LBL--24715

DE88 007371

Inclusive $\pi^{\pm}$, $K^{\pm}$ and p, $\bar{p}$ Production in e^+e^- Annihilation at $\sqrt{s} = 29$ GeV

By
Glen D. Cowan
Ph.D. Thesis
January 27, 1988

Lawrence Berkeley Laboratory
University of California
Berkeley, CA 94720

Abstract

Measurements of $\pi^{\pm}$, $K^{\pm}$ and p, $\bar{p}$ inclusive cross sections and fractions in e^+e^- annihilation at $\sqrt{s} = 29$ GeV are presented. The momentum interval covered corresponds to $0.01 < z < 0.90$, where $z = p/p_{beam}$. The analysis is based on approximately 70 pb^{-1} of data collected between 1984 and 1986 with the TPC/2γ detector at PEP. Charged particles are identified by a simultaneous measurement of momentum and ionization energy loss (dE/dx). The recently upgraded detector's momentum resolution of $(\Delta p/p)^2 = (1.5\%)^2 + (0.65\% \cdot p \text{ (GeV/c) })^2$ and a dE/dx resolution of typically 3.5% allow the measurements to be extended to higher z than previously reported.

This work was supported by the United States Department of Energy under Contract DE-AC03-76SF00098.

Contents

Acknowledgements iii

1 **Introduction** 1

2 **Theory of Hadron Production in e^+e^- Annihilation** 3

- 2.1 Introduction ... 3
- 2.2 e^+e^- Annihilation into Fermion Pairs ... 5
- 2.3 Perturbative QCD ... 9
- 2.4 Hadronization ... 15
  - 2.4.1 Independent Fragmentation Models ... 15
  - 2.4.2 String Fragmentation Models ... 21
  - 2.4.3 Cluster Fragmentation Models ... 31
  - 2.4.4 The Caltech-II Model ... 31
  - 2.4.5 Dimensional Counting Rules ... 32
- 2.5 Effects of Resonance Decays ... 33

3 **PEP and the TPC/2γ Detector** 36

- 3.1 The PEP e^+e^- Storage Ring ... 36
- 3.2 The TPC/2γ Detector: Overview ... 36
- 3.3 The Time Projection Chamber ... 39
- 3.4 Upgrades to the TPC ... 44
- 3.5 The Trigger System ... 47
- 3.6 Calibration and Test Pulsing Systmes ... 49
- 3.7 Position Measurement ... 50

4 **Particle Identification by Measurement of Ionization Energy Loss** 55

- 4.1 Introduction ... 55
- 4.2 Energy Loss in the TPC: Theoretical Considerations ... 58
- 4.3 General Theory of Ionization Energy Loss ... 61

4.4 Model for the Most Probable Energy Loss in the TPC 64
4.5 Fit of the dE/dx Model to Data 71
4.6 Estimation of the dE/dx Resolution 75

5 Event Reconstruction, Selection and Simulation 79
5.1 Introduction 79
5.2 Online Analysis 79
5.3 Offline Analysis 84
5.4 Final Corrections to the Data 86
5.5 Event Simulation 88
5.6 Backgrounds in the Multihadron Event Sample 90

6 Determination of the Inclusive Cross Sections and Fractions 95
6.1 Objectives 95
6.2 Track Selection 96
6.3 Statistical Fit for the Number of Observed Hadrons 97
6.4 Acceptance Corrections 103
6.5 Error Analysis 104
6.6 Results 110

7 Discussion of Results 126
7.1 Introduction 126
7.2 Comparison with other Experiments 126
7.3 Comparison with Fragmentation models 133

8 Summary and Conclusions 147

References 148

Acknowledgements

This thesis was made possible by many years of hard work by the TPC/2γ collaboration, the current members of which are listed below:

The TPC/Two-Gamma Collaboration

H. Aihara, M. Alston-Garnjost, R.E. Avery, A. Barbaro-Galtieri, A.R. Barker, B.A. Barnett, D.A. Bauer, H.-U. Bengtsson, G.J. Bobbink, C.D. Buchanan, A. Buijs, D.O. Caldwell, H.-Y. Chao, S.-B. Chun, A.R. Clark, G.D. Cowan, D.A. Crane, O.I. Dahl, M. Daoudi, K.A. Derby, J.J. Eastman, P.H. Eberhard, T.K. Edberg, A.M. Eisner, R. Enomoto, F.C. Erné, K.H. Fairfield, J.M. Hauptman, W. Hofmann, J. Hylen, T. Kamae, H.S. Kaye, R.W. Kenney, S. Khacheryan, R.R. Kofler, W.G.J. Langeveld, J.G. Layter, W.T. Lin, F.L. Linde, S.C. Loken, A. Lu, G.R. Lynch, R.J. Madaras, B.D. Magnuson, G.E. Masek, L.G. Mathis, J.A.J. Matthews, S.J. Maxfield, E.S. Miller, W. Moses, D.R. Nygren, P.J. Oddone, H.P. Paar, S.K. Park, D.E. Pellett, M. Pripstein, M.T. Ronan, R.R. Ross, F.R. Rouse, K.A. Schwitkis, J.C. Sens, G. Shapiro, B.C. Shen, W.E. Slater, J.R. Smith, J.S. Steinman, R.W. Stephens, M.L. Stevenson, D.H. Stork, M.G. Strauss, M.K. Sullivan, T. Takahashi, S. Toutounchi, R. van Tyen, G.J. VanDalen, R.F. van Daalen Wetters, W. Vernon, W. Wagner, E.M. Wang, Y.-X. Wang, W.A. Wenzel, Z.R. Wolf, H. Yamamoto, S.J. Yellin and C. Zeitlin

In particular, I would like to thank my advisors, Werner Hofmann, Stu Loken and Roy Kerth. I also thank John Rasmussen for reading and commenting on this dissertation.

I am grateful to Gerry Lynch, Al Clark, Mike Ronan, Bill Wenzel and Hiro Yamamoto for their assistance in numerous aspects of the analysis, and to Fred Goozen and Tom Weber for their assistance and instruction in hardware-related matters.

I have benefited from the assistance and friendship of LBL grad students and postdocs Rob Avery, Aurelio Bay, Jack Eastman, Tim Edberg, Lisa Mathis, Bill Moses, Forrest Rouse, Rem van Tyen, Tad Takahashi, Ed Wang, Zack Wolf and Cary Zeitlin.

Last but not least I thank my parents for their support and encouragement.

Chapter 1

Introduction

In the Standard Model of elementary particle physics, quarks and leptons interact by the exchange of photons (electromagnetic interactions) gluons (strong interactions) and intermediate vector bosons (weak interactions). The electromagnetic and weak interactions are described by the Glashow-Weinberg-Salam model, and the strong interactions by quantum chromodynamics (QCD). One of the currently unsolved problems of this picture is how the fundamental fields of QCD, quarks and gluons, transform into observable hadrons, e.g. pions, kaons, and protons, in high energy reactions such as e^+e^- annihilation.

In this dissertation, the inclusive production of charged hadrons in e^+e^- annihilation is studied, that is, the reaction $e^+e^- \rightarrow$ hadron + X, where the hadron is a charged pion, kaon or proton, and X represents all other particles in the event. The inclusive cross sections and charged hadron fractions are fundamental quantities providing information about quark and gluon fragmentation. Measurements of these quantities are presented based on data collected between 1984 and 1986 with the TPC/2γ detector at PEP, operating at a center-of-mass energy of $\sqrt{s}$ = 29 GeV. Recent upgrades in the detector allowed for measurements of improved accuracy, and extending to higher z, where $z \equiv p_{hadron}/p_{beam}$, than previously reported [1, 2, 3, 4].

The particle spectra in the high-z region provide a sensitive probe of the hadron production mechanism, especially for the case of baryons. For example, dimensional counting arguments predict that the baryon to meson ratio for $z \rightarrow 1$ should fall as $(1-z)^{1-2}$ [5] whereas the symmetric Lund string model predicts a rising baryon fraction [6]. The potential to discriminate between competing hadron production models is enhanced at high z by the fact that a comparatively large fraction of the particles in this region are produced directly in the hadronization process, rather than as the result of resonance decays.

This dissertation includes descriptions of the theory of hadron production in e^+e^- annihilation, the TPC/2γ detector, particle identification by ionization energy loss, event reconstruction, selection and simulation, the analysis technique for obtaining inclusive cross sections and fractions, and a comparison of results with previous measurements and with theoretical predictions.

Chapter 2

Theory of Hadron Production in e^+e^- Annihilation

2.1 Introduction

The reaction $e^+e^- \rightarrow$ hadrons proceeds, to a good approximation, as shown in figure 2.1. In the first stage, the electron and positron annihilate into a virtual intermediate vector boson (photon or Z^0) which decays into a quark-antiquark pair. This part of the process is well described by the standard model of electroweak interactions using perturbation theory. The quark and antiquark move apart with a certain probability of emitting a hard (i.e. large-Q^2) gluon. Hard gluon emission can be described by perturbation theory of quantum chromodynamics, since for sufficiently large Q^2 the QCD coupling constant, α_S, is small.

These primary particles (or partons) are not, however, directly observed. Instead one sees "jets" of hadrons, a jet being several or more particles whose momenta are more or less aligned along some axis. The transformation of the initial partons (quarks and gluons) into observable hadrons is known as hadronization. The gray blob in figure 2.1 reflects our lack of understanding of this part of the process. The "observable" (i.e. color-

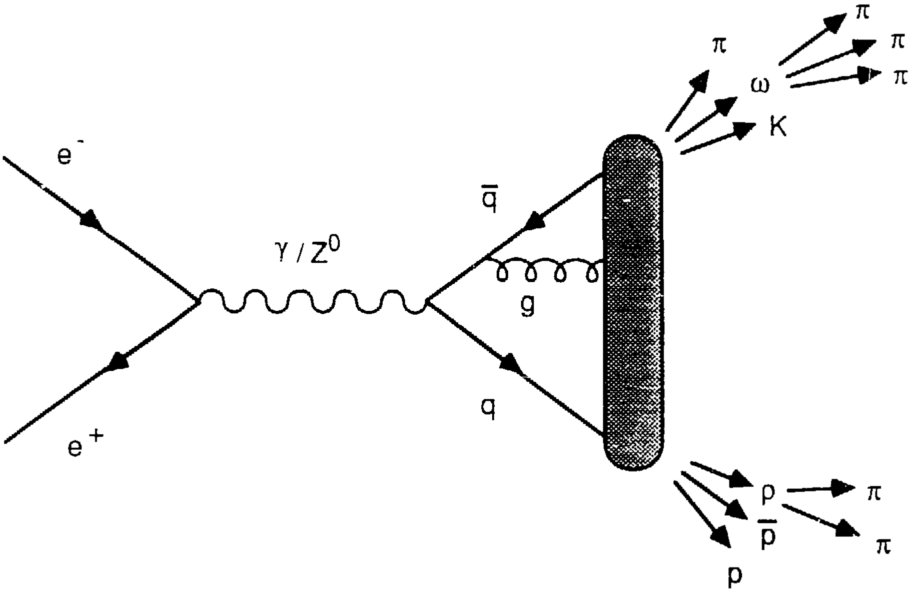

Figure 2.1 The reaction $e^+e^- \rightarrow$ hadrons.

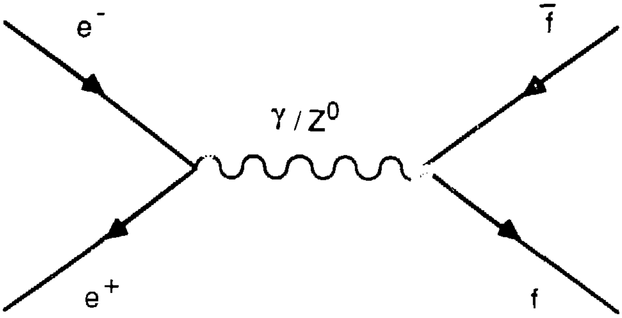

Figure 2.2 The reaction $e^+e^- \rightarrow$ fermion pair.

neutral) hadrons include resonances whose lifetimes are on the order of 10^{-22} seconds. The resonances decay into longer lived hadrons (e.g. pions, kaons, protons) which can be detected experimentally. Each part of this process will now be examined in greater detail.

2.2 e^+e^- Annihilation into Fermion Pairs

The formation of spin-1/2 particle-antiparticle pairs in electron-positron annihilation is described to lowest order in quantum electrodynamics by the Feynman diagram shown in figure 2.2. In the limit where the center-of-mass energy is much greater than the fermion's rest mass, one obtains the differential cross section

$$\left(\frac{d\sigma}{d\Omega}\right)_{f\bar{f}} = \frac{\alpha^2 e_f^2}{4s}\;(1 + \cos^2\theta)\,. \tag{2.1}$$

Here θ is the angle between the incoming electron and the outgoing fermion in the CM system, α is the fine structure constant, s is the square of the total center-of-mass energy, and e_f is the charge of the outgoing fermion measured in units of the electron charge. For the production of pairs of spin-0 particles, the angular distribution would be proportional to $\sin^2\theta$.

Integrating equation 2.1 over the polar angle θ one obtains the total cross section for annihilation into fermion-antifermion pairs:

$$\sigma_{f\bar{f}} = \frac{4\pi}{3s}\;\alpha^2 e_f^2 \tag{2.2}$$

For creation of muon pairs one has $e_\mu = 1$ giving, for $\sqrt{s} = 29$ GeV,

$$\sigma_{\mu^+\mu^-} = \frac{4\pi}{3s}\;\alpha^2 = 0.103\ \text{nb}. \tag{2.3}$$

For creation of quark-antiquark pairs of a given flavor (q = u, d, s, c, b or t) one obtains

$$\sigma_{q\bar{q}} = \frac{4\pi}{3s}\ \alpha^2 e_q^2 \cdot 3 \qquad (2.4)$$

where the factor of three comes from the fact that a quark can be formed in three different colors. The u, c, and the as of yet unobserved t quarks have a charge of 2/3, and the d, s and b quarks have -1/3. Thus the flavors u, c, d, s and b are predicted to be produced in the ratios 4 : 4 : 1 : 1 : 1.

In order to calculate the total cross section for e^+e^- annihilation into hadrons, one traditionally sums equation 2.4 over the relevant quark flavors and divides by the cross section for $e^+e^- \rightarrow \mu^+\mu^-$ as predicted by equation 2.3:

$$R \equiv \frac{\sigma_{e^+e^- \rightarrow hadrons}}{\sigma_{\mu^+\mu^-}} = 3\sum e_q^2 \qquad (2.5)$$

Including the flavors u, c, d, s and b one obtains $R = 11/3$. Recent measurements of R at PEP and PETRA give $R = 4.03 \pm 0.02$ (stat.) $\pm$ 0.05 (sys.) [7]. The fact that the measured value is close to 11/3 is taken as evidence that quarks can indeed be produced in three different color states, and that the t quark is too massive to be produced at PEP or PETRA energies. The discrepancy between the predicted and observed values is attributed to strong and electroweak interaction corrections and can be used to estimate the QCD coupling constant, α_s [7].

Free quarks have not, however, been observed in e^+e^- annihilation. Searches for fractionally charged particles (i.e. 1/3, 2/3, 4/3 $\times$ e) have resulted in limits on the total inclusive cross section $\sigma(e^+e^- \rightarrow q, \bar{q} + X)$ of 10^{-4} - 10^{-2} $\times$

$\sigma(e^+e^- \to \mu^+\mu^-)$, depending on the quark mass and charge [8, 9]. Instead, one sees events with back-to-back jets of "ordinary" hadrons (i.e. π, K, p, etc.) such as the two-jet event shown in figure 2.3. An event axis and a quantitative measure of the event shape can be determined by defining the momentum tensor

$$M_{\alpha\beta} = \sum_{i=1}^{n} p_{i\alpha} \cdot p_{i\beta} \tag{2.6}$$

where α and β refer to the x, y and z components, and i runs over all the particles (or in practice only the detected charged particles) in the event. Diagonalizing $M_{\alpha\beta}$, one determines unit eigenvectors $\boldsymbol{n}_\alpha$, and normalized eigenvalues λ_α:

$$\lambda_\alpha = \frac{\sum_{i=1}^{n} \boldsymbol{p}_i \cdot \boldsymbol{n}_\alpha}{\sum_{i=1}^{n} \boldsymbol{p}_i^2} \tag{2.7}$$

Ordering the eigenvalues so that $\lambda_1 \geq \lambda_2 \geq \lambda_3 \geq 0$, one defines the sphericity, S, and the aplanarity, A, by

$$S = \frac{3}{2}(\lambda_2 + \lambda_3) \tag{2.8}$$

$$A = \frac{3}{2}\lambda_3 \tag{2.9}$$

The eigenvector $\boldsymbol{n}_1$ defines the sphericity axis, the direction with respect to which the sum of the squares of the transverse momenta is minimized. For extreme two-jet events, $S \to 0$, whereas for spherical events, $S = 1$. Extreme flat events have $A = 0$, and lie in the plane defined by $\boldsymbol{n}_1$ and $\boldsymbol{n}_2$. A scatter

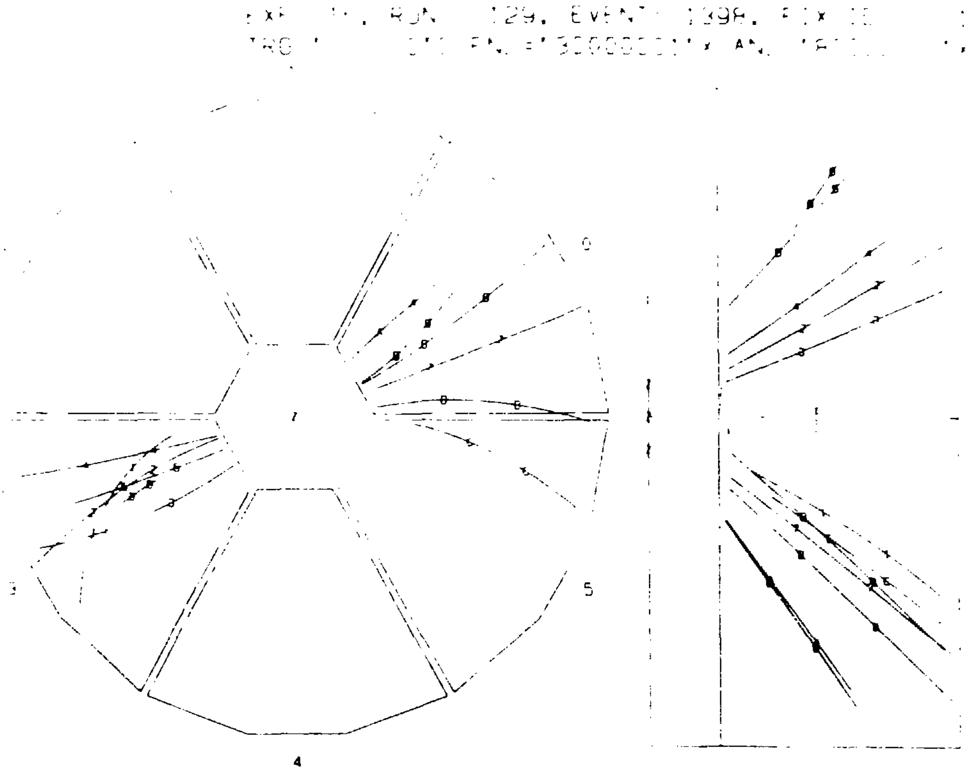

(a) (b)

Figure 2.3 A two-jet event seen by the TPC. The event is characterized by low spehricity, S = 0.0343, and low aplanarity, A = 0.00461. (a) End view. (b) Radial view (i.e. projection onto the r-z plane).

plot of A versus S (figure 2.4) shows that most of the multihadron events possess a two-jet structure.

The distribution of angles between the sphericity axis and the beam direction, θ_S, for multihadron events is shown in figure 2.5. It agrees quite closely with the $1 + \cos^2\theta_S$ distribution predicted for spin-1/2 quark-antiquark production, after the latter has been folded with the detector acceptance. The interpretation is that the colored quark and antiquark turn into colorless hadrons via interactions involving only small transverse momentum transfers, resulting in jets which "remember" the original direction of the quark-antiquark pair.

2.3 Perturbative QCD

The quark-antiquark pair created in the annihilation process move apart with a relative speed close to c, interacting via gluon exchange. For sufficiently small distance scales ($d \sim 10^{-14}$ cm) the four-momentum transfers involved in the interaction are sufficiently large ($\sqrt{Q^2} \sim 1/d$) that perturbation theory can be used. This is because the coupling constant in quantum chromodynamics, α_S, decreases for large Q^2. This is an important property of QCD known as asymptotic freedom, and is expressed by the formula

$$\alpha_S\,(Q^2) = \frac{12\pi}{(\,33 - 2N_f\,)\;\log\,(\,Q^2\,/\,\Lambda^2\,)} \qquad (2.10)$$

where N_f is the number of quark flavors and Λ is a parameter determined by experiment.

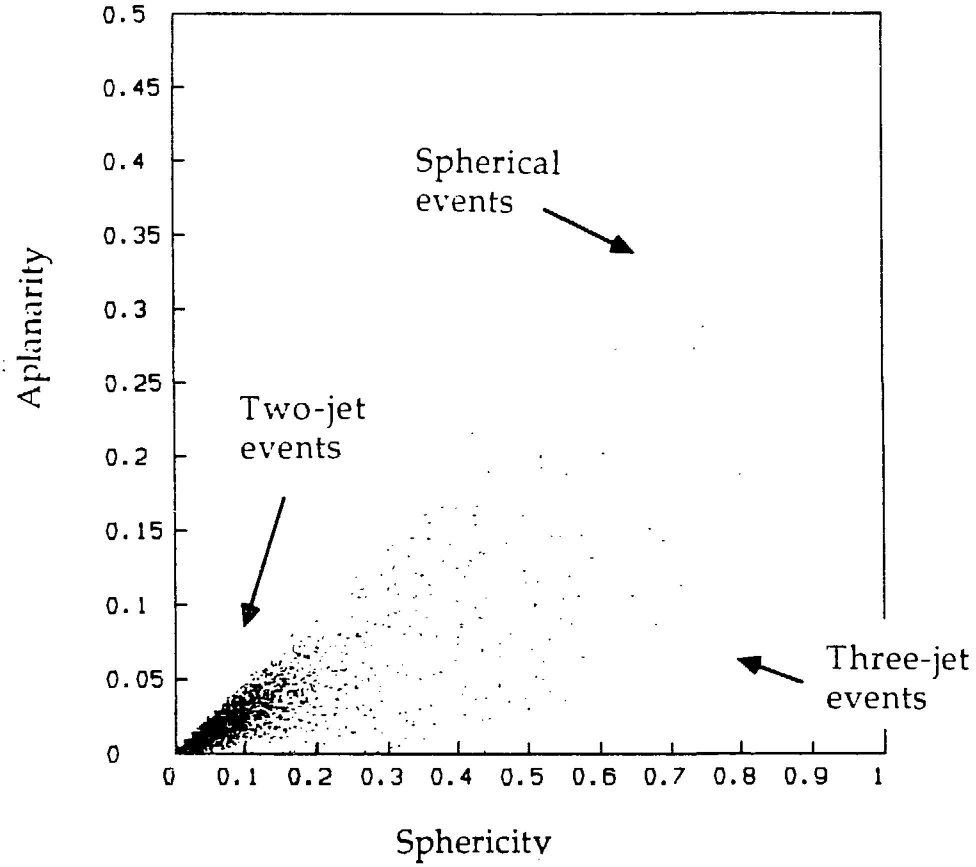

Figure 2.4 A scatter plot of aplanarity, A, versus sphericity, S, showing that most multihadron events possess a two-jet structure.

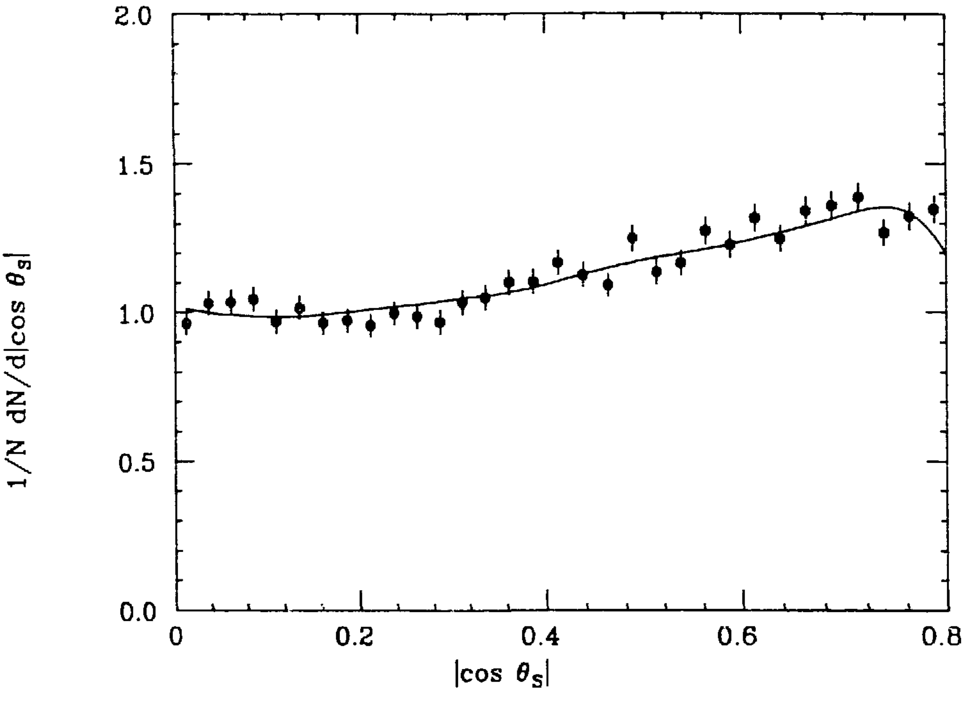

Figure 2.5 The normalized distribution of $|\cos\theta_S|$ for multihadron events, where θ_S is the angle between the beam line and the sphericity axis. The points are measured values from the TPC/2γ detector. The curve is $1 + \cos^2\theta$, folded with the detector acceptance.

Using the Feynman diagram rules derivable from the lagrangian of QCD, one can, for example, compute the cross section for one of the quarks to emit a gluon, as shown in figure 2.6 [10]. In terms of the kinematic variables

$$x_q = 2E_q / \sqrt{s}, \qquad x_{\bar{q}} = 2E_{\bar{q}} / \sqrt{s}, \qquad x_g = 2E_g / \sqrt{s}, \tag{2.11}$$

the normalized cross section to order $\alpha^2\alpha_s$ is

$$\frac{1}{\sigma}\,\frac{d\sigma}{dx_q\,dx_{\bar{q}}} = \frac{2\alpha_s}{3\pi}\,\frac{x_q^2 + x_{\bar{q}}^2}{(1 - x_q)\,(1 - x_{\bar{q}})}\,. \tag{2.12}$$

This cross section diverges if the gluon's energy approaches zero, leading to $x_q \to 1$ and $x_{\bar{q}} \to 1$, or if the gluon is collinear with either the quark or antiquark, leading to $x_{\bar{q}} \to 1$ or $x_q \to 1$ respectively. Physically, these situations correspond to the impossibility of resolving an infinitely soft gluon or a quark-gluon pair separated by an infinitely small angle. Second-order (i.e. α_s^2) calculations for $e^+e^- \to$ hadrons are complicated mathematically but have been carried out. Results can be found in reference [11].

Events of the type $e^+ e^- \to q\,\bar{q}\,g$ lead to three jets of hadrons in the final state, such as the one shown in figure 2.7. Three-jet events are characterized by high sphericity but low aplanarity, since momentum conservation requires that the q, $\bar{q}$ and g momenta lie in the same plane. At the center-of-mass energy of the PEP storage ring (29 GeV) roughly 8% of the events are of the three-jet variety, having a sphericity greater than 0.3 and an aplanarity less than 0.1.

An alternative approach to perturbative QCD is used in the leading-logarithm approximation (LLA). Instead of summing all diagrams up to a

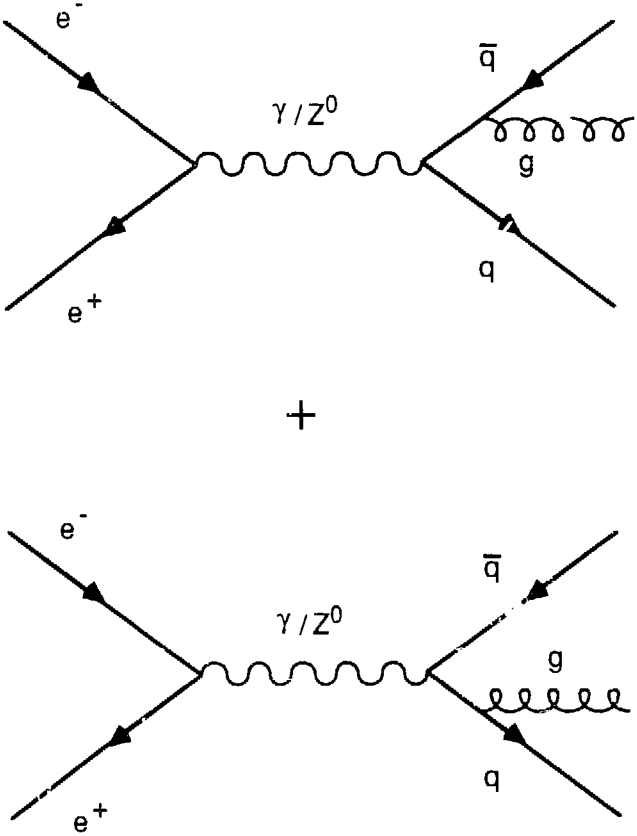

Figure 2.6 The Feynman diagrams for the process $e^+e^- \rightarrow q\,\bar{q}\,g$ to order $\alpha^2\alpha_s$.

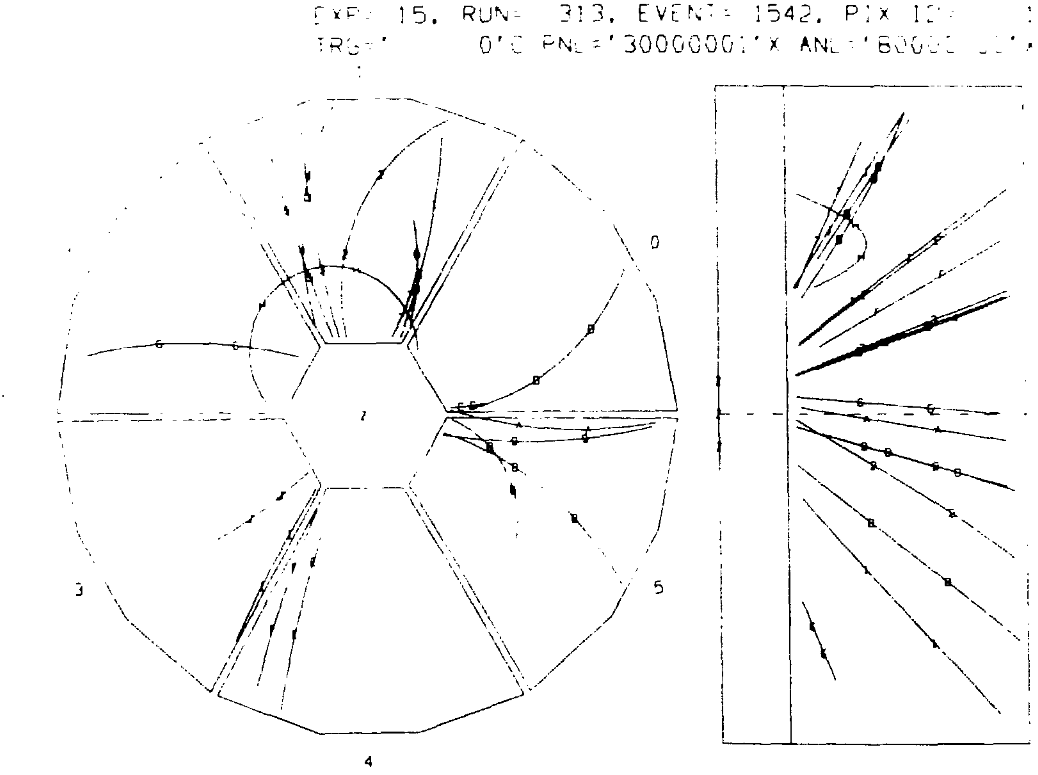

(a) (b)

Figure 2.7 A three-jet event seen by the TPC. The event is characterised by high spehricity, S = 0.676, and low aplanarity, A = 0.0633. (a) End view. (b) Radial view (i.e. projection onto the r-z plane).

fixed order in α_s, diagrams containing leading infrared and collinear singularities are summed to all orders. The LLA probability for the decay of a parton A into partons B and C is given by

$$dP = \frac{dt}{t}\,\frac{\alpha_s(t)}{2\pi}\,dz\ P_{B/A}(z) \tag{2.13}$$

where the virtuality of parton A is given by $t = (p_B + p_C)^2$, z is the fraction of parton A's momentum given to parton B, and $P_{B/A}(z)$ is the Altarelli-Parisi splitting function, given in [12] for A, B = q, $\bar{q}$, g. Using equation 2.13, one can calculate the probability of a "parton shower" as shown in figure 2.8 [13].

2.4 Hadronization

Equation 2.10 predicts that as the Q^2 of the interaction decreases below about 1 GeV^2, the strong coupling constant, α_s, becomes of order unity, and the predictions of perturbation theory become invalid. Perturbation theory fails, therefore, to predict how the quarks and gluons, which carry color charge, bind together to form colorless hadrons. In order to obtain quantitative predictions for, for example, the production rates of pions, kaons and protons, one must turn to phenomenological models, implemented in practice as Monte Carlo programs. Some additional insight is provided by dimensional counting rules [5].

2.4.1 Independent Fragmentation Models

One of the first models for the process $e^+e^- \to q\bar{q} \to$ hadrons was the independent fragmentation model of Feynman and Field [14]. In the Feynman-Field scheme, the original quark and antiquark each transform into a jet of hadrons independently, via processes of the type

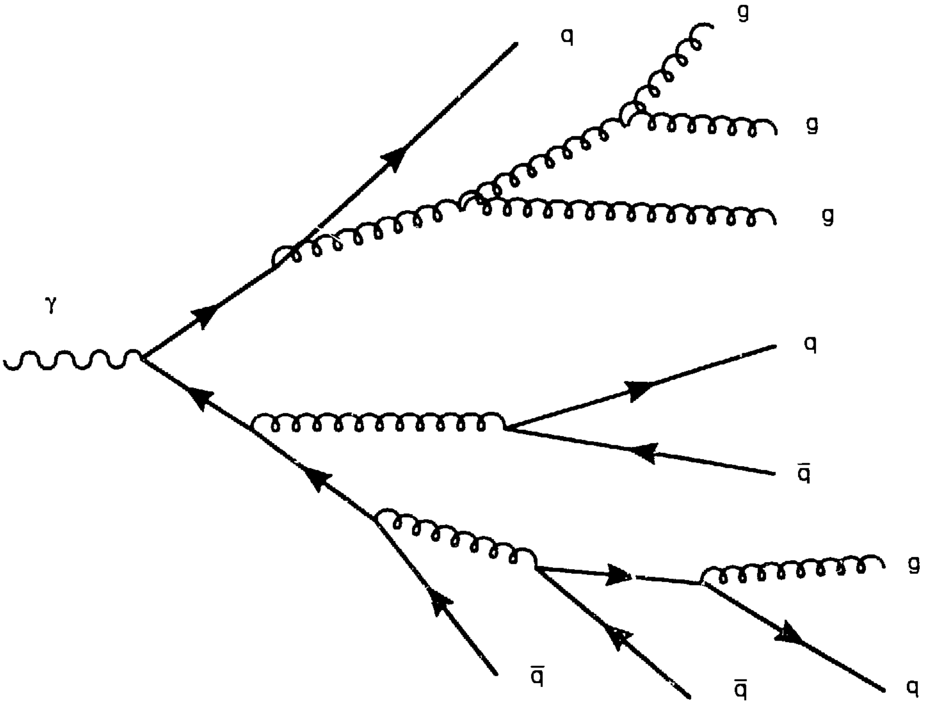

Figure 2.8 A parton shower following the decay of a virtual photon into a quark-antiquark pair.

$$q_0 \rightarrow h(q_0, \bar{q}_1) + q_1, \tag{2.14a}$$

$$q_1 \rightarrow h(q_1, \bar{q}_2) + q_2, \ \text{etc.} \tag{2.14b}$$

Here, q_0 is the quark from the original quark-antiquark pair. A new quark-antiquark pair (q_1, $\bar{q}_1$) is created from the vacuum as represented in figure 2.9. The quark q_0 and the antiquark $\bar{q}_1$ combine to form a hadron $h(q_0, \bar{q}_1)$, leaving an unpaired quark, q_1, with less energy than the original q_0. This procedure is then repeated for quarks q_1, q_2, and so on, until the remaining quark is left with insufficient energy to form a hadron. It is assumed that the transverse momenta of the quarks and antiquarks created from the vacuum follow a Gaussian distribution, and that the total transverse momentum of each pair is zero. The flavor content of the hadron is determined simply by the flavors of its constituent quarks. The probabilities for producing vector or pseudoscalar mesons are left as adjustable parameters, which in the original version were made to be equal.

The model involves one arbitrary function, $f(\zeta)$, which specifies the probability that the hadron $h(q_i, \bar{q}_j)$ will receive a certain fraction, ζ, of the momentum of its parent quark, q_i. (The variable ζ is the same as $1-\eta$ used in [14], and should not be confused with $z = p_{hadron}/p_{beam}$.) Feynman and Field chose $f(\zeta)$ to be of the form

$$f(\zeta) = 1 - a + 3a(1-\zeta)^2 \tag{2.15}$$

where the parameter a is determined from experiment. It is assumed that the same function $f(\zeta)$ applies to all iterations of the cascade. The hadrons initially produced in this procedure are called primary hadrons, and include short-lived resonances. The order in which the primary hadrons are

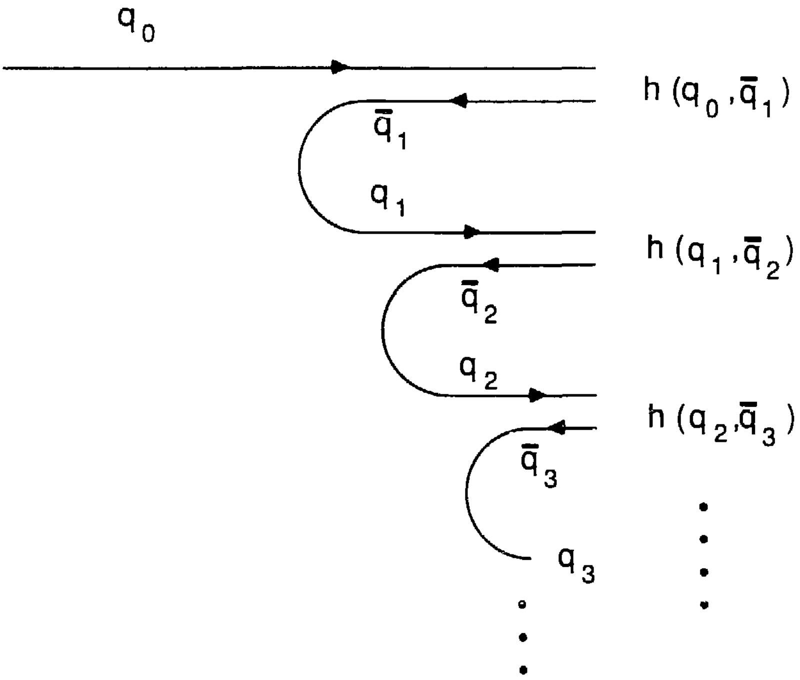

Figure 2.9 A schematic representation of hadron production in the Feynman-Field model.

produced is known as their rank. By specifying the function $f(\zeta)$, one determines the momentum spectrum of the primary hadrons. It can be obtained via the integral equation

$$D(z) = f(z) + \int_z^1 \frac{d\zeta}{\zeta} f(\zeta)\, D\left(\frac{z}{\zeta}\right), \tag{2.16}$$

where z is the ratio of the hadron's momentum to that of the initial quark q_1, or equivalently, p_{hadron}/p_{beam}. The first term in equation 2.16 corresponds to the case where the hadron has a rank of one, (i.e. contains the original quark) and the second term corresponds to hadrons produced in subsequent iterations of the cascade.

The model as described up to this point does not include any mechanism for baryon production, although baryons are observed to account for approximately 5% of the total multiplicity in multihadron events [3, 4]. A simple extension of the Feynman-Field model for baryon production was proposed by Meyer [15]. In this scheme, one assumes that occasionally two quark-antiquark pairs, instead of one, are produced from the vacuum. The quarks and antiquarks then align to form a baryon-antibaryon pair. For this to take place, the (anti)quarks in the two pairs must be created with a small relative momentum, and behave somewhat like a single particle or "(anti)diquark". Meyer originally used the same fragmentation function (i.e. the same value of a in equation 2.15) and the same transverse momentum spectrum for baryons as for mesons. By introducing additional parameters, however, these could in general be different.

In addition to predictions for the inclusive momentum spectra, the model also predicts that the quantum numbers of mesons of neighboring rank should be highly correlated. This arises from the fact that the quantum numbers of the quark and antiquark (or diquark and antidiquark) pulled from the vacuum are necessarily opposite. So, for example, if the quark q_0 in figure 2.9 is of type u, and the pair (q_1, $\bar{q}_1$) is composed of an s and an $\bar{s}$, then the hadron h(q_0, $\bar{q}_1$) will have strangeness $S = +1$ (e.g. a K^+). If the pair (q_2, $\bar{q}_2$) is composed of a u and a $\bar{u}$, the meson h(q_1, $\bar{q}_2$) will have strangeness $S = -1$ (e.g. a K^-). If particles of neighboring rank remain similarly ordered in longitudinal momentum (or rapidity, $y = 1/2\, ln(\, E+p_l \,/\, E-p_l \,)$) one would expect to observe hadrons of opposite strangeness produced close together in momentum space. Such correlations have been studied for a variety of quantum numbers including strangeness [16], baryon number [17], and electric charge [18]. (In fact, depending on the choice of $f(\zeta)$, the correlation may be washed out considerably. This occurs because for a sufficiently broad $f(\zeta)$, mesons of lower rank can be produced with higher momenta. See reference [17].)

The picture as described so far is complicated by several effects. First, one should not expect all flavors of q $\bar{q}$ pairs to be produced in the cascade with equal probability because of differences in quark masses. Feynman and Field assumed the quark flavors u, d and s to be produced in the ratios 2:2:1. (This point is examined in greater detail in section 2.4.2.) In addition, equation 2.16 only holds for primary hadrons, which include short-lived resonances. These resonances decay into longer lived hadrons which share their parent's momentum, resulting in a much larger number of low momentum hadrons (mostly pions) than would be predicted by equation 2.16.

Although the Feynman-Field model does a surprisingly good job of parameterizing experimental results, a number of problems prevent it from being regarded as a true theory of hadronization. For example, at the end of the cascade, one always has one quark and one antiquark "left over", with no simple way of combining them together to form a hadron. In addition, because the model employs the momentum of the original quark in the laboratory frame, it is not Lorentz covariant. These problems were pointed out by Feynman and Field, who intended for their model to provide a convenient parameterization rather than a fundamental theory for hadron production.

2.4.2 String Fragmentation Models

In an attempt to place hadronization on a more solid theoretical footing, Artru and Mennessier [19] and Andersson [6] have proposed models in which the force field between the original quark and antiquark is approximated as a massless string. The latter of these two models (the Lund model) has been very successful in describing a wide range of experimental data. A number of aspects of this approach will be described, including the flux-tube picture of the QCD force field, suppression of heavy flavor production, predictions for transverse and longitudinal momentum spectra, and mechanisms for baryon production.

Casher, Neuberger and Nussinov [20] have examined the relationship between hadron production and the tubelike configuration of the color field between the quark and antiquark. Consider an electron and a positron separated by a certain distance, as shown in figure 2.10 (a). The electric field lines follow the usual dipole pattern, having a significant non-zero value

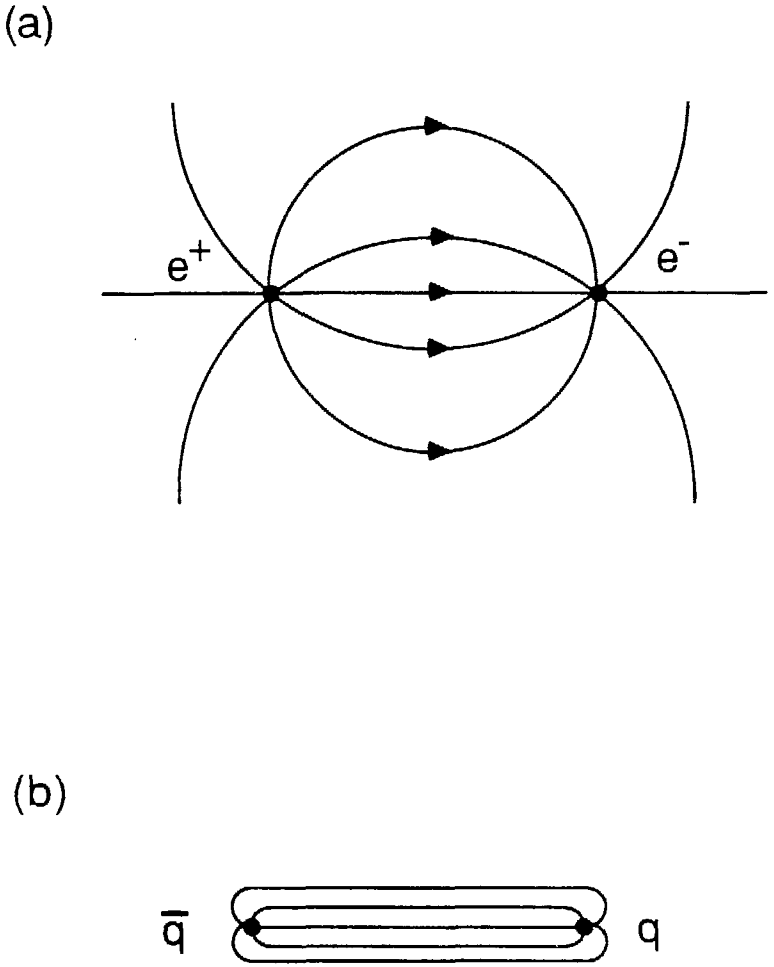

Figure 2.10 (a) The electric field lines between and electron and positron. (b) The lines of force between a quark and antiquark, confined in a narrow flux tube.

even at distances large compared to the separation. In the case of a quark and an antiquark carrying color charge, however, the color field is believed to be confined to a narrow flux-tube, as shown in figure 2.10 (b). Within the context of QCD this effect stems from the fact that gluons couple to themselves (the three-gluon coupling) whereas photons in QED do not. The parallel field lines imply a constant field strength (i.e. independent of separation distance) and a constant energy per unit length in the tube, κ. (This is analogous to a parallel-plate capacitor in electromagnetism.) This picture is consistent with the linear potentials predicted by QCD lattice gauge theory calculations [21].

The energy per unit length, κ, is simply the force on the quark or antiquark at the ends of the tube. Solving the equation of motion $dp/dt = \pm \kappa$ for a bound $q\,\bar{q}$ pair (i.e. a meson), one obtains classical "yo-yo" trajectories such as those shown in figure 2.11 (a) (meson at rest) and figure 2.11 (b) (meson moving with a speed β). Consider the quark and antiquark turning points (x_1, t_1) and (x_2, t_2) as shown in figure 2.11. If the meson is at rest, $t_2 - t_1 = 0$ and $x_2 - x_1 = m / \kappa$, where m is the meson's mass. Thus one obtains the condition

$$(x_2 - x_1)^2 - (t_2 - t_1)^2 = m^2 / \kappa^2 \tag{2.17}$$

which is valid in all reference frames, since the quantity $(x_2 - x_1)^2 - (t_2 - t_1)^2$ is a Lorentz invariant. The speed, momentum and energy of the meson are given by

$$\beta = (t_2 - t_1) / (x_2 - x_1), \tag{2.18a}$$

$$p = \kappa (t_2 - t_1)\,, \tag{2.18b}$$

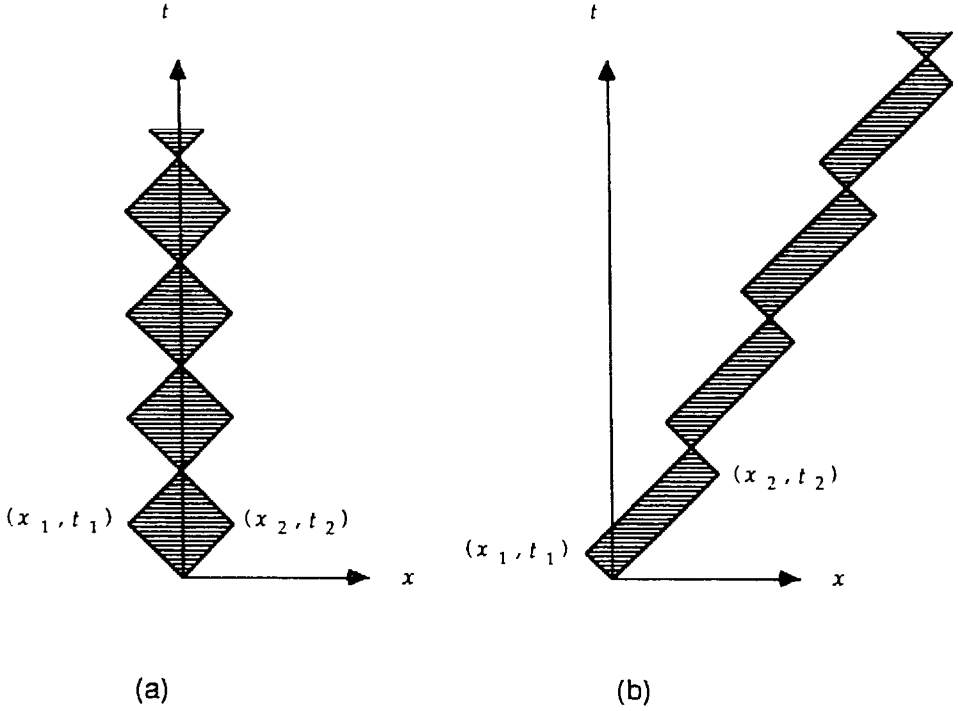

Figure 2.11 (a) "Yo-yo" trajectory for a quark-antiquark pair, representing a meson at rest. (b) A meson moving with a velocity β.

$$E = \kappa (x_2 - x_1) . \qquad (2.18b)$$

Such a picture is useful for studying the space-time development of a quark-antiquark system and its subsequent transformation into hadrons. As the the original quark and antiquark produced in e^+e^- annihilation recede from each other, their kinetic energy is transformed into potential energy in the color field. Multiple particle production results from quark-antiquark pair production within the flux-tube, where the color field is assumed to be completely screened in the regions between the pairs. This is depicted in figure 2.12, where the shaded areas denote regions of nonvanishing color field. In the figure, quark q_0 and antiquark $\bar{q}_1$ combine to form a meson $h(q_0, \bar{q}_1)$, q_1 combines with $\bar{q}_2$ to form the meson $h(q_1, \bar{q}_2)$ and so forth. Note that the space-time coordinates of the pair-production vertices are constrained by the mass-shell condition (equation 2.17) in order that the mass of the quark-antiquark system correspond to a physical meson mass.

The q $\bar{q}$ pair production within the flux tube is assumed to proceed in a manner similar to fermion-pair production in the 1 + 1 dimensional QED of Schwinger [22]. If a quark and an antiquark, both of mass m_q and transverse momentum with respect to the tube $p_\perp$ are created at the same point in the flux tube, energy conservation is violated by an amount $2m_\perp$, where $m_\perp = (m_q^2 + p_\perp^2)^{1/2}$ (the transverse mass.) Once the quark and antiquark are separated by a distance $d = 2\, m_\perp / \kappa$, energy conservation is maintained provided that the field is completely screened in the region in between. As can be shown using a WKB calculation [6], the probability to tunnel from the initial state with no quarks to the final state with a quark and antiquark separated by a distance $= 2\, m_\perp / \kappa$, is given by

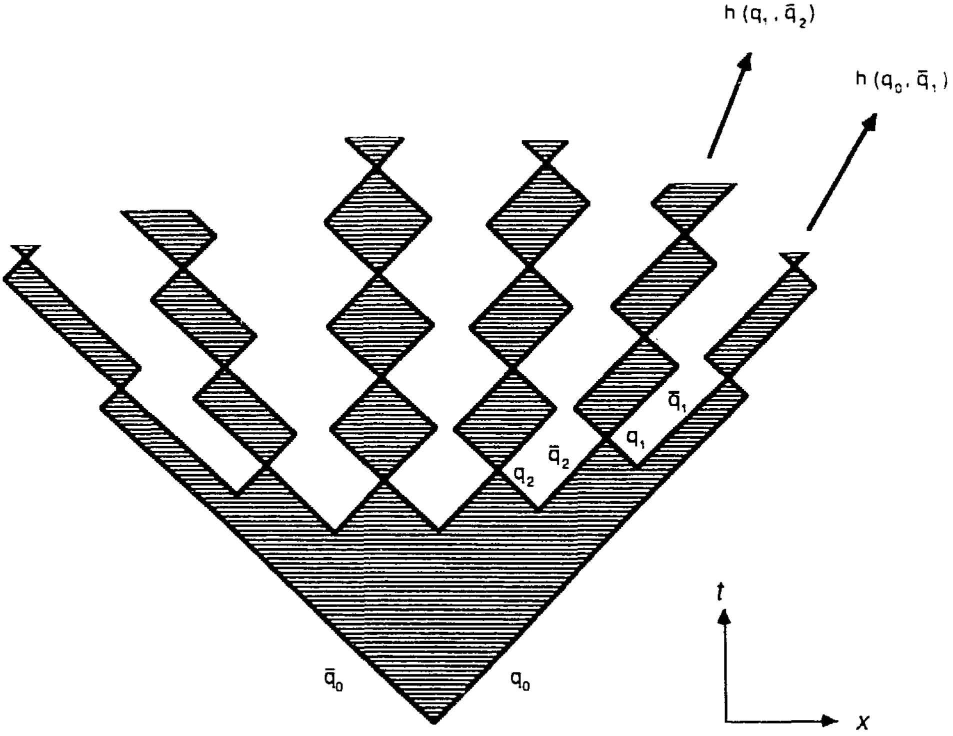

Figure 2.12 The space-time evolution of a quark-antiquark system resulting in meson production. The shaded areas correspond to regions of nonvanishing color field.

$$P \propto \exp\left(\frac{-\pi m_{\perp}^{2}}{\kappa}\right). \tag{2.19}$$

An immediate consequence of equation 2.19 is that production of heavy quarks in the flux tube is highly suppressed. Using a value of $\kappa = 0.2$ GeV^2 = 1 GeV/fm (obtained from charmonium spectroscopy [23] or the slope of Regge trajectories) and quark masses $m_u \approx m_d \approx 0$, $m_s \approx 250$ MeV and $m_c = 1.5$ GeV, one obtains relative probabilities for the production of u, d, s and c of 1 : 1 : 0.37 : 10^{-16}. Thus, strange quark production is substantially suppressed, which should result in a lower production rate for kaons compared to pions. Heavy quarks (c or b) are expected to come almost exclusively from the original q $\bar{q}$ pair.

The flux tube picture is the basis for the Lund model [6], in which q $\bar{q}$ pair production is viewed as the breaking of a string. First, a string is produced with flavors u, d, s, c, b chosen according to the ratios 4 : 1 : 1 : 4 : 1 for the quark and antiquark at the endpoints. A q $\bar{q}$ pair is produced in the string, creating a break. The color field is assumed to be screened between the pair, allowing the two pieces of string to separate. The relative probabilities to produce various quark flavors are left as adjustable parameters, although the final values come out similar to those discussed in the preceding paragraph. The transverse momenta of the quark and antiquark are equal and opposite, and are assumed to follow a Gaussian distribution. The relative probability to produce a vector or pseudoscalar meson is left as an adjustable parameter. A typical vector to pseudoscalar ratio is roughly one.

Once the transverse momentum, spin and flavor (and hence the type) of the hadron have been established, the longitudinal momenta, p_l, is determined. The first meson, composed of the the endpoint quark and the antiquark from the nearest break in the string (or vice versa) receives a fraction, ζ_1, of the available $E+p_l$:

$$(E+p_l)_1 = \zeta_1 \, (E+p_l)_{\mathrm{total}} \,. \tag{2.20a}$$

The transverse momentum, spin and flavor of the second meson are then similarly chosen, and its $E+p_l$ is a certain fraction of the remaining available $E+p_l$:

$$(E+p_l)_2 = \zeta_2 \, (E+p_l)_{\mathrm{remaining}} \,. \tag{2.20b}$$

The procedure is repeated until a certain minimum $(E+p_l)_{\mathrm{remaining}}$ is reached, at which point the system decays into two mesons according to two-body phase space.

By using the quantity $E+p_l$, rather than p_l, the ζ_i are invariant under Lorentz boosts along the direction of the string. The ζ_i are random numbers distributed according to some probability distribution function. In the symmetric Lund model one imposes the (reasonable) restrictions that the rapidity distribution have a central plateau and that the particle spectra on the average not depend on whether one begins the procedure at the quark end or the antiquark end of the string. This restricts the distribution function to be of the form [6, 24]:

$$f(\zeta) \propto N_{\alpha\beta} \, \frac{1}{\zeta} \, \zeta^{a_\alpha} \left(\frac{1-\zeta}{\zeta}\right)^{a_\beta} \exp\left(-\frac{b\, m_\perp^2}{\zeta}\right), \tag{2.21}$$

where $N_{\alpha\beta}$, a_α, a_β and b are parameters (the index α refers to the flavor of the initial quark, β refers to the flavor of the quark produced in the middle of the string) and $m_\perp = (m_h^2 + p_\perp^2)^{1/2}$ is the transverse mass of the hadron produced.

In current implementations all of the a_α are assumed to be equal, in which case equation 2.20 reduces to

$$f(\zeta) \propto \frac{(1-\zeta)^a}{\zeta} \exp\left(-\frac{b\, m_\perp^2}{\zeta}\right). \tag{2.22}$$

Typical values for parameters in equation 2.22 are $a = 1$ and $b = 0.7$ GeV^{-2}.

The Lund model has been extended to include baryons using a diquark scheme similar to that used by Meyer [14, 25]. It is assumed that a break in the string can be caused by creation of a diquark-antidiquark pair. The diquark mass is assumed to be considerably larger than that of a quark, leading to a suppression of the baryon rate as predicted by equation 2.19. In addition, diquarks consisting of a light quark (u or d) and a strange quark are assumed to be heavier than diquarks made up of two light quarks. Summing over all spin and flavor combinations, the diquark to quark ratio is typically around 0.09. Because of the exponential term in equation 2.22, $f(\zeta)$ peaks at a much higher value of ζ for baryons than it does for pions. This results in an increase in the predicted fraction of protons (and of heavier particles in general) for particles of higher momentum.

In the string picture as described so far the initial parton configuration has been a single quark-antiquark pair. The Lund model incorporates gluon emission by describing gluons as "kinks" in the string. Details of this procedure are given in reference [26]. In current implementations, the Lund model uses some form of perturbative QCD (fixed-order matrix elements or parton showers) to describe the initial evolution of a system of quarks, antiquarks and gluons. The four-momenta of the gluons are then associated with kinks in the string. The transformation of the string into hadrons then follows the same procedure as described above, where p_l is understood to mean the momentum along the local string direction.

A modification of the Lund scheme has recently been proposed by the UCLA group [27]. In this model, the Lund expression for $f(\zeta)$, equation 2.22, is reinterpreted as a simultaneous probability density for ζ, m_h, and $p_\perp^2$. The probability for the production of a hadron of $E+p_l$ fraction ζ, mass m_h and transverse momentum $p_\perp^2$ is given by

$$dP \propto \frac{(1-\zeta)^a}{\zeta} \exp\left(-\frac{b\, m_\perp^2}{\zeta}\right) d\zeta\, dp_\perp^2 \qquad (2.23)$$

multiplied by the square of the Clebsch-Gordan coefficients coupling the hadron to its constituent quarks, and by the relative weight of the next two stages in the chain to account for local quantum number conservation. All suppression of heavy hadron production enters through the hadron mass in equation 2.23. There are no "quark level" parameters such as the s/u or diquark/quark ratios in the Lund model. Spin counting is taken care of automatically by the Clebsch-Gordan coefficients, and no separate parameter for the relative production rates of vectors and pseudoscalars is introduced. The UCLA model only contains two adjustable hadronization parameters, a and b, compared to typically 10 parameters in the Lund model.

2.4.3 Cluster Fragmentation Models

Hadron production can also be described by so-called cluster models. In this approach, a parton shower is generated using the leading-log approximation. The shower evolution is stopped when the parton virtuality, t, falls below some cut-off, t_0. Gluons are then split into quark-antiquark pairs. Adjacent quarks and antiquarks are associated with color-singlet clusters which decay into pairs of hadrons (mesons or baryons) according to two-body phase space.

The fundamental parameters are the virtuality cut-off, t_0, and a QCD scale parameter, Λ, which enters into α_s (equation 2.10) which in turn enters into the LLA parton-branching probabilities (equation 2.13). In the most widely used example of this approach, the Webber model [28], additional parameters are included for treatment of very high and very low mass clusters. For example, very large mass clusters are first allowed to break up according to a string scheme, and clusters of a sufficiently small mass are allowed to "decay" into a single hadron. It should be pointed out that the Webber model contains no function corresponding to the $f(\zeta)$ of string or independent fragmentation models, which would directly determine the hadron momentum distributions. Instead, particle production rates are determined entirely from the parton shower and the kinematics of the two-body decays.

2.4.4 The Caltech-II Model

The Caltech-II model [29] employs features of both string and cluster models. The model begins with the generation of an LLA parton shower. The final partonic state is associated with a system of strings. The strings break into smaller strings in a way analogous to the Lund model, but with an important difference: In the Lund approach, the space-time coordinates of the quark-antiquark production vertices are required to obey the mass-shell constraint, equation 2.17. In practice, this amounts to generating hadrons of known masses with momenta determined by the fragmentation function, $f(\zeta)$. In the Caltech-II model, however, the probability of a break is assumed to be constant in over the length of the string:

$$\frac{dP_{\text{break}}}{dx\,dt} = \text{constant}. \tag{2.24}$$

In this way, one replaces the fragmentation function, $f(\zeta)$, by the relatively simple ansatz of constant break-up probability. Unfortunately, this leads to string segments whose masses do not necessarily correspond to the masses of any real hadron. This problem is overcome by stopping the string evolution at a sufficiently large mass and allowing the segments to decay into physical hadrons. This stage is analogous to the cluster decay of the Webber model. Instead of using a two-body phase-space decay, however, the Caltech-II model employs a more sophisticated parameterization of low mass data.

2.4.5 Dimensional Counting Rules

Some additional insight into hadron production is provided by dimensional counting rules (DCR) [5]. For the inclusive process $e^+e^- \rightarrow$ hadron + X, the normalized cross section is predicted to be

$$\frac{1}{\sigma}\frac{d\sigma_i}{dz} \sim \frac{(1-z)^{2n-1}}{z} \tag{2.25}$$

in the limit that $z = p_{\mathrm{hadron}}/p_{\mathrm{beam}}$ approaches one. Here n is the minimum number of quarks (or antiquarks) "left over" in producing the hadron i, as shown in figure 2.13. Thus, n = 2 for baryons and n = 1 for mesons, yielding

$$\frac{1}{\sigma}\frac{\mathrm{d}\sigma_{meson}}{\mathrm{dz}} \sim \frac{(1 - z)}{z}, \tag{2.26a}$$

$$\frac{1}{\sigma}\frac{\mathrm{d}\sigma_{baryon}}{\mathrm{dz}} \sim \frac{(1 - z)^3}{z}. \tag{2.26b}$$

Different assumptions concerning the quark spin lead to slightly differing predictions. The main point is that the baryon cross section is predicted to fall off faster than the meson cross section for $z \to 1$. This can be understood qualitatively by noting that the minimum number of quarks left over, n, is the same as the minimum number of gluons exchanged. Since the Q^2 of the gluon must be large to produce a high-z hadron, and since the gluon propagator goes as $1/Q^2$, one expects the probability to produce a high-z baryon to be less than that of a high-z meson.

2.5 Effects of Resonance Decays

Resonances with decay times on the order of 10^{-22} seconds are produced in the hadronization process at roughly the same rate as longer-lived hadrons. Largely because of kinematic constraints, most resonances tend to decay into pions, which share the momentum of their parents. As a result, a large fraction of the low momentum pions are not produced directly in the hadronization process. The Lund model prediction for the fraction of hadrons which are primary as a function of $z = p_{\mathrm{hadron}}/p_{\mathrm{beam}}$ is shown in figure 2.14. From this it can be seen that to disentangle the characteristics of resonance production from other properties of the hadronization process, it is necessary (or at least preferable) to look at higher momentum particles.

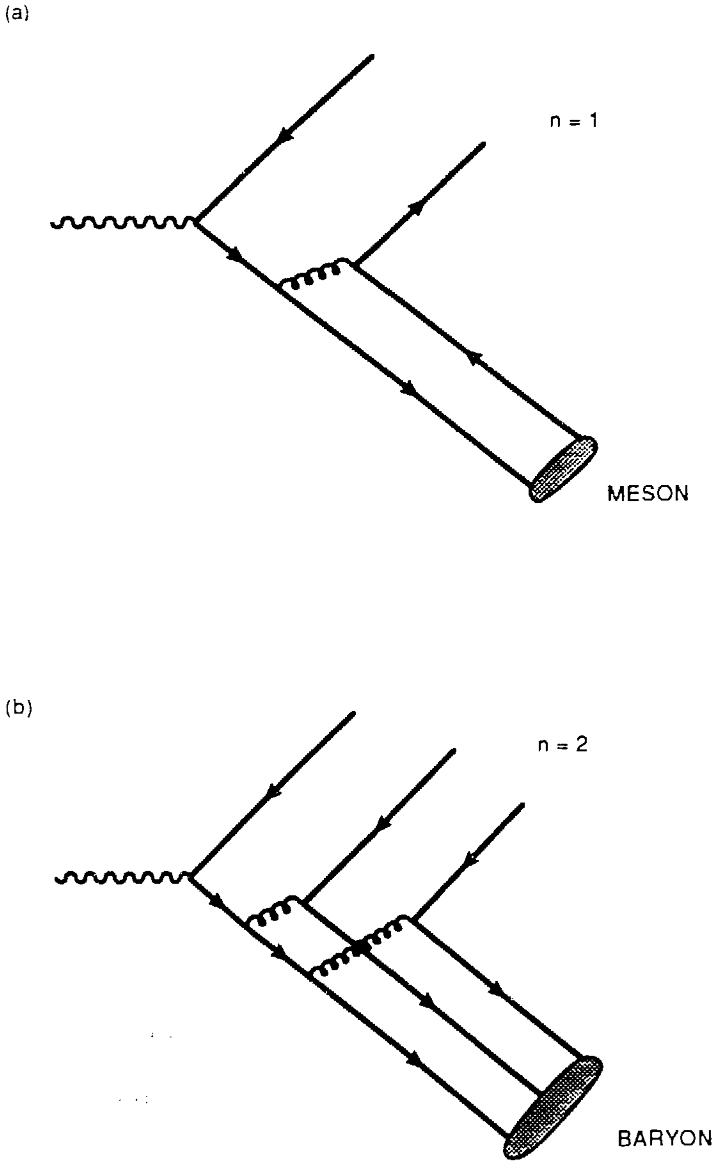

Figure 2.13 Feynman diagrams for $\gamma \rightarrow$ hadron + X, showing the minimum number of quarks "left over", n. (a) For mesons, $n = 1$. (b) For baryons, $n = 2$.

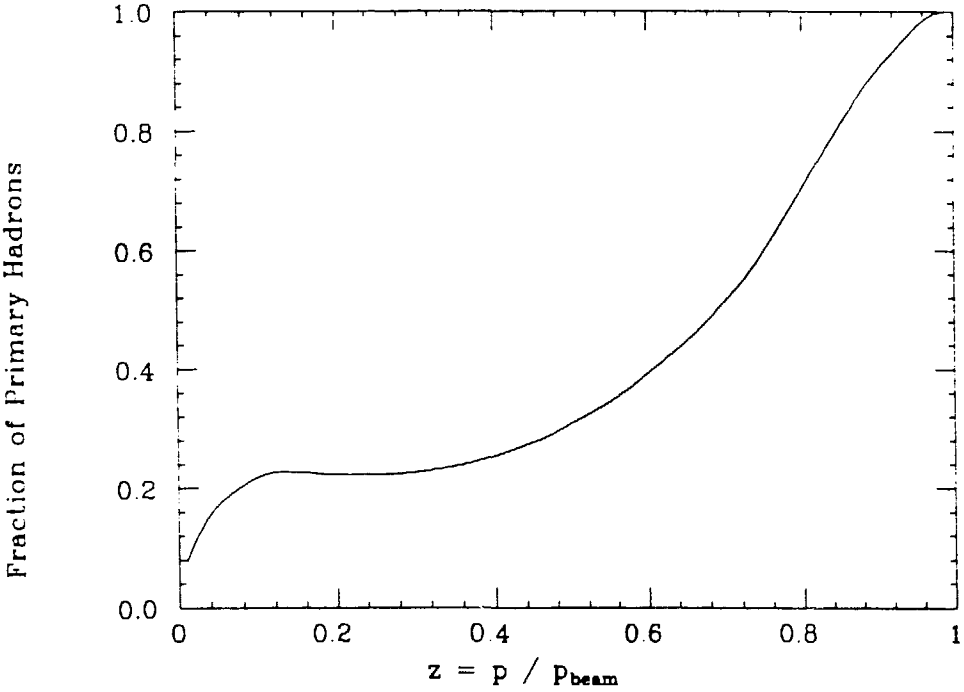

Figure 2.14 The fraction of charged pions, kaons and protons which are primary (i.e. not from resonance decays) as a function of $z = p/p_{beam}$, according to the Lund model version 5.3.

Chapter 3

PEP and the TPC/2γ Detector

3.1 The PEP e^+e^- Storage Ring

The data used in this analysis were collected between 1984 and 1986 with the TPC/2γ detector at the PEP e^+e^- storage ring. The PEP ring has a circumference of approximately 2.2 km, and is located at the end of the 3.2 km Stanford linear accelerator. The layout of PEP is shown in figure 3.1. The ring contains three bunches of electrons and three counter-rotating bunches of positrons, with a beam energy of 14.5 GeV, colliding at six interaction regions. The time between collisions is 2.45 μs and the beam current is typically 15 - 25 mA, resulting in an instantaneous luminosity of $10 - 25 \times 10^{30}$ cm^{-2} s^{-1}.

3.2 The TPC/2γ Detector: Overview

The TPC/2γ detector consists of a number of detector subsystems, most of which can be seen in figure 3.2. These include:

i) The inner drift chamber (IDC) [30].

ii) The time projection chamber (TPC) [31-41].

iii) The outer drift chamber (ODC) [30].

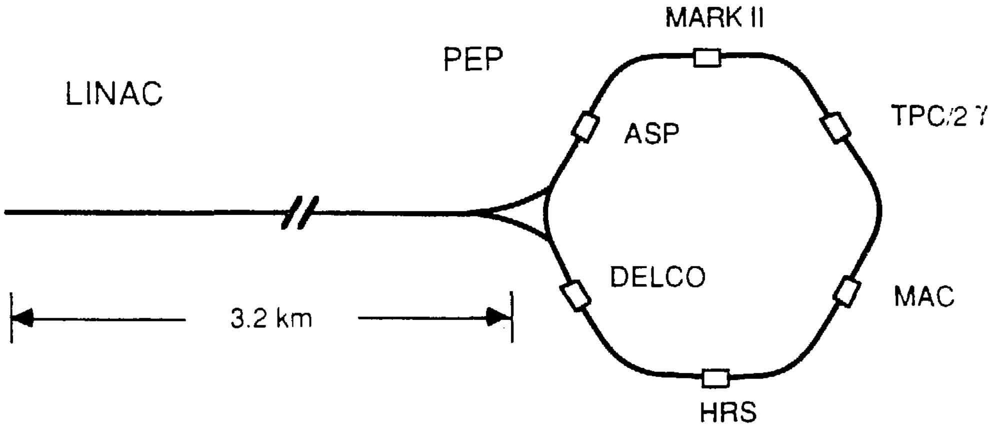

Figure 3.1 A schematic view of the SLAC linac and the PEP storage ring, showing the positions of the six detectors.

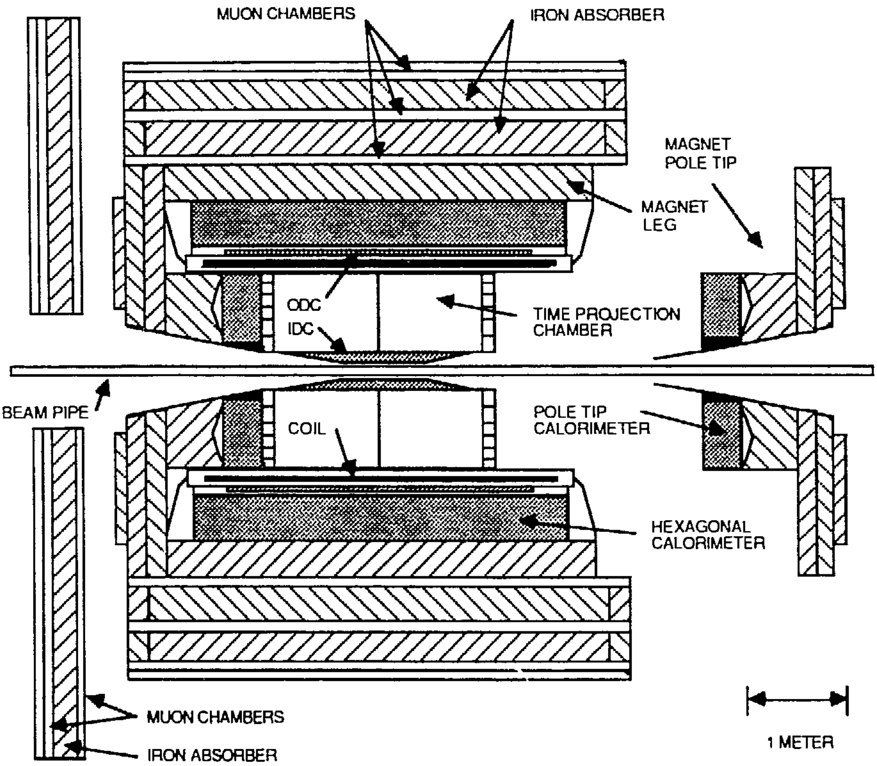

Figure 3.2 A schematic view of the TPC/2γ detector, with one pole tip opened. The PEP-9 detectors and one of the forward muon detectors are not shown.

Table 6.6 The ratios $K^{\pm}/\pi^{\pm}$, $(p, \bar{p})/\pi^{\pm}$ and $(p, \bar{p})/(\pi^{\pm} + K^{\pm})$ as a function of $z = p_{hadron}/p_{beam}$.

z interval	$K^{\pm}/\pi^{\pm}$	$(p, \bar{p})/\pi^{\pm}$	$(p, \bar{p})/(\pi^{\pm}+K^{\pm})$
0.025 - 0.030	0.0386 ± 0.0035	-	-
0.030 - 0.035	0.0551 ± 0.0043	-	-
0.035 - 0.040	0.0673 ± 0.0053	0.0322 ± 0.0058	0.0302 ± 0.0054
0.040 - 0.045	0.089 ± 0.012	0.0331 ± 0.0044	0.0304 ± 0.0040
0.045 - 0.050	0.091 ± 0.010	0.0426 ± 0.0049	0.0390 ± 0.0044
0.050 - 0.055	0.1042 ± 0.0080	0.0434 ± 0.0050	0.0393 ± 0.0045
0.055 - 0.060	0.112 ± 0.010	0.0441 ± 0.0052	0.0397 ± 0.0046
0.060 - 0.065	0.135 ± 0.022	0.0486 ± 0.0059	0.0429 ± 0.0051
0.065 - 0.070	0.145 ± 0.042	0.0453 ± 0.0056	0.0396 ± 0.0047
0.070 - 0.075	-	0.0612 ± 0.0074	-
0.075 - 0.080	-	0.053 ± 0.010	-
0.080 - 0.085	-	0.079 ± 0.024	-
0.085 - 0.090	-	0.075 ± 0.012	-
0.090 - 0.100	0.154 ± 0.047	0.085 ± 0.011	0.0736 ± 0.0081
0.100 - 0.110	0.211 ± 0.038	0.090 ± 0.023	0.074 ± 0.018
.			
.			
.			
.			
0.250 - 0.300	0.424 ± 0.027	0.104 ± 0.025	0.073 ± 0.018
0.300 - 0.350	0.446 ± 0.030	0.120 ± 0.024	0.083 ± 0.018
0.350 - 0.400	0.532 ± 0.040	0.140 ± 0.030	0.092 ± 0.020
0.400 - 0.500	0.537 ± 0.039	0.137 ± 0.026	0.089 ± 0.018
0.500 - 0.600	0.673 ± 0.067	0.120 ± 0.033	0.072 ± 0.020
0.600 - 0.700	0.477 ± 0.075	0.161 ± 0.044	0.109 ± 0.031
0.700 - 0.900	0.48 ± 0.11	0.138 ± 0.049	0.093 ± 0.034

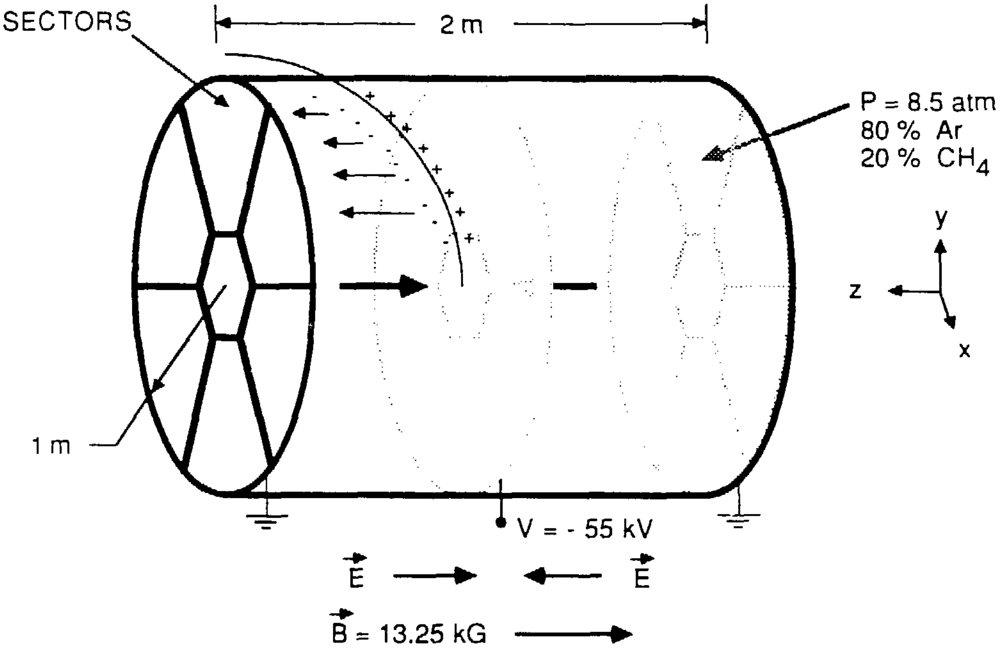

Figure 3.3 Schematic view of the time projection chamber.

As a charged particle traverses the TPC's gas volume, it creates pairs of electrons and positive ions along its path. The electrons drift towards the sense wires at the endcaps with a velocity of approximately 3.3 cm/μs, where they create an avalanche. The induced signal is amplified, shaped, digitized and recorded. Each sector contains 183 sense wires spaced 4 mm apart and 15 rows of 7.0 mm × 7.5 mm cathode pads, as shown in figure 3.4. Information on the track's projection onto the x-y plane is obtained from the location of the charge induced on the cathode pads. The z position of each track segment is determined by measuring the arrival time of the ionization at the sense wire. A track crossing all pad rows thus has 15 three-dimensional points from which its trajectory is determined. The pulse height information from the sense wires is used to determine the ionization rate ($\mathrm{d}E/\mathrm{d}x$) of the particle [33]. The $\mathrm{d}E/\mathrm{d}x$ measurement is discussed in detail in chapter 5.

The TPC contains 2196 sense wires and 13824 cathode pads. A schematic representation of the signal processing chain for a single channel is shown in figure 3.5 [34]. A preamplifier mounted on the sector integrates the collected charge and produces a step signal with a 5 μs decay time. This pulse is sent to a shaping amplifier in the electronics house, which produces a signal roughly Gaussian in shape with a 250 ns peaking time. The output of the shaping amplifier is sampled at 100 ns intervals and stored in a CCD analog shift register [35]. The maximum drift time in the TPC is approximately 30 μs, so the CCD must record 300 samples or "buckets", each corresponding to 3.3 mm of drift. After all of the ionization has reached the sectors and the pulses have been clocked into the CCDs, the clock frequency is changed from 10 MHz to 20 kHz for readout. Each CCD bucket is digitized with 9 bit accuracy. Buckets exceeding a preset (software controlled) threshold

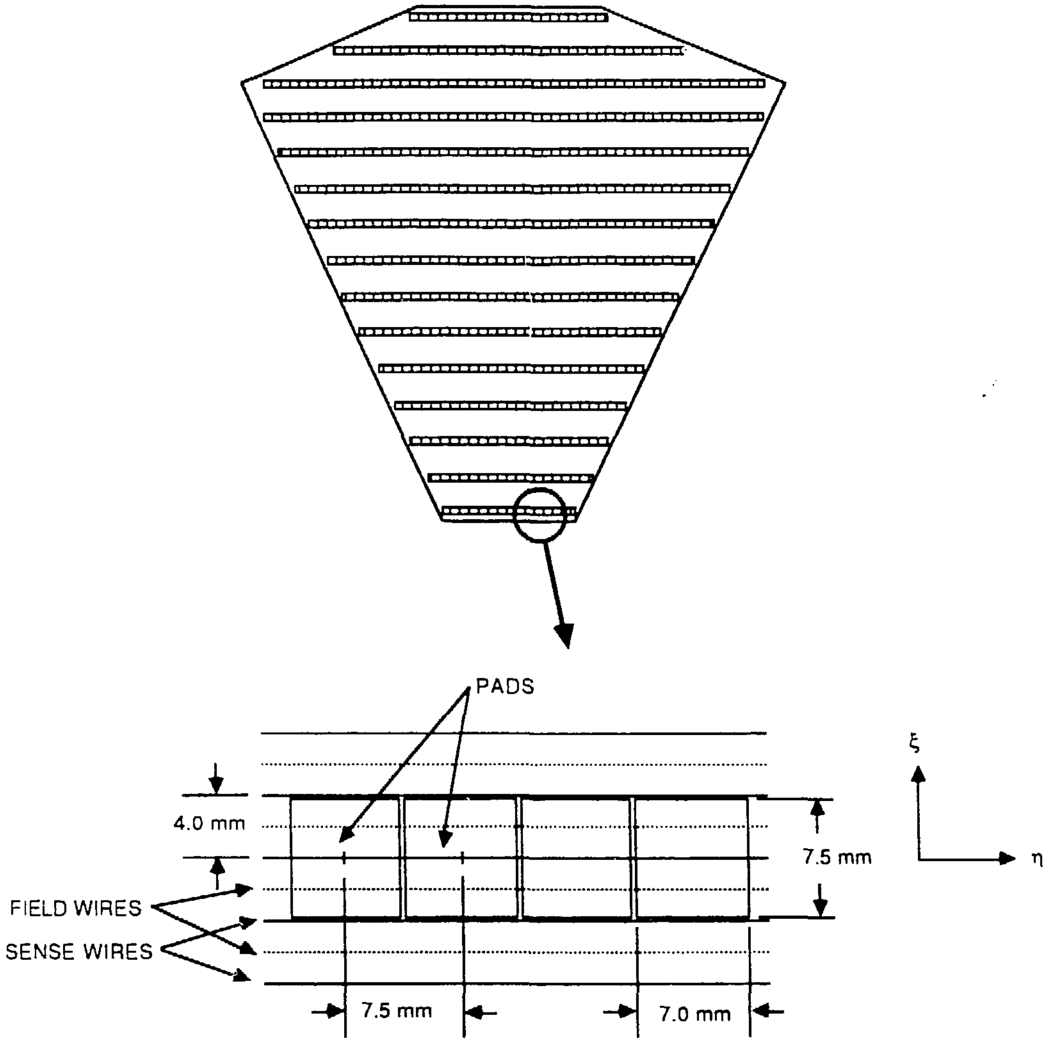

Figure 3.4 A TPC sector, with a detailed view of part of one of the pad rows.

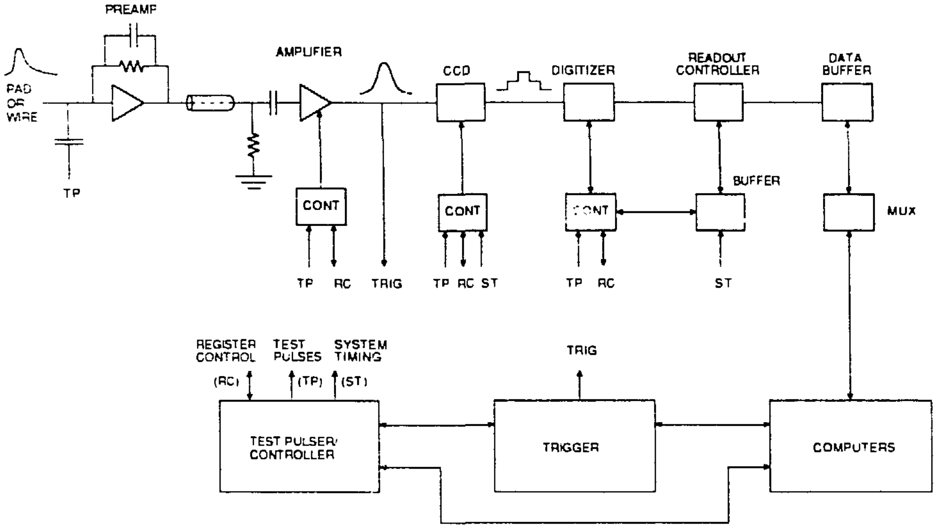

Figure 3.5 A schematic view of the signal processing chain for a single TPC channel.

are read out into the Large Data Buffer (LDB) and sent to the VAX 11/782 online computer. The readout thresholds are controlled by a PDP 11/70 computer.

3.4 Upgrades to the TPC

Prior to running in 1984, a number of upgrades were undertaken to improve the TPC's momentum resolution [36]. The 4 kG conventional coil was replaced with a 13.25 kG superconducting coil, and measures were taken to limit electrostatic distortions in the TPC. The upgrades resulted in an improvement in the momentum resolution from $(\Delta p/p)^2 = (6\%)^2 + (3.6\% \cdot p \text{ (GeV/c)})^2$ to $(\Delta p/p)^2 = (1.5\%)^2 + (0.065 \cdot p \text{ (GeV/c)})^2$.

The original PEP-4 proposal [31] called for the TPC to be placed in a 15 kG superconducting coil. The first such magnet suffered a fatal quench while still being tested. A 4 kG conventional coil was used during the 1982-1983 running cycles while a second superconducting solenoid was built. In September of 1983 the second superconducting coil was found to have a faulty suspension system due to errors in the mechanical design. A solution was implemented which involved reinforcing one end of the magnet with a stainless steel ring and installing a set of axial tie rods between the coil package and the cryostat. This coil has been used since autumn of 1984 at a current of 1900 A and a magnetic field of 13.25 kG.

One source of electrostatic distortions in the TPC was charge build-up on the field cages. The cages consist of a series of equipotential rings spaced every 5 mm and maintained at the proper potential by precision resistor chains. Charge build-up on the G-10 substrate between the rings led to distortions of the electric field. This problem originally led to track distortions on the order of several centimeters ("hooks") when the detector was tested in the summer of 1981. By increasing the width of the rings from 0.5 mm to 2.5 mm with a copper tape overlay (and hence increasing the ratio of conductor to insulator from 1:10 to 1:1) the distortions were reduced to the level of several millimeters for the 1982-1983 running cycle. A more permanent solution was implemented before the 1984 running cycle in which the 2.5 mm copper tape was removed and the field cages were coated with a resistive paint. The resistance of the paint is much lower than that of the G-10 substrate, but much higher than that of the resistors establishing the potentials of the rings, so that charge build-up between the rings is prevented.

Electrostatic distortions also occur if positive ions created in the avalanche at the sense wires are allowed to drift back into the TPC volume. This problem was solved by installing a electrical shutter or "gating grid" in front of the sectors [37]. The layout of the central membrane, gating grid, shielding grid, sense and field wires and cathode plane is shown in figure 3.6. The nominal potential of the grid, V_{GG}, is such that the electric field between the shielding and gating grids is the same as in the main drift volume of the TPC. In this configuration, the gating grid is transparent to charged particles from ionization. If, however, the potentials of alternate wires are set to $V_{GG} \pm \Delta V_{GG}$, then the field lines are changed in such a way that the grid is opaque to charged particles. Values of the potentials used are V_{GG} = -910 V and ΔV_{GG} = 90 V.

The gating grid is normally kept in the opaque state. When a pre-pretrigger signal (see section 3.5) is generated the grid is opened long enough for the ionization electrons to drift to the sense wires. The grid is then closed before the positive ions created at the sense wire, which travel much more

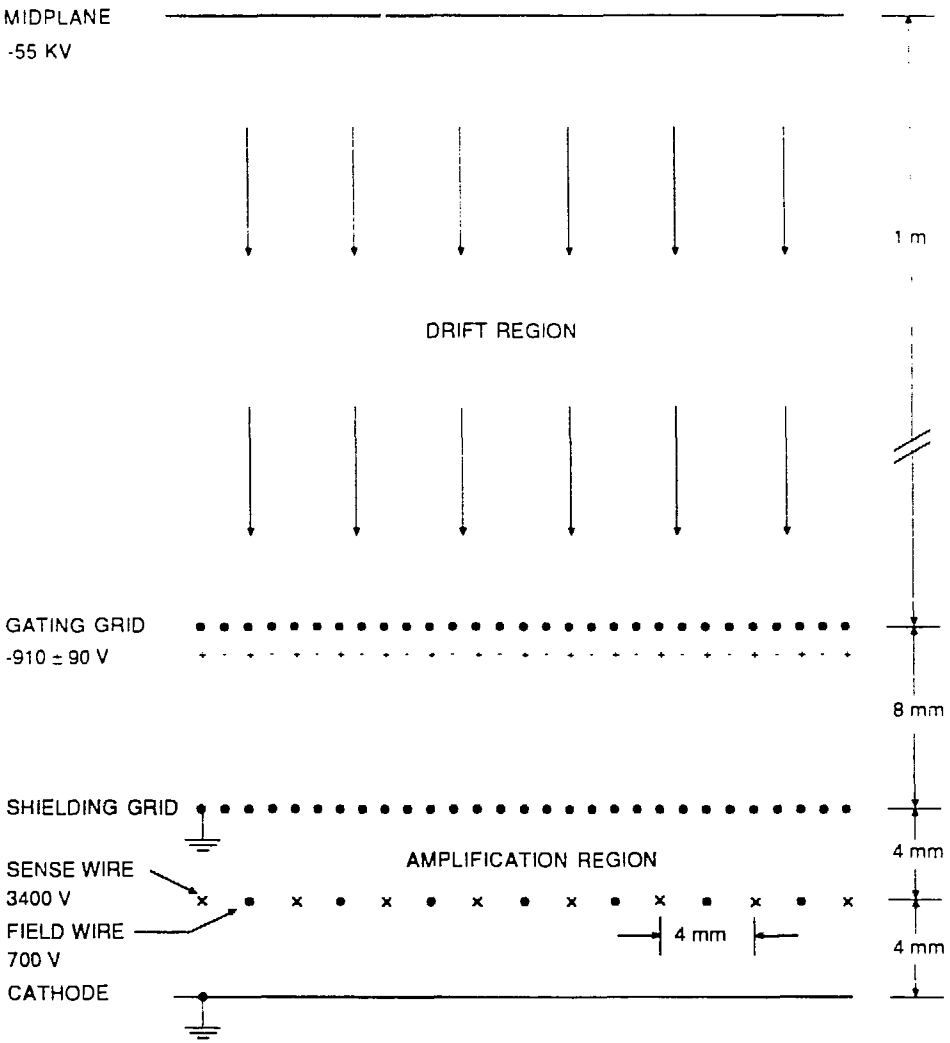

Figure 3.6 Layout of cathode, sense and field wire planes, shielding grid, gating grid and midplane.

slowly, are able to drift back into the TPC. Unfortunately, changing the voltage on the gating grid induces oscillations on the sense wires. These oscillations damp out only after about 3 μs, rendering signals collected during this time unusable. The usable drift length of the TPC is therefore only 91 cm, rather than 1 m.

3.5 The Trigger System

Although the time between beam crossings at PEP is 2.45 μs, events of sufficient interest to be recorded occur only at a rate of about 1-2 Hz. Furthermore, the time required for electrons to drift from the midplane to the sectors is approximately 30 μs, i.e. 12 beam crossing times, and the time required to read out a multihadronic event is about 20 ms, or over 8000 beam crossing times. A trigger system based on various prompt signals is used to determine whether or not to open the gating grid, collect the signals and read out the event. Triggers based on several of combinations of charged and neutral particle information are used. For multihadron events, these triggers are largely redundant. Here, only the charged-particle trigger is described. More comprehensive descriptions of the trigger system are given in references [38, 39].

The trigger system is divided into three levels: the pre-pretrigger, the pretrigger and the trigger. The pre-pretrigger requires evidence of two charged tracks separated by at least 90° in azimuth and at dip angles of less than 65°. A track is identified by combinations of signals in either the IDC and ODC or the IDC and TPC. Since the gating grid is initially closed, the TPC can collect ionization only from tracks passing through the sectors. The pre-pretrigger can also be satisfied by exceeding a calorimeter total-energy threshold. If no pre-pretrigger signal is generated, the electronics are reset in time for the next beam crossing. The total pre-pretrigger rate is typically 4-8 kHz.

If the pre-pretrigger condition is satisfied, the gating grid is opened allowing ionization to pass through to the sectors. The next level of the trigger, the pretrigger, is qualitatively similar to the pre-pretrigger, but with tighter requirements for the TPC information. The TPC uses ionization collected between 3.2 and 6.2 μs after the beam crossing time, corresponding to the region between 10 and 20 cm from the sectors. If no pretrigger signal is generated before 6.2 μs after beam crossing, the gating grid is closed and the electronics are reset. A pre-pretrigger signal with no pretrigger leads to a loss of three beam crossings. Other pretriggers involve combinations of charged and neutral information. The total pretrigger rate is typically 200-400 Hz.

If the pretrigger is satisfied, the gating grid is kept open for 30 μs, long enough for ionization anywhere in the chamber to be collected. The TPC wires are divided into groups of eight, known as majority units. A majority signal is generated if a certain number (typically four) of the eight wires have signals over threshold within a time window of 2-3 μs. The presence of a charged track coming from the interaction point is established by a series of majority signals for which decreasing radius is matched by a corresponding increase in drift time. The charged particle trigger requires two such tracks with dip angles less than 60°. Events satisfying the trigger condition are read out into the computer. The charged particle trigger rate is typically 0.5-1.0 Hz, and the total trigger rate (charged and neutral) is typically 1-2 Hz.

3.6 Calibration and Test Pulsing Systems

Variations in wire gain over the surface of a sector were measured before chamber assembly, resulting in a gain map for each sector. Wire gains were found to vary about 3%, mainly as a result of differences in wire diameter and wire-cathode spacing. Corrections to the gain map are made based on measurements using ^{55}Fe x-ray sources. Each sector has three ^{55}Fe source rods, at 0°, -15° and +30° from center, mounted directly behind the cathode plane. The rods can be positioned so that the sources line up with a row of small holes in the cathode, allowing the x-rays to create ionization near the wires. Calibration runs with the ^{55}Fe sources were performed approximately once per month. The long term stability was found to be better than 0.3%

A computer controlled test pulsing system is used to measure the gain and saturation characteristics of the electronics and to monitor system stability [40]. First, pedestals are measured corresponding to the amount of charge stored in the CCD when no test pulse is sent. Because of dark current leakage, the pedestal depends on how long the charge is stored in the CCD. Since charge is passed from bucket to bucket at 20 MHz while being clocked in, and at 10 kHz while being read out, the amount of time spent in the CCD depends on when the input is sampled relative to when the clock speed is changed. The pedestal is found to change by 1-2% of the pulse height of a minimum ionizing track depending on when the signal enters the CCD.

The shape of the gain curve is measured by sending pulses to the shielding grid which induce signals on the wires and pads. Pulses of eleven different amplitudes are sent and the response is parameterized using a spline fit. The capacitive coupling between the shielding grid and the wires is not known with sufficient accuracy to determine the overall scale from the test pulsing system. A scale factor is determined using both ^{55}Fe source runs and minimum ionizing pions from the data. With this procedure the gain characteristics can be measured to better than 1%.

3.7 Position Measurement

Position measurements are made primarily from pad information, with the sense wire information being used only to make small corrections. The pad signals receive contributions from effectively five sense wires: the one centered directly above the pad and the two adjacent wires on each side. Avalanches on these five wires typically induce signals above threshold on two or three pads. The signal on a pad can be parameterized by [41]:

$$H_P = \left(\sum_{i=-2}^{2} w_i H_i \right) e^{-\eta^2/2\sigma^2} \qquad (3.1)$$

where:

H_P = Pulse height on the pad,

i = Wire number, (0 for the wire centered on the pad; ±1, 2 for the adjacent wires.)

η = Distance along the pad row from the point of the avalanche to the center of the pad,

σ = Pad response rms width,

H_i = Pulse height on wire i,

w_i = Weight for wire i. ($w_0 = 0.239$, $w_1 = 0.117$, $w_2 = 0.0135$, $w_{-1} = w_1$, $w_{-2} = w_2$.)

The position of an avalanche along the pad row, η, is determined by fitting the measured pulse heights to equation 3.1. If the cluster contains three or more pads above threshold, the width, σ, is made an adjustable parameter. Otherwise, σ is estimated from the drift distance, L, and the angle between the track's projection onto the x-y plane and the direction normal to the sense wires, α. In order to compensate for fluctuations in the ionization detected by the five wires above a pad, a correction of the form

$$\Delta\eta = \left(\sum_{i=-2}^{2} i\, w_i H_i \Big/ \sum_{i=-2}^{2} w_i H_i \right) D \tan\alpha \tag{3.2}$$

is applied, where $D = 4$ mm is the spacing between sense wires.

The spatial resolution in the x-y plane, σ_{xy}, is estimated from cosmic ray data as a function of drift distance, L, and crossing angle, α. Track fits are performed in which one pad row is omitted, and x-y residuals are determined. The resolution is estimated from a Gaussian fit to the distribution of x-y residuals. Values for σ_{xy} vary between 120 and 200 μm depending on tan α, as shown in figure 3.7.

The z position of a pad cluster is determined from the CCD bucket information, as previously described. Ionization from a single track will typically produce 5 to 7 buckets over threshold. A parabola is fit to the three buckets with the most charge to determine the arrival time (and hence the initial z position) of the ionization. The z spatial resolution, σ_z, is determined in the same manner as σ_{xy}. Typical values for σ_z are from 160 to 250 μm, depending on the dip angle, λ, as shown in figure 3.8.

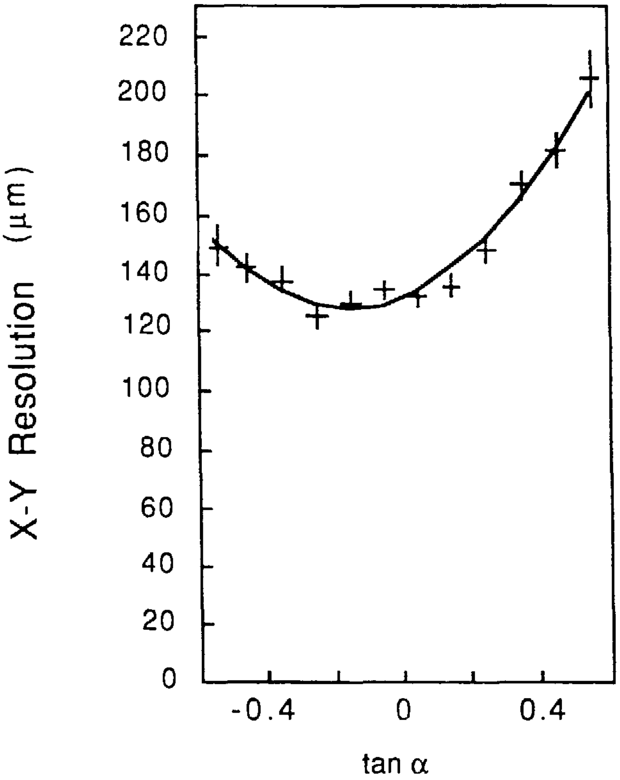

Figure 3.7 The position resolution, σ_{xy}, as a function of the tangent of the crossing angle, α.

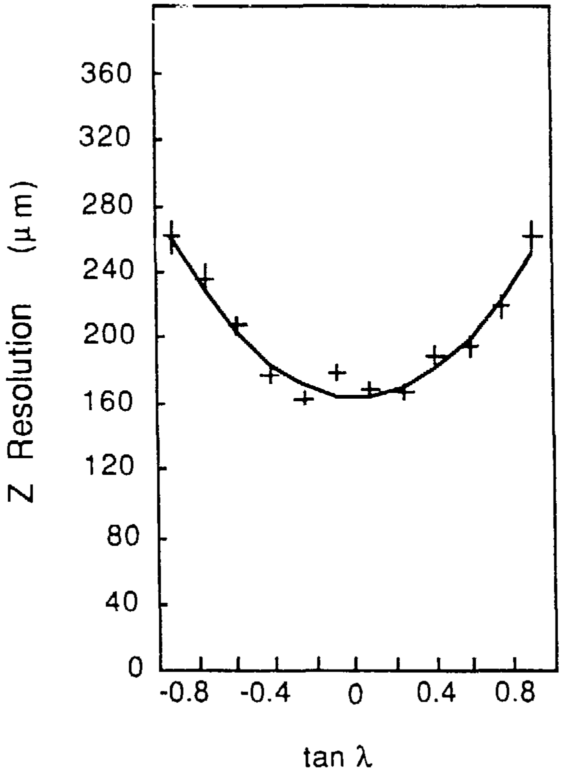

Figure 3.8 The position resolution, σ_z, as a function of the tangent of the dip angle, λ.

Chapter 4

Particle Identification by Measurement of Ionization Energy Loss

4.1 Introduction

The identity of a charged particle traversing the TPC is determined by simultaneously measuring its momentum and ionization rate ($\mathrm{d}E/\mathrm{d}x$). This technique is based on the fact that the $\mathrm{d}E/\mathrm{d}x$ of a particle depends only on its speed and the magnitude of its electric charge, which in this analysis is assumed to be plus or minus that of an electron. A scatter plot of $\mathrm{d}E/\mathrm{d}x$ vs. momentum for tracks from multihadron events (figure 4.1) shows clearly defined bands corresponding to electrons, muons, pions, kaons, protons and deuterons.

The momentum of a particle is determined by measuring its curvature in the TPC's 13.25 kG magnetic field. The momentum resolution is typically (depending on dip angle and track length) given by $(\Delta p/p)^2 = (1.5\%)^2 + (0.65\% \cdot p\ (\mathrm{GeV}/c))^2$. A detailed description of the momentum measurement is given in section 5.2.

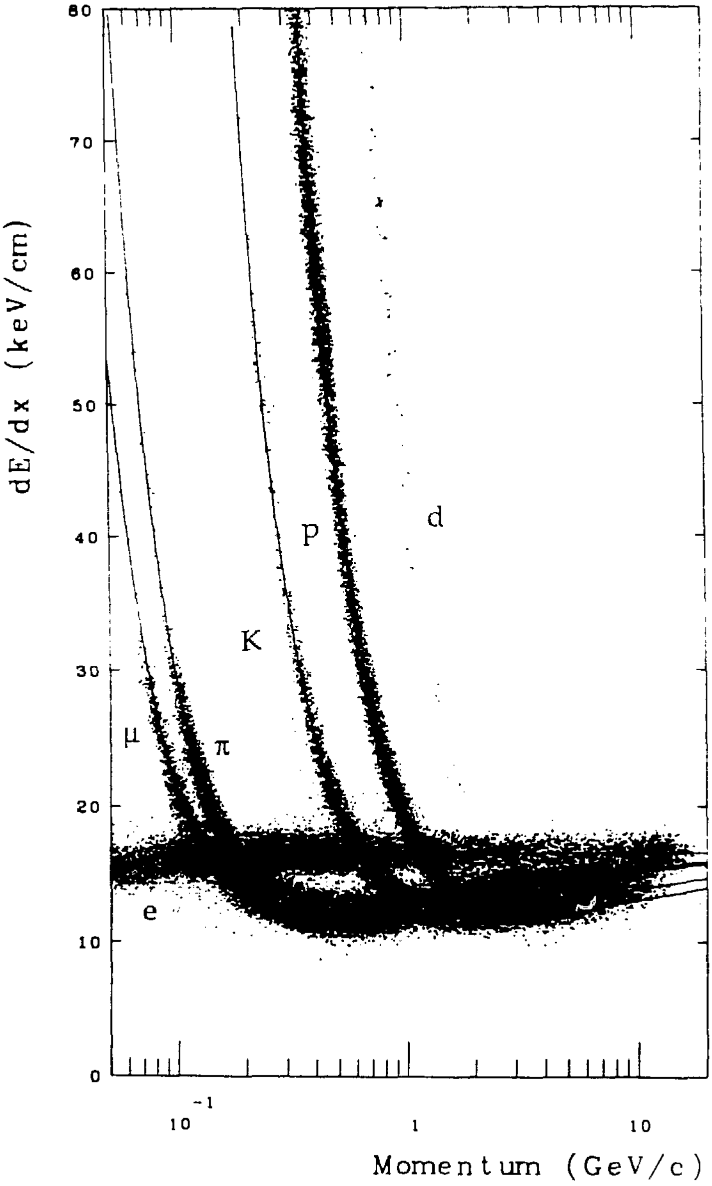

Figure 4.1 Scatter plot of dE/dx vs. momentum for tracks in events passing loose multihadron selection cuts.

The basic dependence of dE/dx on velocity can be seen in figure 4.1. For slow speeds ($\beta < 0.96$) the dE/dx is proportional to $1/\beta^2$, leading to well separated bands of highly ionizing particles. For $\beta > 0.96$ (the "relativistic rise region") the dE/dx increases logarithmically. This is due to the relativistic increase in the particle's transverse electric field, and hence its ionizing power. As β increases further, the relativistic rise is eventually stopped at what is known as the Fermi plateau. This phenomenon is known as the density effect, and is caused by the polarization of the medium, leading to an effective limit in the range of the particle's electric field [44, 45].

Note that ionization values between 12 1 and 16.6 keV/cm correspond to two values of velocity, leading to regions of ambiguity where the bands of different particle species cross. At momenta higher than that of the kaon-proton crossover ($p > 3.5$ GeV/c) there is only a 1 to 1.5 keV/cm separation between the pion and kaon bands, and only 0.5 to 1 keV/cm between kaons and protons. The relative dE/dx resolution is approximately 3.5%, corresponding to a 2 to 3.5 standard deviation separation between pions and kaons, and 1 to 2 standard deviations between kaons and protons. Hence, a particle's identity cannot always be established on a track-by-track basis, and a statistical technique must be used to determine the relative abundances of the various particle types. As input to this procedure, one requires an estimate of each particle's momentum and dE/dx, and in addition, an accurate estimate of the expected dE/dx and dE/dx resolution as a function of momentum and particle type.

4.2 Energy Loss in the TPC: Theoretical Considerations

As a charged particle passes through the gas volume of the TPC (80% Argon, 20% CH_4, at a pressure of 8.5 atmospheres) it loses energy through interactions with the electrons of the gas molecules, resulting in the production of electrons and positive ions (primary ionization). (Energy loss due to Cherenkov radiation and interaction with atomic nuclei is comparatively small and may be neglected.) The primary electrons can collide with neighboring gas molecules to produce additional (secondary) ionization. The electrons, primary and secondary, drift axially to the sense wires of the TPC sectors, where they create an avalanche. Since the sense wires are spaced 4 mm apart, each measurement corresponds to the passage of the particle through a gas layer of about 4 to 8 mm, depending on the track's dip angle, azimuth and momentum.

The number of primary ionization-producing collisions for a particle traversing a 5 mm layer of TPC gas is on the order of 100, and the fluctuations in this number obey Poisson statistics. These fluctuations are fairly small: about 10% for a single gas layer, or 1% for a track traversing most of the TPC gas volume. The number of primary collisions cannot, however, be directly measured. Instead, one measures the total number of electrons produced, primary plus secondary, which leads to a fundamental difficulty in the measurement of ionization energy loss: Relatively rare primary collisions resulting in large energy loss, and hence in a large number of secondary electrons, account for a comparatively large fraction of the total number of electrons produced. Because such collisions are comparatively rare, they lead to large fluctuations (25%-50%) in the total amount of ionization produced in a single gas layer.

In this analysis it is assumed that the number of electrons produced is proportional to the amount of energy the particle loses, Δ. A typical distribution of energy loss $f(\Delta; \beta, x)$ for a particle of speed $\beta \approx 0.96$ traversing a gas layer of thickness $x \approx 5$ mm is shown in figure 4.2. For adequate particle identification a dE/dx resolution of a few percent is needed. This is achieved by sampling the distribution (i.e. measuring the track's ionization rate) a large number of times. It is for this reason that each TPC sector is equipped with 183 anode sense wires. Signals induced on the pads also provide some dE/dx information, but this is not used in this analysis.

From the set of dE/dx measurements, one could in principle estimate the particle's speed, β, by means of a maximum likelihood fit to the energy loss distribution, $f(\Delta; \beta, x)$, in which β is an adjustable parameter. This procedure is too complicated, however, to be carried out on a track-by-track basis, particularly since it is difficult to obtain an accurate parameterization of $f(\Delta; \beta, x)$. (Recall that x is different for each track, and would therefore need to be included as a parameter.) Instead, it is convenient to form a single estimator of the distribution, which ideally should be a sensitive a function of β, and also should be as robust as possible. (i.e. it should have a small statistical error for a given number of samples.) In order to avoid the fluctuations caused by large energy losses, the mean of the lowest 65% of the individual dE/dx measurements is used. This quantity, hereafter referred to as the truncated mean dE/dx or simply the "dE/dx" of a particle, is assumed, for the purposes of theoretical calculations, to be proportional to the most probable value of $f(\Delta; \beta, x)$. To establish an energy scale for the data, the truncated mean dE/dx for minimum ionizing pions is assigned a value of 12.1 keV/cm, based on preliminary theoretical calculations.

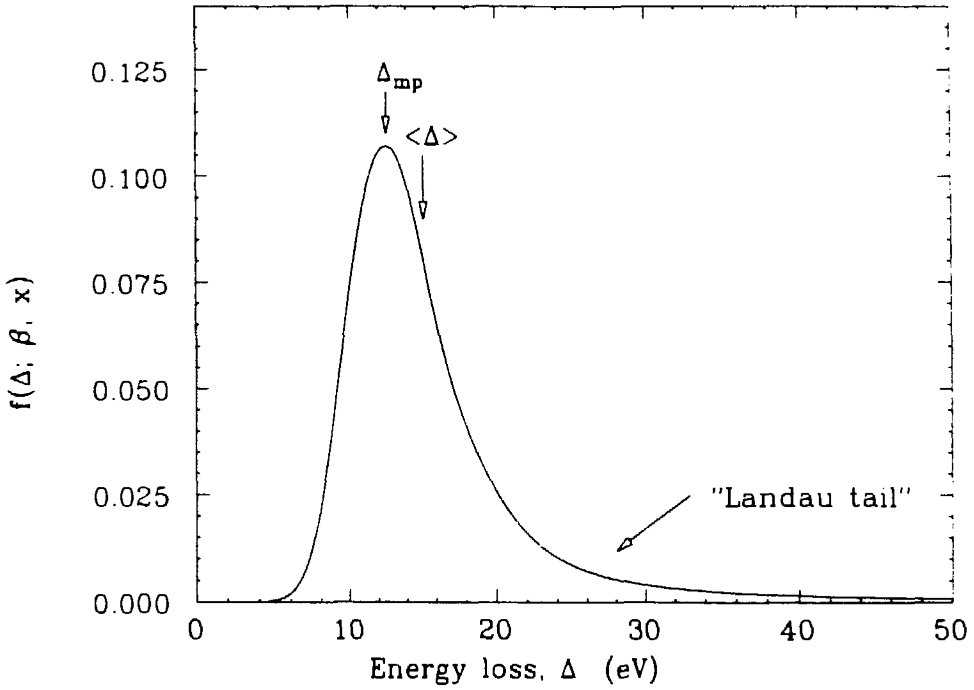

Figure 4.2 Energy loss distribution, $f(\Delta;\ \beta, x)$ for a particle of speed $\beta \approx 0.96$ traversing a gas layer of thickness $x \approx 5$ mm.

4.3 General Theory of Ionization Energy Loss

We would like to derive the energy loss distribution, $f(\Delta; \beta, x)$, or at least its most probable value, as a function of the parameters β and x. This was done by Landau [46] by relating $f(\Delta; \beta, x)$ to the differential cross section, $d\sigma/dE$, for losing an amount of energy E in a collision with an atomic electron. One starts with the Laplace transform of $f(\Delta; \beta, x)$:

$$\bar{f}(p; \beta, x) = \int_0^\infty e^{-p\Delta} f(\Delta; \beta, x)\, d\Delta. \tag{4.1}$$

This is related to the energy loss cross section, $d\sigma/dE$, by [47]

$$\bar{f}(p; \beta, x) = \exp\left(-x \int_0^\infty (1 - e^{-pE})\, \rho \frac{d\sigma}{dE}\, dE \right), \tag{4.2}$$

where ρ is the number of atomic electrons per unit volume. This can be inverted numerically or (for example) by

$$f(\Delta; \beta, x) = \frac{1}{2\pi i} \int_{\sigma - i\infty}^{\sigma + i\infty} e^{p\Delta}\, \bar{f}(p; \beta, x)\, dp. \tag{4.3}$$

For energy transfers large compared to atomic binding energies, $d\sigma/dE$ is essentially the Rutherford cross section:

$$d\sigma/dE = \begin{cases} \dfrac{2\pi e^4}{mc^2} \dfrac{1}{\beta^2 E^2} & E \geq E' \\[2ex] 0 & E < E' \end{cases} \tag{4.4}$$

where m is the electron mass. The minimum energy transfer, E', corresponds to a collision time on the order of an orbital period for an atomic electron. Landau's treatment is equivalent to using

$$\ln E' = \ln\left(\frac{I^2}{2\, m\, c^2\, \beta^2\, \gamma^2}\right) + \beta^2 \tag{4.5}$$

where I is the ionization potential of the atom. (I = 13.5 eV · Z.)

$f(\Delta;\, \beta,\, x)$ is found using the Laplace transform procedure outlined above, and can be expressed as the product of two terms:

$$f(\Delta;\, \beta,\, x) = \frac{1}{\xi}\, \phi\,(\lambda). \tag{4.6}$$

The variables ξ and λ are defined by

$$\xi = \frac{2\, \pi\, e^4\, \rho\, x}{m\, c^2\, \beta^2}\,, \tag{4.7}$$

$$\lambda = \frac{1}{\xi}\left(\Delta - \xi\left(\ln \frac{\xi}{E'} + 1 - \mathrm{C}\right)\right) \tag{4.8}$$

where C = 0.577 is Euler's constant. $\phi\,(\lambda)$ is the Landau distribution, given by

$$\phi\,(\lambda) = \frac{1}{2\pi i} \int_{\sigma - i\infty}^{\sigma + i\infty} \exp\,(\, u\, \ln u + \lambda\, u\,)\, du. \tag{4.9}$$

The famous "Landau tail" of $\phi\,(\lambda)$ is the source of the large energy-loss fluctuations mentioned in section 4.2. The maximum of $\phi\,(\lambda)$ occurs at λ = - 0.225, leading to a most probable energy loss, Δ_{mp}, of

$$\Delta_{mp} = \xi\left(\ln \frac{\xi}{E'} + 0.198\right). \tag{4.10}$$

(In fact, the additive constant in equation 4.10 was originally determined by Landau to be 0.37. A calculational error was later discovered by Maccabee and Papworth [48], who provided the corrected value of 0.198.) Note that the relativistic rise in equation 4.10 comes entirely from the fact the the minimum energy transfer, E', depends on the particle's speed.

Equation 4.10 for the most probable energy loss is only valid to the extent that $d\sigma/dE$ is accurately described by the Rutherford cross section given in equation 4.4. This corresponds to the case where typical energy transfers are large compared to the maximum binding energy, so that the atomic electrons can be treated as free particles. In reality, the probability to transfer an amount of energy, E, to an electron is strongly peaked at the binding energies corresponding to the various atomic levels. An energy-loss cross section which takes into account this effect is given by [49]:

$$\frac{d\sigma}{dE} = \left(\frac{d\sigma}{dE}\right)_{resonance} + \left(\frac{d\sigma}{dE}\right)_{Rutherford} , \tag{4.11a}$$

$$\left(\frac{d\sigma}{dE}\right)_{resonance} = \tag{4.11b}$$

$$\frac{2\pi e^4}{m c^2} \frac{f(E)}{\beta^2 E} \left(\ln \left(\frac{2 m c^2 \beta^2 \gamma^2}{E \mid 1 + \beta^2 \gamma^2 (1 - \varepsilon(E)) \mid} \right) - \beta^2 \operatorname{Re}(\varepsilon(E)) \right)$$

$$\left(\frac{d\sigma}{dE}\right)_{Rutherford} = \frac{2\pi e^4}{m c^2} \frac{1}{\beta^2 E^2} \int_0^E f(E')\, dE' , \tag{4.11c}$$

where $\varepsilon = \varepsilon_1 + i\varepsilon_2$ is the dielectric constant of the medium and $f(E)$ is the oscillator strength. These are related by

$$\varepsilon_1(E) = 1 - \frac{4\pi \rho\, \alpha (\hbar c)^3}{m c^2 E^2} \int_0^E f(E')\, dE', \tag{4.12}$$

$$\varepsilon_2(E) = \frac{2\pi^2 \rho \, \alpha \, (\hbar c)^3}{m c^2 E} f(E) \; . \tag{4.13}$$

The oscillator strength is proportional to the atomic photoabsorption cross section (for atomic number Z):

$$f(E) = \frac{m c^2}{2\pi^2 \alpha \, (\hbar c)^2 Z} \sigma_\gamma(E). \tag{4.14}$$

The first term in equation 4.11a, $(d\sigma/dE)_{resonance}$, is proportional to $f(E)$ and therefore peaks at energies corresponding to atomic energy levels. This term shows the origin of the Fermi plateau: for $\beta > 0.96$, but $\beta^2\gamma^2 (1 - \varepsilon) \ll 1$, the cross section rises as ln $\beta\gamma$. For sufficiently large $\beta\gamma$, the denominator of the logarithm becomes proportional to $\beta^2\gamma^2$, and $(d\sigma/dE)_{resonance}$ becomes independent of the particle's speed. $(d\sigma/dE)_{Rutherford}$ is essentially the Rutherford cross section multiplied by the fraction of electrons bound by an energy less than E.

4.4 Model for the Most Probable Energy Loss in the TPC

Ideally, one could plug the expression for $d\sigma/dE$ given in equation 4.11 into the expression for $\bar{f}(p; \beta, x)$ (equation 4.2) invert the Laplace transform to find the energy loss distribution, and then determine its most probable value, Δ_{mp}. We choose the simpler approach of finding Δ_{mp} using the resonance and Rutherford cross sections separately, and then simply adding the results [50]. In other words, we make the approximation:

$$\Delta_{mp} \approx (\Delta_{mp})_{resonance} + (\Delta_{mp})_{Rutherford} \; . \tag{4.15}$$

For the oscillator strength, $f(E)$, it is convenient to use different approximations for the resonance and Rutherford terms. For the resonance term, the following parameterization was obtained from photoabsorption data [50, 51]: (See figure 4.3a.)

$$f(E) = \sum_{j\,=\,\mathrm{gas}} \sum_{i\,=\,\mathrm{level}} \frac{\rho_j}{\rho_{\mathrm{Ar}} + \rho_{\mathrm{CH_4}}} \, w_{ij} \, f_{ij}(E) \; , \tag{4.16a}$$

$$f_{ij}(E) = \begin{cases} \dfrac{s_{ij} - 1}{E_{ij}} \left(\dfrac{E}{E_{ij}} \right)^{-s_{ij}} & E \geq E_{ij} \\ 0 & E < E_{ij} \, . \end{cases} \tag{4.16b}$$

The index j is summed over gas types, argon and methane, ρ_j is the number of electrons per unit volume from gas type j, i is summed over the atomic energy levels, and the weights, w_{ij}, sum to one for each component of the gas. The gas mixture of 80% Ar, 20% CH_4, by number of molecules, at a temperature of 21° C corresponds to electron densities of $\rho_{\mathrm{Ar}} = 3.05 \times 10^{21}$ cm^{-3} and $\rho_{\mathrm{CH_4}} = 4.24 \times 10^{20}$ cm^{-3}. Argon is approximated as having four energy levels, and methane as having two. Values for the parameters w_{ij}, E_{ij}, and s_{ij} are shown in table 4.1. The resulting real and imaginary parts of the dielectric constant are shown in figures 4.3b and 4.3c.

The mean number of resonance collisions per unit length can be found by integrating $(d\sigma/dE)_{resonance}$, multiplied by the appropriate electron density, over energy. For this, the energy dependence inside the logarithm can be approximated as being constant, and set equal to the mean ionization potential, E_{ij}', for energy level i, gas j. This is defined by

$$\ln E_{ij}' = \int_0^{\infty} f_{ij}(E) \ln E \, dE \; , \tag{4.17}$$

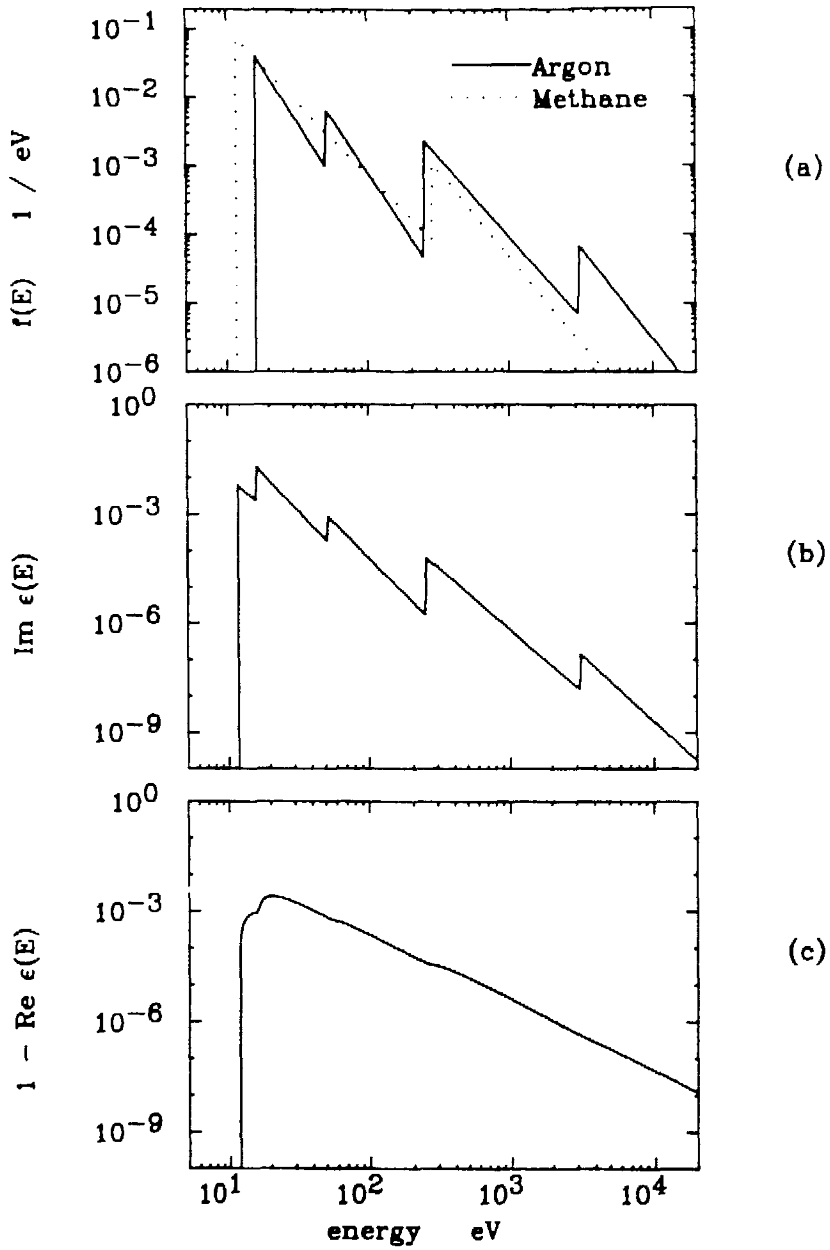

Figure 4.3 (a) The oscillator strengths, *f*(*E*), for argon and methane. *f*(*E*) for the argon-methane mixture is given by a weighted sum of the two curves (equation 4.16). (b) The imaginary part of the dielectric constant, from equations 4.12 and 4.16. (c) One minus the real part of the dielectric constant, from equations 4.13 and 4.16.

Table 4.1 Parameters used in the model for ionization energy loss described in section 4.4. The index j refers to the gas, and i to the energy level. The "outer" level of CH_4 combines hydrogen with the L-level of carbon.

Atom	Level	w_{ij}	E_{ij} (eV)	s_{ij}
Ar	K	0.111	3206.0	2.75
Ar	L	0.444	248.0	2.29
Ar	M	0.133	52.0	3.20
Ar	M	0.311	15.8	3.20
CH_4	K	0.2	283.	2.52
CH_4	"outer"	0.8	11.5	2.15

yielding

$$E_{ij}' = E_{ij}\ \exp\left(\frac{1}{s_{ij} - 1}\right). \tag{4.18}$$

Using this to integrate $(\mathrm{d}\sigma/\mathrm{d}E)_{resonance}$, one obtains for the mean number of collisions per unit length for electrons of energy level i, gas j:

$$\left(\frac{\mathrm{d}N}{\mathrm{d}x}\right)_{ij} = \frac{2\pi e^4 \rho_j}{m\, c^2 \beta^2}\ \frac{w_{ij}}{E_{ij}}\ \frac{s_{ij} - 1}{s_{ij}} \times$$

$$\left(\ln\left(\frac{2\, m\, c^2\, \beta^2\, \gamma^2}{E_{ij}'\ |\, 1 + \beta^2 \gamma^2 (1 - \varepsilon(E_{ij}'))\, |}\right) + 1 - \beta^2\ \mathrm{Re}\,(\varepsilon\,(E_{ij}'))\right). \tag{4.19}$$

Since the resonance cross section is strongly peaked at the binding energies, the most probable energy loss for a given gas and energy level can be approximated by the most probable number of collisions multiplied by the mean ionization potential for that level. The number of collisions in a gas layer of thickness x follows a Poisson distribution, the most probable value of which is one half less than its mean. This yields

$$(\Delta_{mp})_{resonance} = \sum_{j\,=\,\mathrm{gas}}\ \sum_{i\,=\,\mathrm{level}} \left(\left(\frac{\mathrm{d}N}{\mathrm{d}x}\right)_{ij} x\ -\ \frac{1}{2}\right) E_{ij}'\ . \tag{4.20}$$

For the Rutherford term, it is easier to approximate $f(E)$ as a sum of delta functions centered about the mean ionization potentials, using the same weights, w_{ij}, as before:

$$f(E)\ =\ \sum_j \sum_i \frac{\rho_j}{\rho_{\mathrm{Ar}} + \rho_{\mathrm{CH_4}}}\ w_{ij}\ \delta(\, E\ -\ E_{ij}'\,)\,. \tag{4.21}$$

This breaks the Rutherford cross section into six terms: four for argon and two for methane. Each term is of the same form as the Rutherford cross section given in equation 4.4, which was used to obtain equation 4.10 for the most probable energy loss. $(\Delta_{mp})_{Rutherford}$ can therefore be approximated as

$$(\Delta_{mp})_{Rutherford} \approx \sum_{j\,=\,\text{gas}} \; \sum_{i\,=\,\text{level}} w_{ij}\, \xi_j \left(\ln \frac{\xi_j}{E_{ij}'} + 0.198 \right). \tag{4.22}$$

Using the definition of E_{ij}', (equation 4.17,) this reduces to

$$(\Delta_{mp})_{Rutherford} = \sum_{j\,=\,\text{gas}} \xi_j \left(\ln \frac{\xi_j}{E_j'} + 0.198 \right), \tag{4.23}$$

where E_j' is the mean ionization potential for gas j, defined by

$$E_j' = \sum_{i\,=\,\text{level}} \int_0^\infty w_{ij}\, f_{ij}(E) \ln E \, dE\,. \tag{4.24}$$

This yields mean ionization potentials of 208.0 eV for Argon and 49.9 eV for methane. Note that $(\Delta_{mp})_{Rutherford}$ is not directly proportional to the gas layer thickness, x, but rather to $x \ln x$. For purposes of the energy loss model, $(\Delta_{mp})_{Rutherford}$ is evaluated at $x = 5$ mm. In the data, the dE/dx of each track is corrected for the dependence on gas layer thickness.

The final expression for the most probable energy loss per unit length is obtained by summing equations 4.20 and 4.23 and dividing by the gas layer thickness, x. (See figure 4.4a.) Note that only the resonance term contributes to the relativistic rise. This results from the fact that the minimum energy transfers for the six terms in the Rutherford cross section were set equal to the mean ionization potentials, E_{ij}', independent of the speed of the particle. The contributions from the various energy levels to $(\Delta_{mp})_{resonance}$ are shown in figure 4.4b. From this it can be seen that most of the relativistic rise comes from collisions with the L-shell electrons in argon.

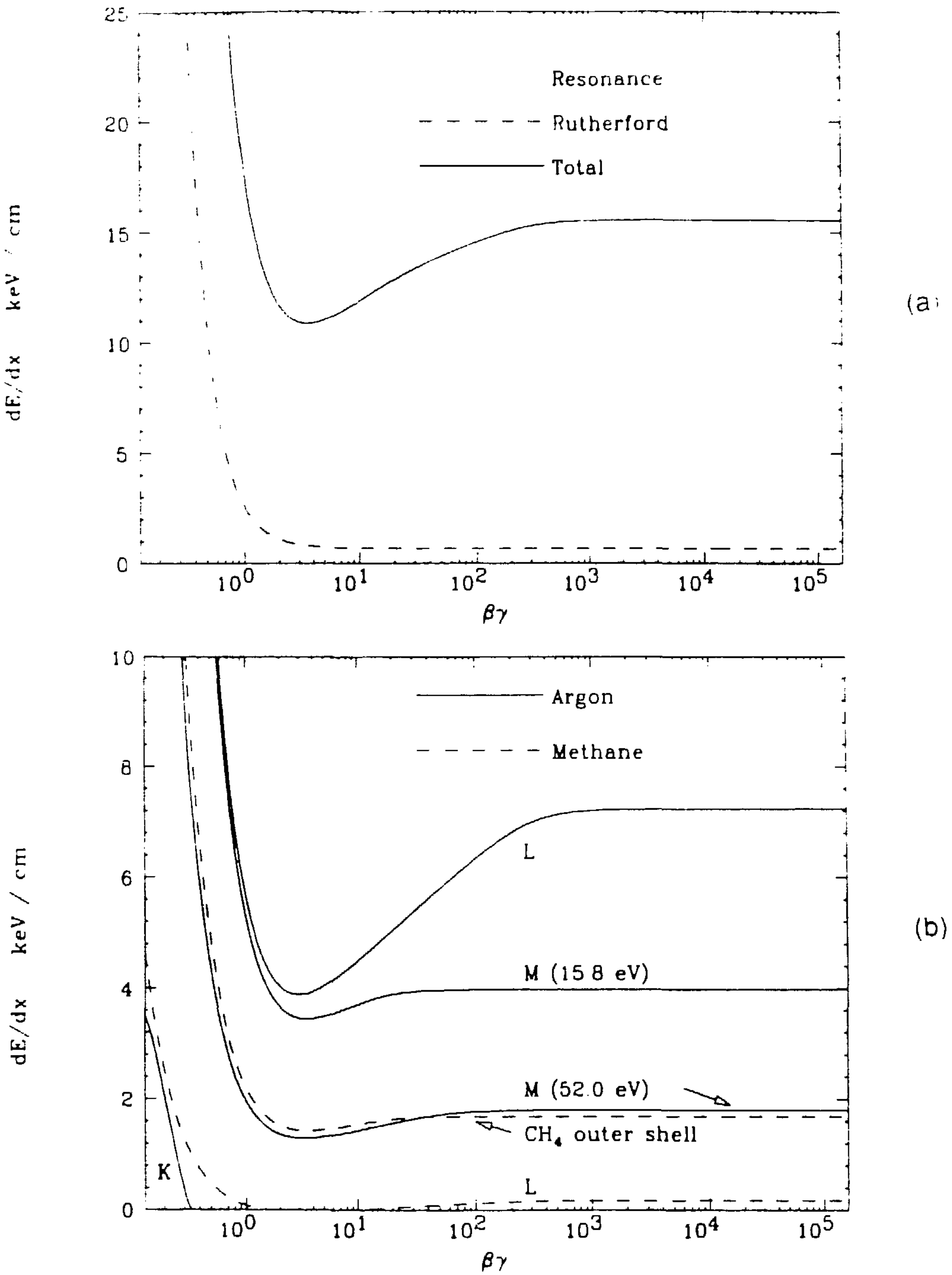

Figure 4.4 (a) Model prediction for the most probable dE/dx as a function of $\beta\gamma$, showing the contributions of the resonance and Rutherford terms. (b) Contributions to the resonance term of the most probable dE/dx by energy level.

4.5 Fit of the d*E*/d*x* Model to Data

As mentioned in section 4.1, the required accuracy for the expected dE/dx as a function of velocity is approximately 0.2%. In order to achieve this, the model for $(dE/dx)_{mp}$ described in the previous section was parameterized and fit to data from a variety of track samples. These included protons from the $1/\beta^2$ region, pions from the minimum ionizing and relativistic rise regions, cosmic ray muons, conversion pair electrons and Bhabha electrons (i.e. electrons from $e^+e^- \rightarrow e^+e^-$). The protons, pions and conversion pair electrons were taken from multihadron events (i.e. the same events we eventually want to study) so that systematic errors from gain variations and track environment cancel.

In order to have track samples of sufficient purity, particles were taken from regions where identification by dE/dx does not depend crucially on the dE/dx measurement (e.g. the $1/\beta^2$ region) or where identification is provided by means other than dE/dx. (For example, the cosmic ray muons are identified by their ability to penetrate the iron in front of the muon chambers.) An exception to this is the pion sample, which is not well separated from kaons and protons in the relativistic rise region. Here, a maximum-likelihood fit was performed for the dE/dx distribution of tracks within a narrow momentum interval. The technique is essentially the same as that used to determine the charged hadron fractions, and is described in detail in section 6.3. For purposes of obtaining information on the dE/dx as a function of velocity, an extra adjustable parameter was used corresponding to the mean dE/dx of the pions in the momentum interval. The pions from the relativistic rise region are crucial for establishing the accuracy of the dE/dx versus velocity curve.

The model prediction was parameterized to allow translations and linear transformations in $\ln \beta\gamma$ and $\mathrm{d}E/\mathrm{d}x$. In other words,

$$\left(\frac{\mathrm{d}E}{\mathrm{d}x}\right)_{fit}(\beta\gamma) = C \cdot \left(\frac{\mathrm{d}E}{\mathrm{d}x}\right)_{model} + D \tag{4.25}$$

where $(\mathrm{d}E/\mathrm{d}x)_{model}$ is evaluated at

$$(\ln \beta\gamma)_{model} = A \cdot \ln \beta\gamma + B. \tag{4.26}$$

The data and resulting fit are shown in figure 4.5. The χ^2 per degree of freedom is 1.50. The values obtained for the parameters are:

$A = 0.986$

$B = -0.055$

$C = 0.999$

$D = 1.532$ keV/cm

The fact that $A \approx 1$ and $B \approx 0$ indicates the extent to which the velocity scales agree between theory and experiment. The fact that D is not zero, but rather represents about a 10% shift for particles between the minimum ionizing and plateau regions, can be interpreted in several ways. It could be the result of a pedestal subtraction problem in the data, or (more likely) an underestimate of the Rutherford contribution to the most probable $\mathrm{d}E/\mathrm{d}x$ in the model. For purposes of data analysis, the distinction is unimportant. What is important is that the parameterization of the model fits the data well. Figure 4.6 shows the $\mathrm{d}E/\mathrm{d}x$ for cosmic ray muons and pions from the relativistic rise region divided by the predicted $\mathrm{d}E/\mathrm{d}x$. The dashed lines

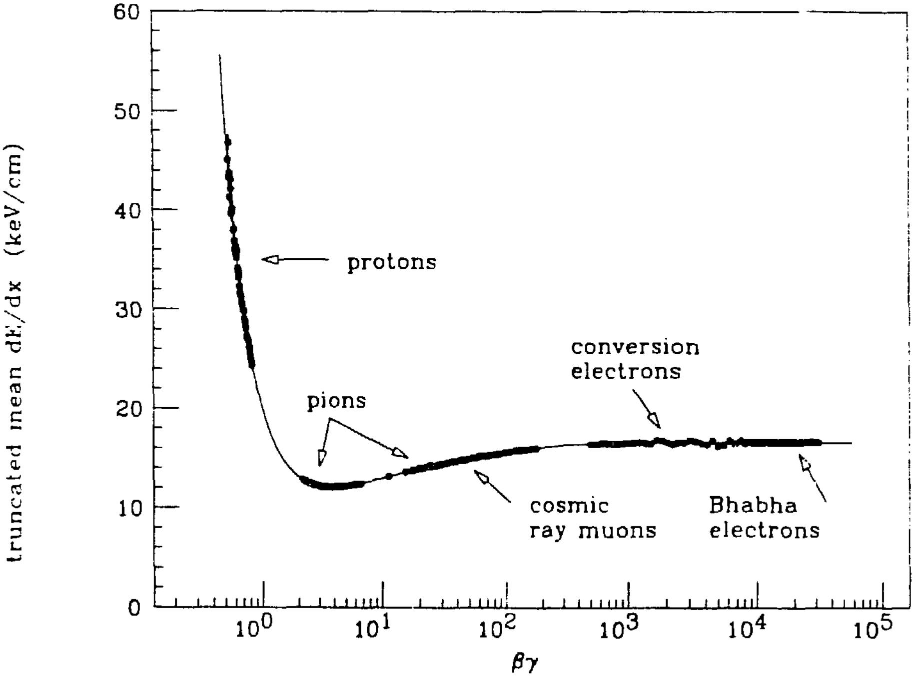

Figure 4.5 Data points: the truncated mean dE/dx from several track samples as a function of $\beta\gamma$. Curve: the parameterization of the dE/dx model.

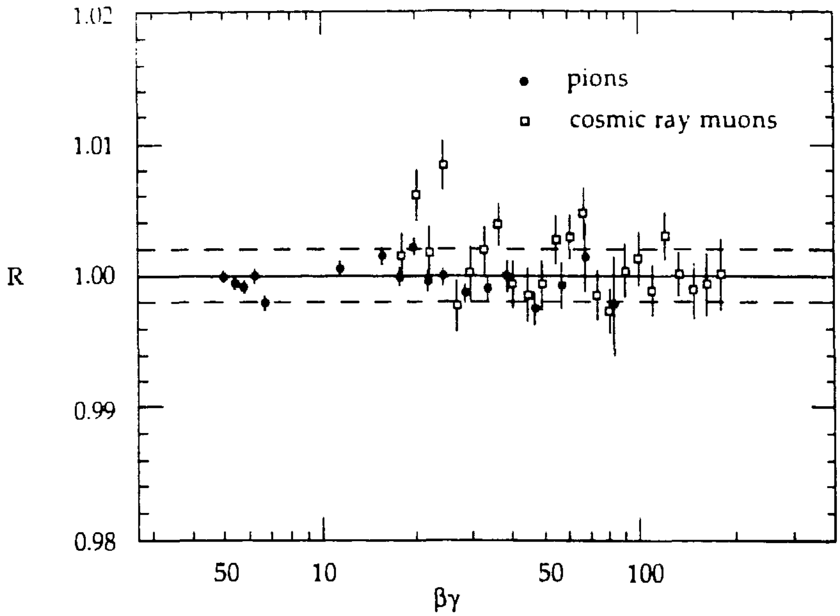

Figure 4.6 The measured truncated mean dE/dx divided by the prediction of the parameterized dE/dx model, R, as a function of $\beta\gamma$ for cosmic ray muons and pions from multihadron events. The dashed lines indicate the estimated systematic uncertainty in the model of 0.2% for the relativistic rise region.

indicate the estimated systematic uncertainty for the $\mathrm{d}E/\mathrm{d}x$ versus velocity curve of 0.2%.

4.6 Estimation of the d*E*/d*x* Resolution

In addition to the expected $\mathrm{d}E/\mathrm{d}x$ as a function of velocity, a knowledge of the $\mathrm{d}E/\mathrm{d}x$ resolution is needed. This was determined from a sample of approximately 47,000 minimum ionizing pions from multihadron events. The tracks were required to have at least 80 usable ionization measurements for determination of the truncated mean, and to have a dip angle between -45° and 45°. The relative resolution, $\sigma_{dE/dx}$ / $(\mathrm{d}E/\mathrm{d}x)$, is shown in figure 4.7, in which tracks of all dip angles are combined. The resolution improves slightly for larger dip angles because of the increase in the effective thickness of the gas layer sampled and pedestal restoration problems in the electronics. A parameterization of $\sigma_{dE/dx}$ / $(\mathrm{d}E/\mathrm{d}x)$ is given by

$$\sigma_{dE/dx} / (\mathrm{d}E/\mathrm{d}x) = \sqrt{\frac{a}{n} + b}\;\;(1 + c\,n + d\,|\sin\lambda|) \qquad (4.27)$$

where n is the number of ionization samples used to compute the truncated mean and λ is the dip angle. Determined parameter values are:

$a = 0.168$

$b = 4.62 \times 10^{-4}$

$c = -5.46 \times 10^{-4}$

$d = -0.258$

Figure 4.8 shows a histogram of the difference between measured and predicted $\mathrm{d}E/\mathrm{d}x$, divided by the $\mathrm{d}E/\mathrm{d}x$ resolution for each track, for the

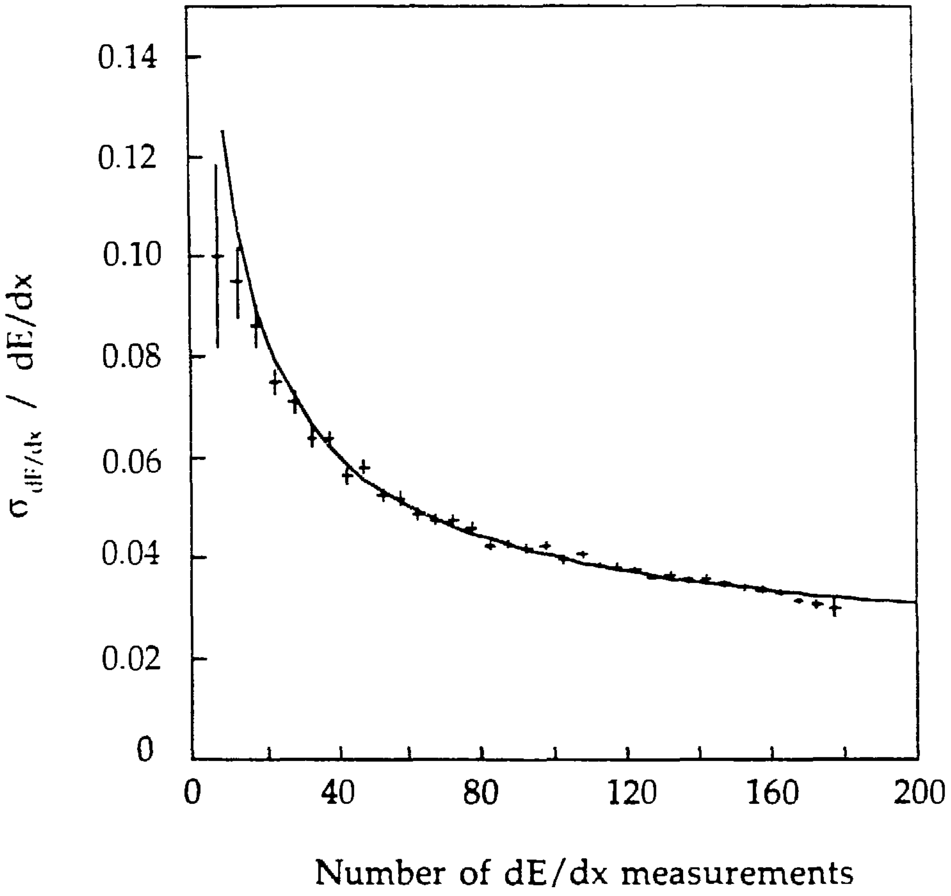

Figure 4.7 The relative dE/dx resolution as a function of the number of wire samples used for determination of the truncated mean.

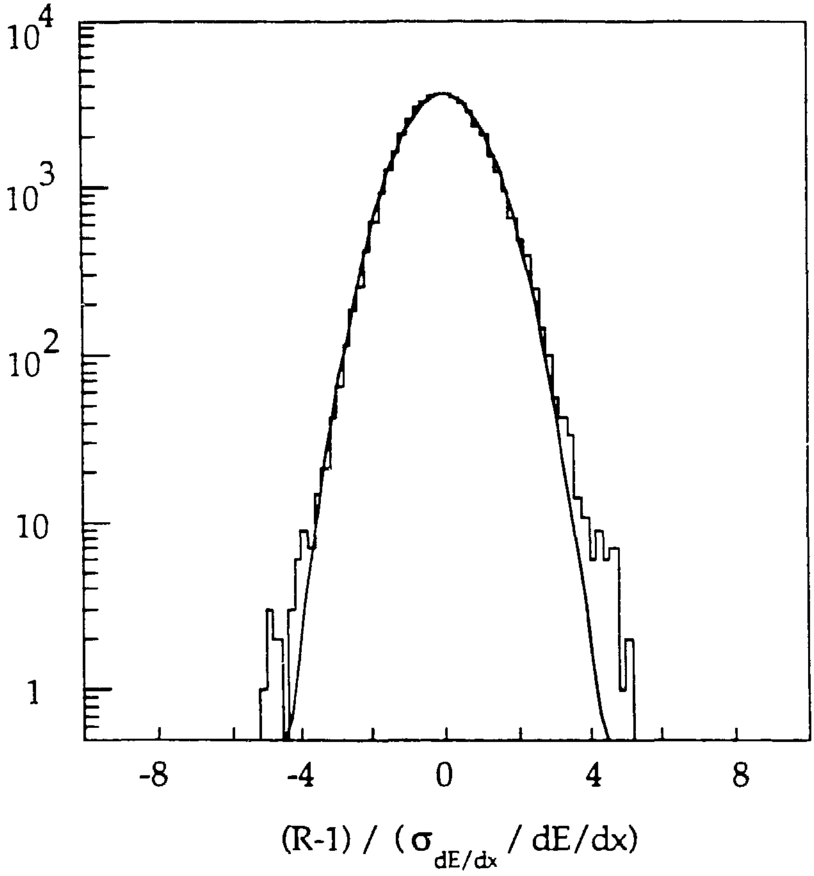

Figure 4.8 Histogram of the quantity $(R - 1) / (\sigma_{dE/dx} / dE/dx)$ for minimum ionizing pions.

minimum ionizing pion sample. The distribution is well described by a Gaussian of unit width out to three standard deviations, demonstrating that the dE/dx response is indeed well understood. Studies with cosmic ray muons indicate that $\sigma_{dE/dx}$ / (dE/dx) remains approximately independent of the mean dE/dx of the track sample for the relativistic rise region. For the $1/\beta^2$ region, the resolution was observed to improve somewhat for track samples of increasing mean dE/dx. (Empirically, $\sigma_{dE/dx}$ / (dE/dx) ~ (dE/dx)$^{-0.35}$.) The relative systematic uncertainty in the dE/dx resolution is estimated to be 8%.

Chapter 5

Event Reconstruction, Selection and Simulation

5.1 Introduction

The basic flow of the analysis used to convert raw input signals into data summary tapes (DSTs -- actually disk files) of multihadron events is shown in figure 5.1. Event selection is carried out at several stages along the way; details are given in reference [52]. The basic philosophy is to analyze the data with the best available calibration constants and correction factors, use the analyzed data to refine the calibrations and corrections, and then reanalyze the data. Only the charged particle analysis for TPC information will be described here.

5.2 Online Analysis

The first stage of the analysis chain, known as preanalysis, is an online event filter for fast rejection of spurious events, mostly beam gas collisions and cosmic rays [53]. Qualitatively, the cuts imposed in preanalysis are similar to (although tighter than) those required by the hardware trigger. Events satisfying charged particle triggers are first processed by the "charged

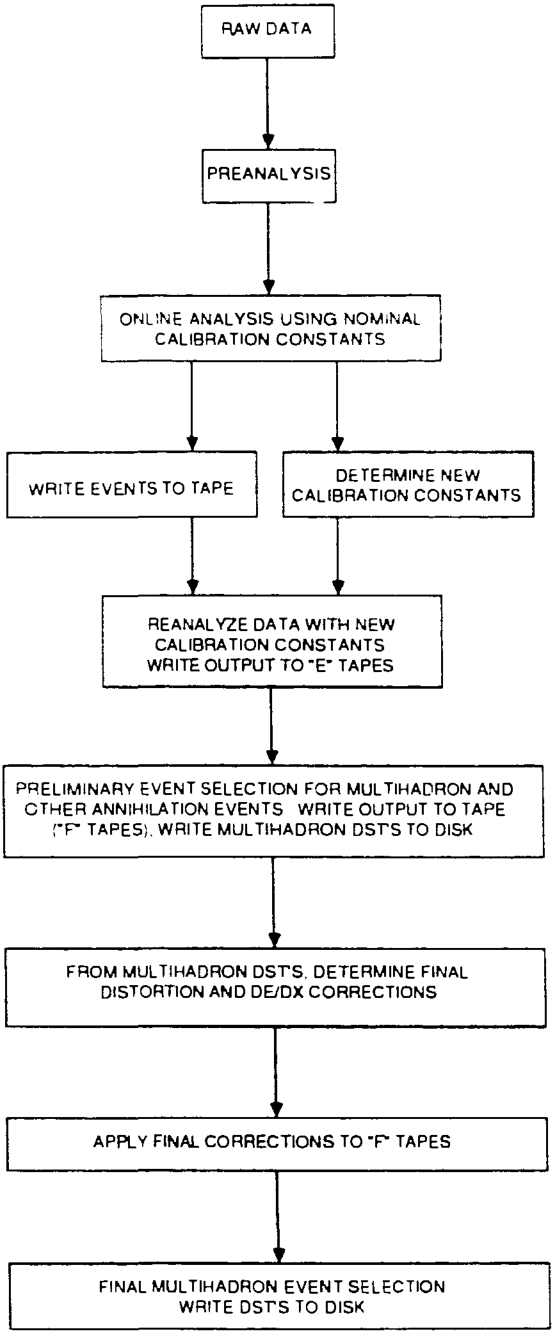

Figure 5.1 The data analysis chain for multihadron events.

preanalysis". Recall that the charged particle trigger uses TPC wire signals and information from the inner and outer drift chambers to identify at least two charged tracks with dip angles less than 60°. In the charged preanalysis, TPC pad information is used to verify that this condition actually existed. If the event is rejected by the charged preanalysis but a neutral trigger was satisfied, the event is processed by the "neutral preanalysis" for verification that the corresponding trigger requirements were met. All events passing preanalysis are recorded on the raw-data tapes. The fraction of events rejected is typically 35%. Approximately 1,000 raw-data tapes were written during the 1984-1986 running cycle.

For the events passing preanalysis, as much further analysis as possible is done online. Large-angle Bhabha events ($e^+e^- \rightarrow e^+e^-$) and multihadron candidates (4-5% of the events passing preanalysis) are processed through the final (DST) level. As many of the other events as possible (typically about 70%) are processed through track reconstruction and the first level of distortion corrections. The charged track reconstruction and momentum determination can be summarized as follows:

1) Find clusters of wire and pad hits. Determine space points from pad clusters. (Program CLUSTER.)

2) Find tracks from space points. (Program PATTERN.)

3) Associate wire clusters with tracks. (Program HAWIRE.)

4) Use wire information to refine space points. Apply distortion corrections. (Program DISTORT.)

5) Determine the tracks' momenta from independent fits in the bend plane and in z. (Program DISTORT.)

6) Determine truncated mean dE/dx. Assign particle type. (Program DEDX.)

7) Redetermine momenta with helix fit. Extrapolate momenta to origin including energy loss corrections based on particle type assignment. (Program TRAGIC.)

8) Redetermine momenta using the constraint that the tracks come from a common vertex. (Program VERTEX.)

9) Summarize data in "DST" format. (Program MAKEDST.)

The online analysis is done using best guesses for calibration constants and correction factors, usually based on a weighted average of the most recent previous data. The processed data is then used to determine new corrections for offline analysis. Information from the multihadron candidates is used to establish the beam position on a run-by-run basis. Drift velocity correction factors are determined from tracks crossing the midplane, and from the edge of the distribution of hits in z. Minimum-ionizing pions from all of the events (mostly two-photon collisions) are used to determine gain factors for the dE/dx analysis. Because of fluctuations in the methane fraction of the TPC gas, the gain factors are crucial for achieving the dE/dx resolution necessary for particle identification. Gain factors as a function of run number are shown in figure 5.2.

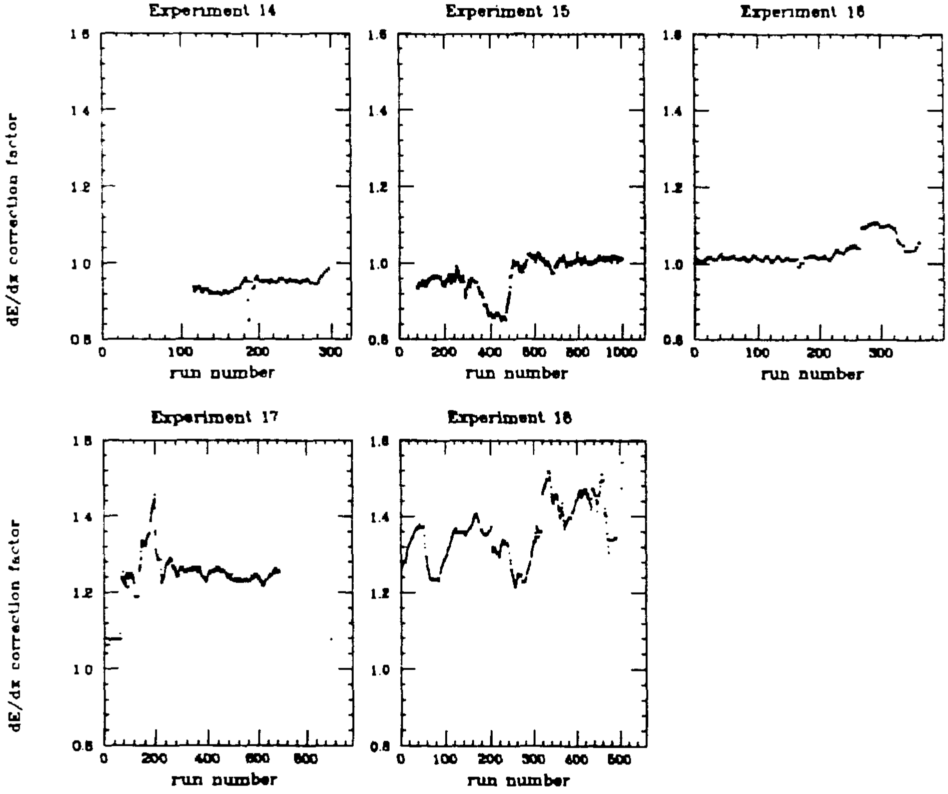

Figure 5.2 Run-by-run dE/dx gain correction factors for the 1984-1986 running cycles. The factors are based on minimum ionizing pions from single-photon annihilation and two-photon multihadronic events.

5.3 Offline Analysis

Once the events have been recorded, the raw data tapes are transported to LBL for further analysis using the refined calibration constants. For events not processed online, the track and event reconstruction procedure described in the previous section is performed up to creating the DST information. For events which have already been processed, the analysis chain is started at the point where the wire information is used to refine the space points and distortion corrections are applied (step 4 above, program DISTORT). Cosmic ray events identified by information from the TPC and the muon chambers are removed. Low-angle Bhabha events are counted for determination of the integrated luminosity, and every tenth event is kept. The output events are written to "E" tapes. The information retained on the "E" tapes includes individual wire pulse heights and space points, but not raw input signals (i.e. digitizer outputs).

DST information is produced from the "E" tapes, and events satisfying loose criteria for $\tau^+\tau^-$, multihadron (i.e. $q\,\bar{q}$) and large angle Bhabha events are output to "F" tapes. There were 193 "F" tapes for 1984-1986. In addition, the DST information for events passing a tighter set of selection criteria for multihadron events is written to disk. For the purposes of the multihadron event selection, a "good" track is defined as satisfying the following criteria:

1) Dip angle, $|\lambda| < 60°$.

2) Curvature error, $\Delta c < 0.3$ (GeV/c)$^{-1}$ or relative curvature error, $\Delta c/c < 0.3$.

3) Momentum in the TPC, $p_{TPC} > 100$ MeV/c.

4) Momentum extrapolated to the interaction point, $p_{VTX} > 120$ MeV/c.

5) Distance of closest approach to the event vertex in the bend plane, $\Delta r < 6$ cm.

6) Distance of closest approach to the event vertex in the direction of the beam, $\Delta z < 10$ cm.

A preliminary mass assignment is made for each track based on its dE/dx and momentum. Pairs of oppositely charged tracks with low invariant mass and dE/dx values consistent with electrons are identified as electron-positron pairs from photon conversions. The total charged energy, E_{ch}, is computed from the measured momenta and the preliminary mass assignments. The sphericity axis is determined, which defines two hemispheres for the event. The following criteria are used to select multihadron events:

1) The number of "good" tracks identified not to be electrons, $N_{had} \geq 5$.

2) Total charged energy, $E_{ch} \geq 7.25$ GeV. (Suppression of two-photon collisions.)

3) Sum of z components of momenta, $\Sigma\ |p_z| < 0.4\ E_{ch}/c$. (Suppression of two-photon collisions and events with large initial state radiation.)

4) The total number of "good" tracks, N_{good}, ≥ half the total number or tracks, $N_{total}/2$.

5) In at least one hemisphere there must be at least 4 non-electron tracks or the invariant mass of the tracks must satisfy $M_{jet} \geq 2.0$ GeV. (Suppression of $\tau^+\tau^-$ background.)

6) The event vertex must be within 2.0 cm of the origin in the x-y plane and 3.5 cm in the z direction.

7) The dip angle of the sphericity axis, $|\lambda_{sph}| \leq 45°$.

This resulted in a sample of 20,126 events.

5.4 Final Corrections to the Data

Once DSTs with multihadron events were available on disk, further analysis was carried out to study systematic effects in the dE/dx measurement. This was based on approximately 47,000 minimum ionizing pions from multihadron events. Correction factors were determined for dependence of the dE/dx on sector, end cap, and dip angle. For example, figure 5.3 shows the uncorrected mean dE/dx for minimum ionizing pions divided by the expected value as a function of dip angle. Variations on the order of several percent can be seen. Correction factors were computed by fitting third order polynomials to the data. The sector-to-sector variations were also on the order of several percent. The dE/dx corrections resulted in an improvement in the dE/dx resolution from 3.7% to 3.5% for pions with at least 120 wire samples for determination of the truncated mean.

In addition, a final set of distortion corrections was developed based on $\mu^+\mu^-$ and Bhabha events. These included corrections for $\mathbf{E} \times \mathbf{B}$ drift based on magnetic field maps obtained with NMR probes [54], and a set of empirical corrections for distortions from sources not entirely understood, but assumed

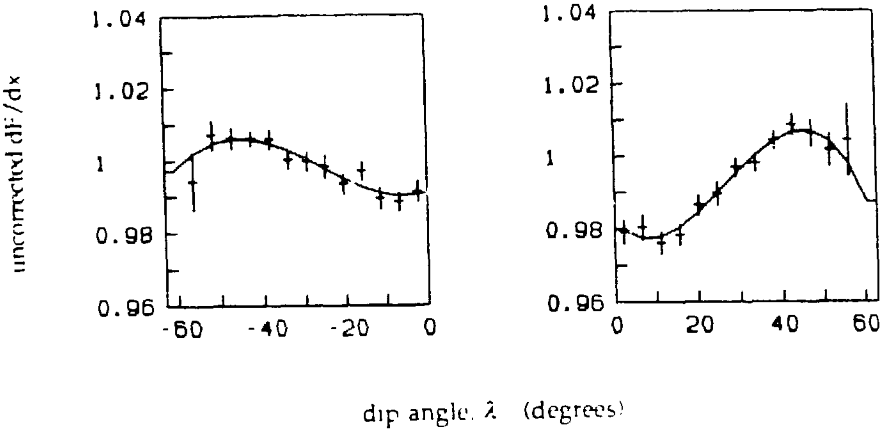

Figure 5.3 The uncorrected dE/dx divided by the expected value as a function of dip angle, λ, for minimum-ionizing pions (data points). Correction factors are determined from the third-degree polynomial fits (curves).

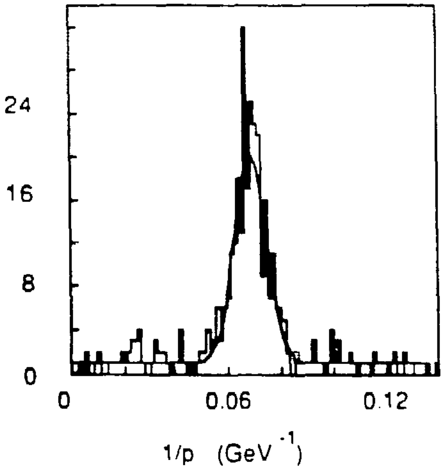

Figure 5.4 Distribution of $1/p$ for muons from $e^+e^- \rightarrow \mu^+\mu^-$ events. The curve is a Gaussian plus constant background fit, giving a momentum resolution of $\Delta p/p = 0.65\% \cdot p$ (GeV/c) for high momentum particles.

to be mainly electrostatic in origin. The result of these corrections was to improve the momentum resolution for high momentum tracks from approximately $\Delta p/p = 0.9\% \cdot p$ (GeV/c) to $0.65\% \cdot p$ (GeV/c). The resolution is determined from the width of the curvature distribution for muons from $\mu^+\mu^-$ events, as shown in figure 5.4. The constant background is from cosmic ray muons which pass through the interaction point.

5.5 Event Simulation

A Monte Carlo event generator and detector simulation program is used to determine the event selection efficiency and particle acceptances, estimate backgrounds and test various data analysis procedures. To simulate multihadron events, the Lund version 5.3 generator was used. (See section 2.4.2 and references [55-57].) The output from this program is basically a list of particles produced in the event, with their types and momenta.

This particle list is the input to the program TPCLUND which simulates the detector response. The philosophy behind TPCLUND is to adequately simulate the overall characteristics of the detector, while running sufficiently quickly to allow a number of events comparable to the amount of actual data to be processed in a short period of time. The time required to process a typical multihadron event is 1.8 seconds on a VAX 8650 computer.

The speed requirement places constraints on the level of detail in which the detector can be represented. TPCLUND describes the detector as a series of hexagonal layers, each characterized by a certain number of radiation lengths, nuclear interaction lengths, and a certain ionization rate for a minimum ionizing particle. The simulation of the particle's evolution from layer to layer includes the effects of decays, nuclear interactions and hard electromagnetic processes (i.e. bremsstrahlung for charged particles, pair production for photons) multiple Coulomb scattering and ionization energy loss. Particles from decays and particles produced in interactions in the detector's material are treated in the same manner.

Rather than simulating the production of ionization in the TPC and its subsequent drift and detection by the sectors, TPCLUND generates space points corresponding to the places where a particle's trajectory crosses a pad row. The positions of the points are then smeared according to the measured position resolution of the detector as a function of drift distance, (i.e. z) crossing angle, α, and pad row. Points are thrown away in regions where tracks overlap. A significant amount of time is saved by not using the pattern recognition program used for the actual data. Instead, points are associated with a track if they are within 3 cm of its trajectory. Ambiguous points are associated with only one track. Tracks with at least three points are said to be found, and the momentum is determined by a fit to a helix.

Individual wire signals are not simulated by TPCLUND. Instead, a truncated mean dE/dx is generated based on the particle's momentum and particle type. The number of usable dE/dx measurements that the track would have had is then estimated. This takes into account how many wires were crossed, track overlap, effects of delta rays and electronics saturation. The dE/dx resolution is then estimated from the number of usable dE/dx measurements and the dip angle using equation 4.27. The initial truncated mean dE/dx value is then smeared with a Gaussian distribution of this width.

From this point, the analysis in TPCLUND mimics the analysis for the real data. A particle type is assigned based on the momentum and dE/dx.

The energy loss in the material between the detector and the interaction point is then estimated. The particle's trajectory is extrapolated to the interaction point including the effects of energy loss. The momentum is then redetermined using the vertex constraint. The output is recorded in the same format as for the real data, so that the same analysis programs can be used for both.

5.6 Backgrounds in the Multihadron Event Sample

The reactions $e^+e^- \rightarrow e^+e^-$ + hadrons (two-photon reactions) $e^+e^- \rightarrow \tau^+\tau^-$ and $e^+e^- \rightarrow e^+e^-$ events were studied as potential sources of background to the multihadron event sample. Background subtractions for the π, K and p momentum spectra are made, although these corrections are in all cases small compared to uncertainties from other sources.

The reaction $e^+e^- \rightarrow e^+e^-$ + hadrons can be viewed as a collision of two photons [58]. For the case where one or both of the Q^2 values of the colliding photons are large compared to vector meson masses (O(1 GeV)), the process can be described by the Quark Partor Model (QPM). A Monte Carlo study was carried out in which 61,504 QPM events were generated and processed through the detector simulation program TPCLUND. The total center-of-mass energy of the two-photon system, $W_{\gamma\gamma}$, was required to be greater than 3 GeV, corresponding to a cross section of 0.42 nb. Of the generated events, 224 were accepted by the selection criteria discussed in section 5.3, from which the fraction of QPM events in the multihadron event sample is estimated to be 0.5%. The error in this value could be quite large (a factor of 2-3) in view of the experimentally observed excess of two-photon events over the QPM prediction [59]. Nevertheless, the QPM background is sufficiently small that it does not constitute a significant source of systematic uncertainty in the analysis of annihilation (i.e. $q\bar{q}$) events. The relative background levels for the various particle species (with statistical errors only) are shown as a function of $z = p \, / \, p_{beam}$ in figure 5.3.

For the case in which the photons' Q^2 values are small or of the same order as vector meson masses, the process $e^+e^- \rightarrow e^+e^-$ + hadrons can be described by the Vector Dominance Model (VDM). Requiring $W_{\gamma\gamma} \geq 3$ GeV as before, the cross section for this process is approximately 2.4 nb. Events of this type tend to produce hadrons at very small angles with respect to the beam direction, so that the amount of detected energy is typically below the minimum energy cut of 7.25 GeV. In a Monte Carlo study with 80,000 generated VDM events, four passed the the multihadron selection cuts with the exception of the 45° cut on the dip angle of the sphericity axis. Of the four, only one passed this final cut, corresponding to a contamination of only 0.01% in the multihadron event sample.

For the reaction $e^+e^- \rightarrow \tau^+\tau^-$, 100,000 events were generated and processed through the detector simulation program. The total cross section including radiative corrections is 0.136 nb. 975 events were accepted, corresponding to a contamination of 0.4%. The background levels as a function of z are shown in figure 5.6. The background peaks at high momentum, reaching 4% for pions in the interval $0.7 < z < 0.9$.

Bhabha events were studied as a potential background to the high momentum region. 200,000 events were generated of the type $e^+e^- \rightarrow e^+e^-$ and $e^+e^- \rightarrow e^+e^-\gamma$, where the minimum scattering angle with respect to the beam direction was 30° and the minimum photon energy in the radiative events

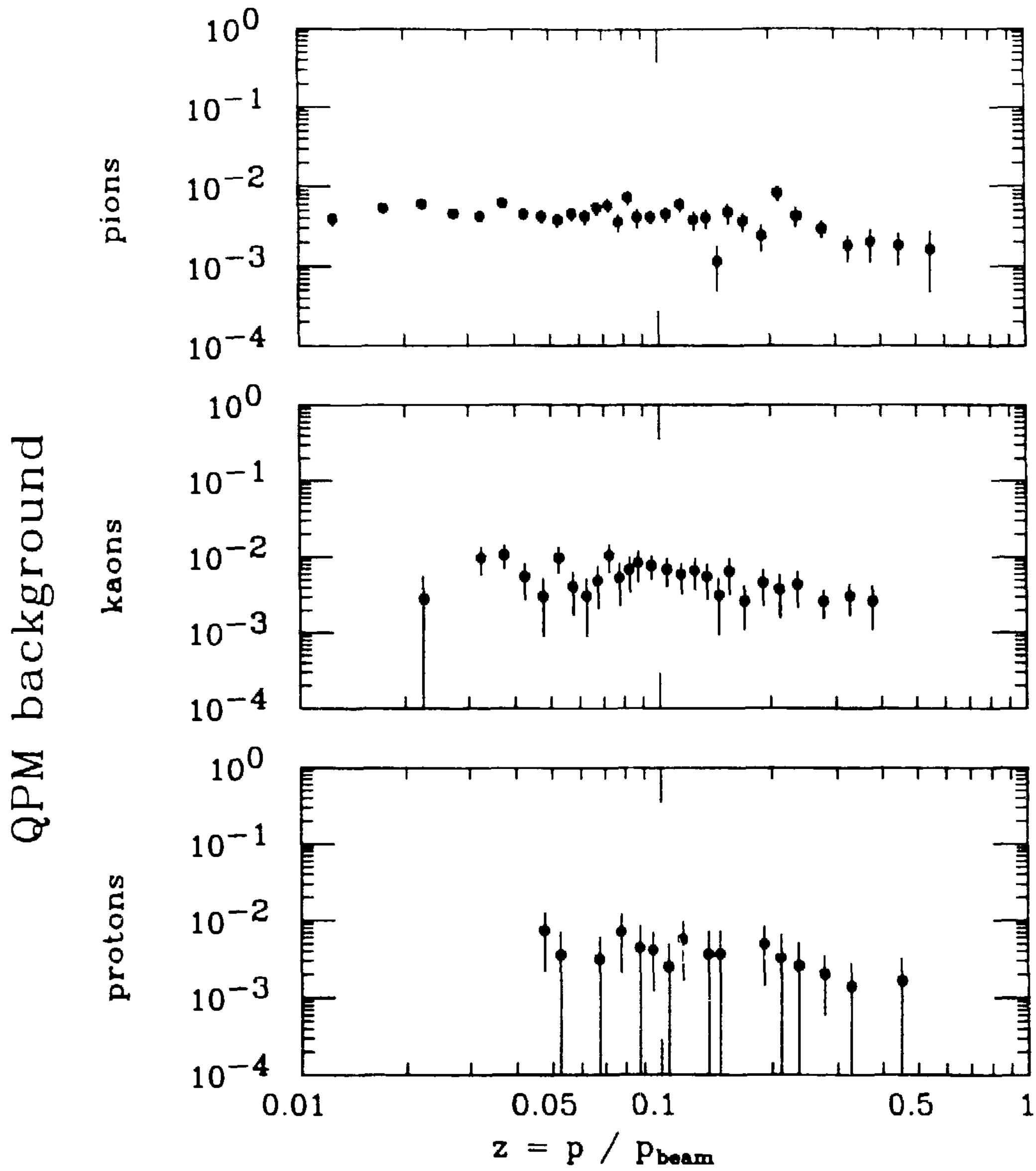

Figure 5.5 Relative background levels in the multihadron event sample from two-photon events based on the quark-parton model as a function of $z = p_{hadron}/p_{beam}$.

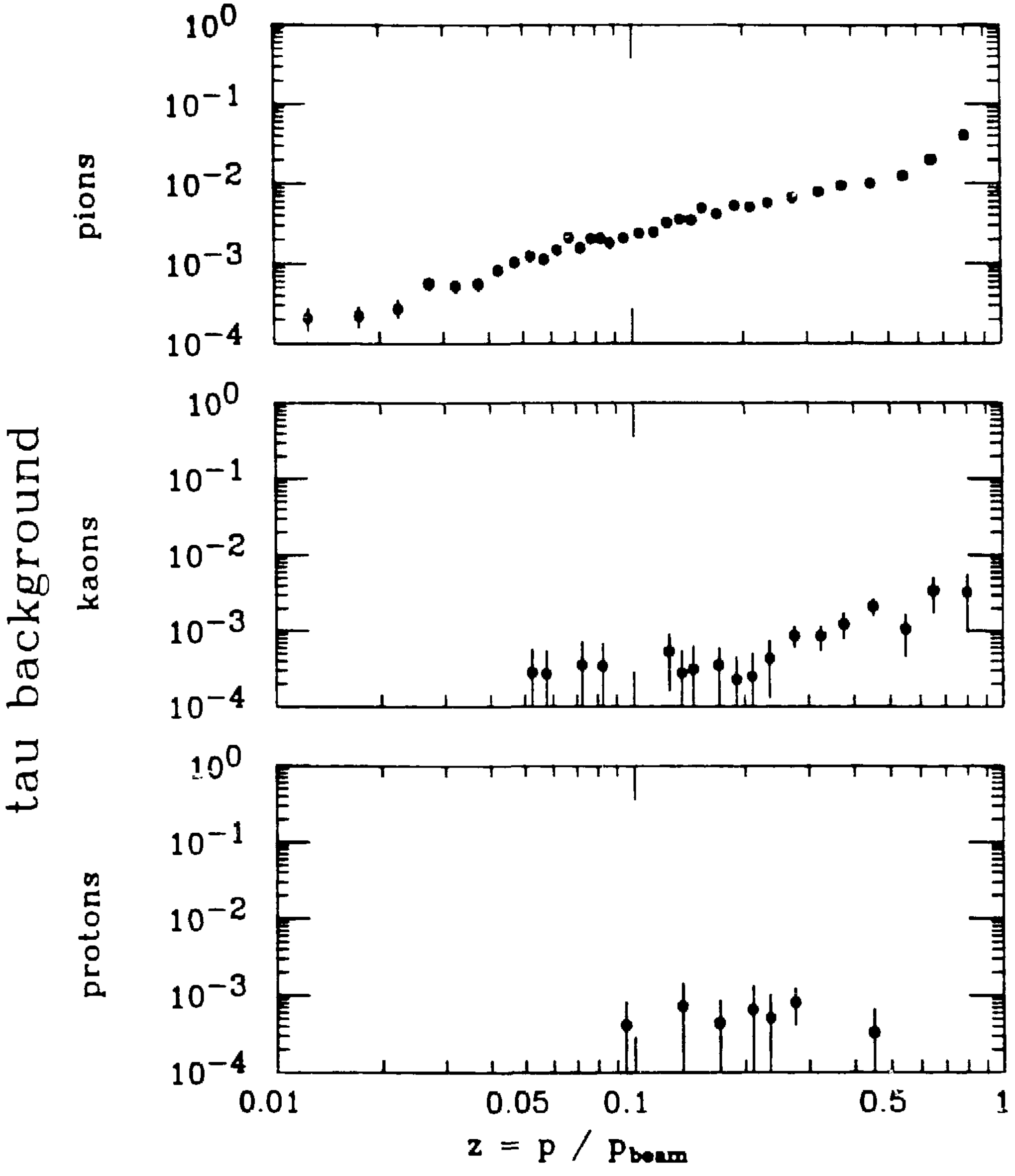

Figure 5.6 Relative background levels in the multihadron event sample from $e^+e^- \rightarrow \tau^+\tau^-$ events as a function of $z = p_{hadron}/p_{beam}$

was 0.5 GeV. The corresponding cross section is 3.64 nb. Approximately 1% of the events contained at least five charged tracks due to electromagnetic processes in the 15% r.l. of material between the interaction point and the detector. The multihadron event selection requires, however, that these tracks be identified not to be electrons. None of the events satisfied this criterion, leading to a 68% confidence level upper limit on the fraction of Bhabha events in the multihadron sample of 0.01%.

Chapter 6

Determination of the Inclusive Cross Sections and Fractions

6.1 Objectives

The 20,126 events passing the multihadron event selection criteria were analyzed to determine the charged hadron inclusive cross sections and fractions. Specifically, the following quantities were measured:

1) $\frac{1}{\sigma_{tot}} \frac{d\sigma}{dz} (e^+e^- \to h + X)$ as a function of $z = p_{hadron}/p_{beam}$ for $h = \pi^\pm$, $K^\pm$, p, $\bar{p}$ and total.

2) $\frac{1}{\sigma_{tot}\,\beta} \frac{d\sigma}{dx} (e^+e^- \to h + X)$ as a function of $x = E_{hadron}/E_{beam}$ for $h = \pi^\pm$, $K^\pm$ and p, $\bar{p}$.

3) $\frac{z}{\sigma_{tot}} \frac{d\sigma}{dz} (e^+e^- \to h + X)$ as a function of $z = p_{hadron}/p_{beam}$ for $h = \pi^\pm$, $K^\pm$ and p, $\bar{p}$.

4) Charged hadron fractions as a function of $z = p_{hadron}/p_{beam}$.

5) K/π, p/π and baryon/meson ratios as a function of $z = p_{hadron}/p_{beam}$.

Here σ_{tot} refers to the total cross section for the process $e^+e^- \rightarrow$ hadrons. The quantities listed above are clearly not independent; all are computed for the sake of convenience in comparison with theory and with other experiments. The fractions and particle ratios have the advantage that a number of systematic uncertainties (e.g. those associated with the acceptance) largely cancel out.

6.2 Track Selection

For determination of the quantities listed above, tracks from the selected events were required to satisfy the following criteria:

1) Number of dE/dx wire samples for determination of the truncated mean dE/dx, $n_w \gtrsim 40$.

2) Absolute value of dip angle, $|\lambda| \leq 60°$.

3) Curvature error of track, $\Delta c \leq 0.15$ GeV^{-1} or relative curvature error, $\Delta c/c \leq 0.15$.

4) Distance of closest approach to event vertex in the x-y plane, $\Delta r \leq$ 3 cm.

5) Distance of closest approach to event vertex in the beam direction, $\Delta z \leq 5$ cm.

At low momenta, a substantial fraction of the observed protons come from nuclear interactions in the material between the interaction point and the TPC. Therefore, only negative particles are used for $z < 0.25$.

6.3 Statistical Fit for the Number of Observed Hadrons

For determination of the hadron fractions and cross sections, the track sample is divided into z (i.e. momentum) intervals as shown in figure 6.1 and table 6.1. Also shown in figure 6.1 is the expected truncated mean dE/dx as a function momentum for electrons, pions, kaons and protons. In the following these curves are referred to as $T_i(p)$, where the index i refers to the particle type. In the relativistic rise region ($z > 0.25$), however, there is only a 1 to 2 standard deviation separation between protons and kaons, and only 2 to 3.5 standard deviations between kaons and pions. As a result, the relative abundances of the various particle types must be determined by a statistical technique.

For purposes of the statistical analysis, it is convenient to normalize the dE/dx of a track by the expected mean dE/dx value for pions at the track's measured momentum:

$$R \equiv \frac{dE}{dx} \Big/ T_\pi(p) . \tag{6.1}$$

The variable $\mu_i(p)$ is defined as the expected mean dE/dx for particle species i divided by the expected mean dE/dx for pions at the momentum p:

$$\mu_i(p) \equiv T_i(p) \ / \ T_\pi(p), \qquad i = \mathrm{e}, \pi, \mathrm{K}, \mathrm{p}. \tag{6.2}$$

For a sample of tracks all of momentum p, particle type i, number of wire samples for truncated mean determination n_w, dip angle λ, and momentum error Δp, the variable R is assumed to follow a Gaussian distribution centered about $\mu_i(p)$ of width

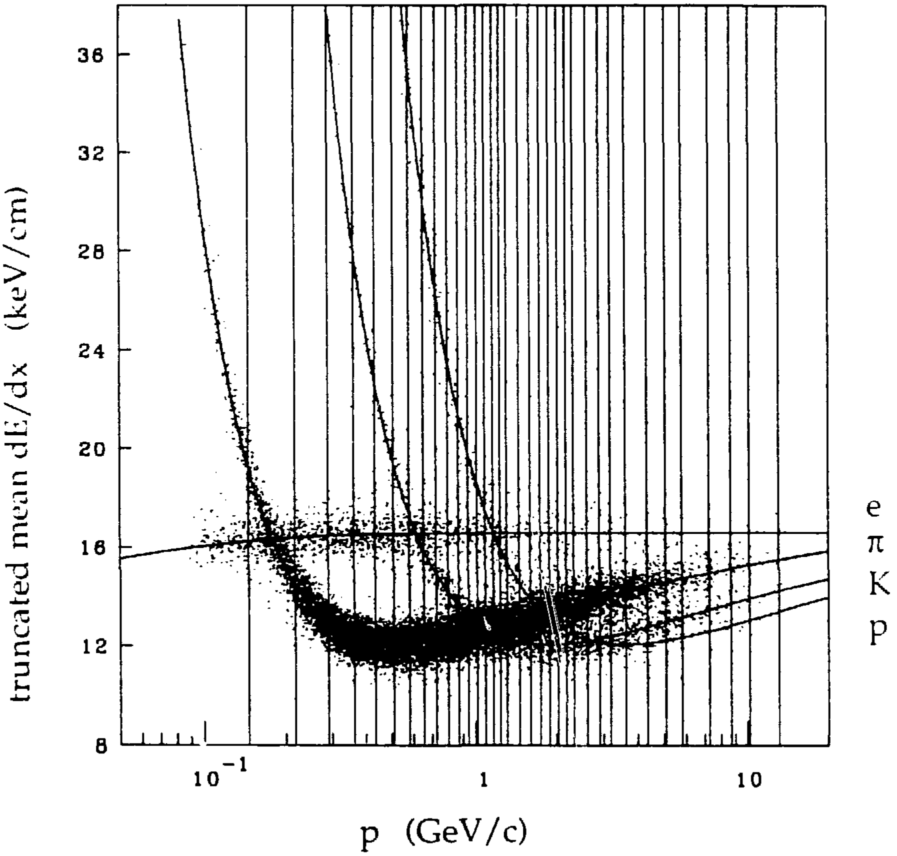

Figure 6.1 Scatter plot of dE/dx versus p showing the momentum intervals used for determination of the inclusive cross sections and fractions.

$$\sigma_i^2 = \left(\sigma_{min\text{-}I\,\pi}(n_w, \lambda)\ \mu_i(p) \left(\frac{(\mathrm{d}E/\mathrm{d}x)_{min\text{-}I}}{T_i(p)} \right)^{\alpha} \right)^2 + \left(\frac{\Delta p}{T_i(p)} \frac{\mathrm{d}}{\mathrm{d}p} T_i(p) \right)^2 . \quad (6.3)$$

Here, $\sigma_{min\text{-}I\,\pi}(n_w, \lambda)$ is the relative $\mathrm{d}E/\mathrm{d}x$ resolution (i.e. $\sigma_{\mathrm{d}E/\mathrm{d}x}/(\mathrm{d}E/\mathrm{d}x)$) as determined from minimum ionizing pions and given by equation 4.27. $(\mathrm{d}E/\mathrm{d}x)_{min\text{-}I}$ is 12.1 keV/cm, the ionization rate for a minimum-ionizing particle. The exponent α is zero for relativistic particles ($\beta > 0.96$) and 0.35 otherwise. (See section 4.6.) The second term corresponds to the broadening due to momentum measurement errors. The contribution from this term is only significant in the $1/\beta^2$ region, since the multiple Coulomb scattering contribution to the momentum resolution is inversely proportional to β.

The tracks within a given momentum interval do not, however, all have the same dip angle, number of $\mathrm{d}E/\mathrm{d}x$ samples, or momentum resolution. Therefore σ_i is different for each track and must be treated as a random variable. Furthermore, the momentum interval is not infinitesimally narrow; it is necessary to consider different values of momentum, and hence different values of $\mu_i(p)$ within the interval. It is assumed that the distribution of the variables R, p and σ_i for tracks within a sufficiently narrow momentum interval are distributed according to

$$F(R, p, \sigma_i) \propto g(p, \sigma_i)\ f(R, p, \sigma_i; \phi_i)\ , \quad (6.4)$$

where the function $f(R, p, \sigma_i; \phi_i)$ is given by

$$f(R, p, \sigma_i; \phi_i) = \sum_i \frac{\phi_i}{\sqrt{2\pi}\,\sigma_i} \exp\left(\frac{-(R - \mu_i(p))^2}{2\sigma_i^2} \right). \quad (6.5)$$

The index i is summed over the four particle types: e, π, K and p. The four adjustable parameters, ϕ_i, are proportional to the abundances of the corresponding particle types. Studies with minimum-ionizing pions indicate that the assumption of a Gaussian distribution is well justified. (See figure 4.8.)

The abundance of each particle type is determined by an extended maximum likelihood fit [60]. The likelihood function is given by

$$L = \exp\left(- \sum_i \phi_i \right) \prod_j f\,(R_j,\, p_j,\, \sigma_{ij};\, \phi_i), \tag{6.6}$$

where the index j runs over all tracks in the momentum interval. It is not necessary to include $g\,(p, \sigma_i)$ in the likelihood function, since it does not depend on the adjustable parameters, ϕ_i. The likelihood function is maximized using the program MINUIT [61]. By using the extended maximum likelihood technique (i.e. including the exponential term in front of the usual product in equation 6.6) the parameters, ϕ_i, give the actual number of particles (not the fraction) of each type. The fit does not require binning in the variable R (i.e. dE/dx) and makes maximal use of the information available for each track. This is particularly important in the high momentum region, where limited statistics are available.

In order to see qualitatively the results of the fit, a histogram of R can be compared to $f\,(R, \langle p \rangle, \langle \sigma_i \rangle; \phi_i)$. Plots for several momentum intervals are shown in figures 6.2a - 6.2d. The function f is evaluated at the mean values of momentum and σ_i in the interval, and its area is scaled to that of the histogram. Note that the relative number of hadrons can be determined even when the peaks are quite close together. This relies heavily on the fact

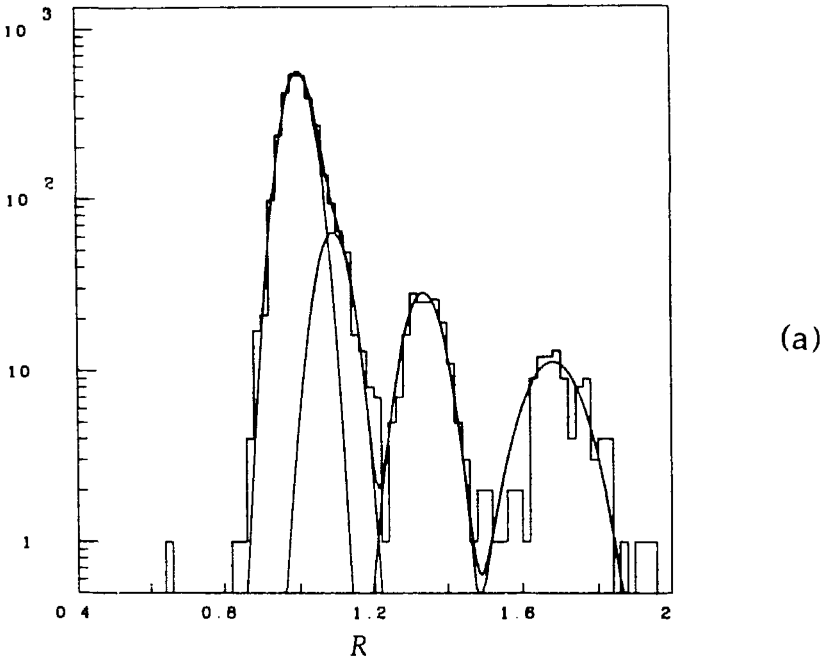

0.060 < z < 0.065

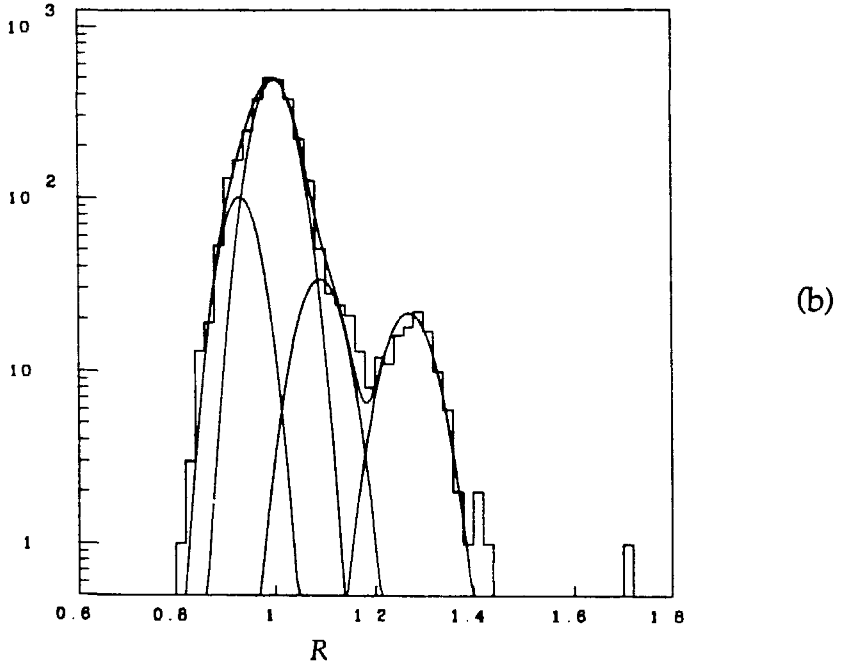

0.100 < z < 0.110

Figures 6.2a, b Histograms of *R* for the indicated *z* intervals. The solid curves correspond to the fit numbers of electrons, pions, kaons and protons.

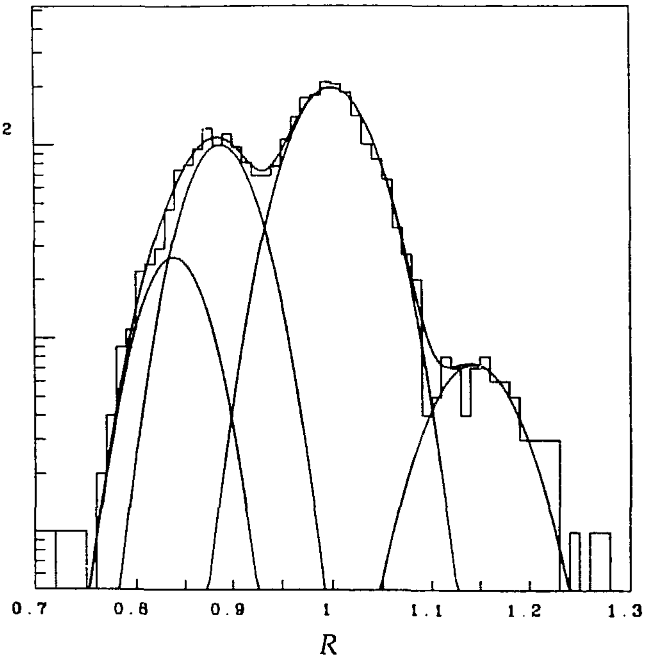

(c)

0.300 < z < 0.350

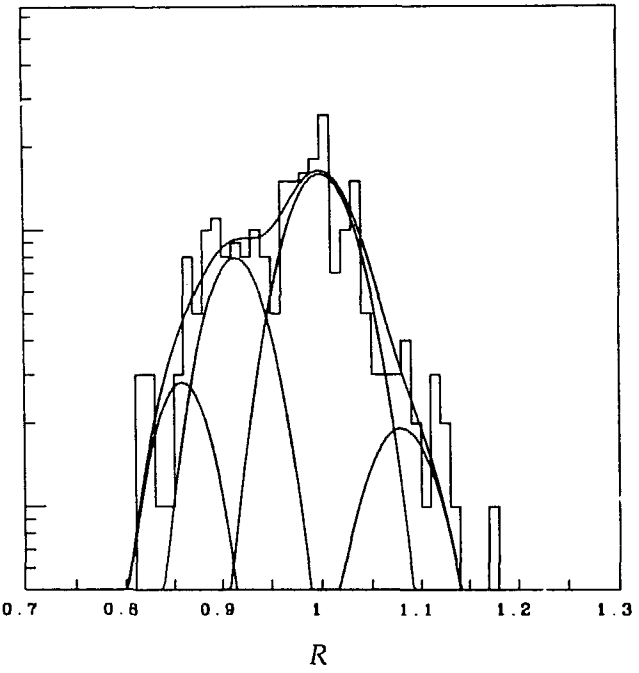

(d)

0.700 < z < 0.900

Figures 6.2c, d Histograms of R for the indicated z intervals. The solid curves correspond to the fit numbers of electrons, pions, kaons and protons.

that the positions of the peaks (i.e. $\mu_i(p)$) and the widths, σ_i, are not adjustable parameters, but instead are determined from separate measurements. Contributions of the uncertainties in these quantities to systematic errors in the cross sections and fractions are discussed in section 6.5.

The fit number of particles in each momentum interval is corrected for background from the processes $e^+e^- \rightarrow \tau^+\tau^-$ and $e^+e^- \rightarrow e^+e^-$ + hadrons as discussed in section 5.6. These corrections are small, and the associated uncertainties do not constitute a significant source of systematic error in the cross sections or fractions.

6.4 Acceptance Corrections

Given a certain number of particles observed in the detector, one must estimate how many particles were actually produced in the e^+e^- collision. The ratio of these two quantities (the acceptance) was determined using the Lund version 5.3 Monte Carlo event generator [55-57] and the Monte Carlo detector simulation program TPCLUND, described in section 5.5.

First, 139,497 multihadron events were generated and processed through the detector simulation program. The event generator included initial state radiation (i.e. photon emission) so that the initial partonic system had, on the average, a center of mass energy somewhat less than 29 GeV. Events and tracks were selected using the same cuts as for the real data. 73,793 events passed the selection criteria described in section 5.3, corresponding to an efficiency of ε_{had} = 0.529. By looking at the reconstructed momentum, z_{TPC}, and the generated particle type of each track, the number of pions, kaons and protons in a given z_{TPC} interval passing the track selection cuts per accepted event was determined.

A second set of 500,000 Monte Carlo events was generated using the same event generator, except that the effects of initial state radiation were turned off. The total number of particles of each type (without any detector simulation or cuts) was recorded as a function of the generated z, z_{MC}. Protons were defined to include the decay products of weakly decaying baryons. Pions included decay products of K^0_S mesons, but not those of K^0_L.

From these two Monte Carlo data sets, the acceptance for particle type i, A_i, is given by

$$A_i = \frac{\begin{pmatrix} \text{Number of particles} \\ \text{of type } i \text{ in } \Delta z_{\mathrm{TPC}} \text{ passing} \\ \text{track cuts per accepted event} \end{pmatrix}}{\begin{pmatrix} \text{Number of particles of type } i \\ \text{generated in } \Delta z_{\mathrm{MC}} \text{ per event} \\ \text{without initial state radiation} \end{pmatrix}} \times \varepsilon_{pattern}. \qquad (6.7)$$

where $\varepsilon_{pattern} = 0.97$ is the estimated pattern recognition for the real data. (The corresponding efficiency in TPCLUND is essentially 100%.) The pion acceptance is computed using the number of pions plus the number of muons passing the track cuts. This corrects for the fact that muons are not separated in the statistical fit. The muon spectrum in the Monte Carlo is in agreement with an independent measurement which utilized the TPC/2γ detector's muon chambers [62]. The acceptance as a function of z for pions, kaons and protons is shown in figure 6.3. The discontinuity corresponds to the requirement that only negative particles be used for $z < 0.25$.

6.5 Error Analysis

The cross sections and ratios listed in section 6.1 are functions of the observed number of hadrons of type i in Δz, n_i, the acceptance, A_i, and the

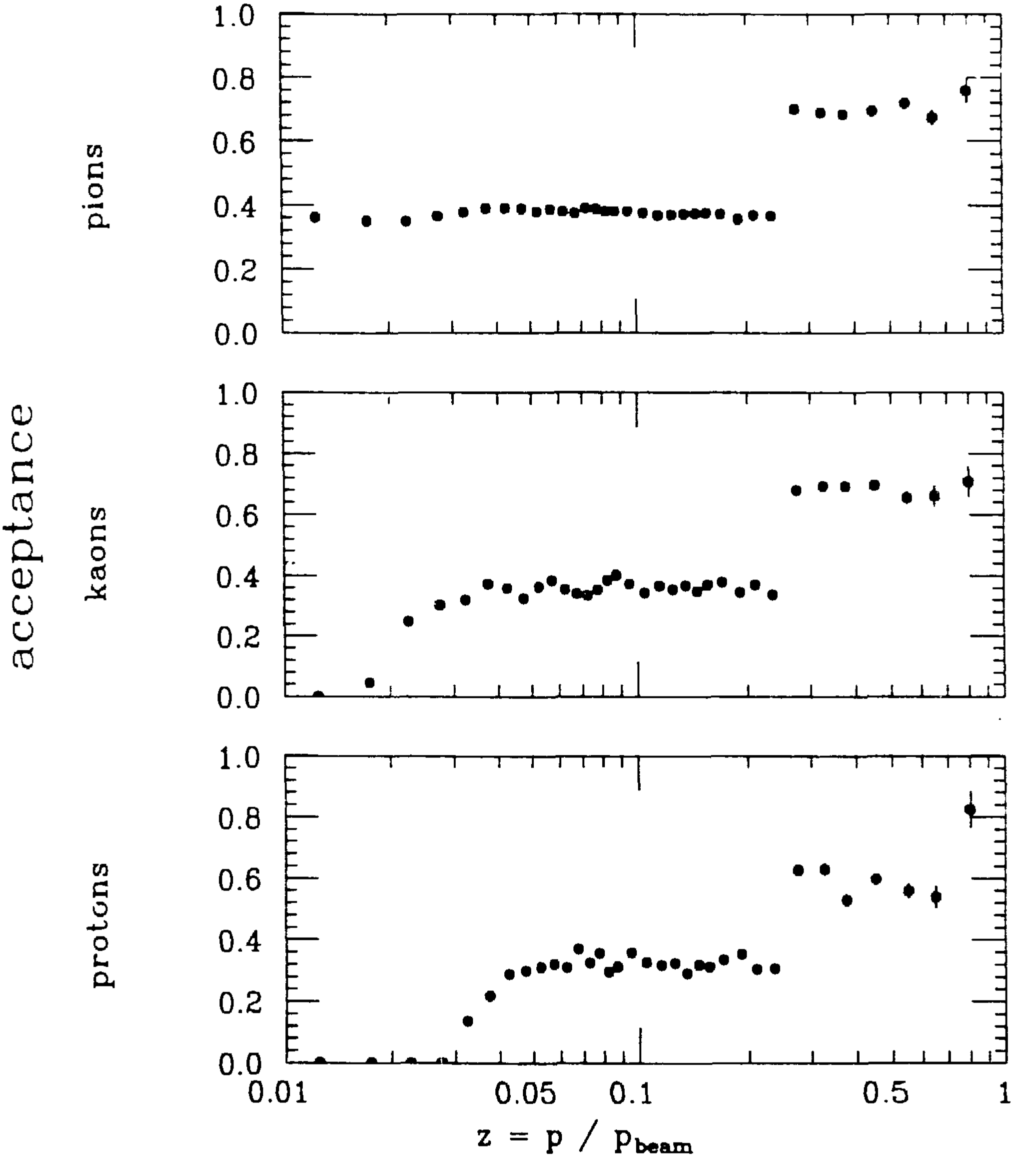

Figure 6.3 Acceptance for charged pions, kaons and protons as a function of $z = p_{hadron}/p_{beam}$. The discontinuity corresponds to the requirement that only negative particles be used for $z < 0.25$.

total number of accepted events, N_{events} = 20,126. For example, the normalized inclusive cross section for hadron type i is computed as

$$\frac{1}{\sigma_{tot}}\frac{d\sigma_i}{dz} = \frac{n_i}{A_i\ \Delta z\ \ N_{events}}. \tag{6.9}$$

The relative error in this quantity is equally sensitive to the relative error in n_i as to that in A_i. The fraction of hadrons of type i is given by

$$f_i = \frac{n_i/A_i}{n_\pi/A_\pi + n_K/A_K + n_p/A_p}. \tag{6.10}$$

Here, the errors due to the acceptance largely cancel, since the errors in A_π, A_K and A_p are highly correlated.

In order to carry out the error propagation for functions of n_i and A_i, a 6×6 covariance matrix, V_{ij}, is defined in which i, j = 1, 2, 3 corresponds to n_π, n_K and n_p, and i = 4, 5, 6 corresponds to A_π, A_K and A_p. The covariance matrix is assumed to be in block diagonal form, with no correlations between the errors in n_i and the errors in A_i. The final covariance matrix is the sum of a number of terms corresponding to both statistical and systematic uncertainties.

For the statistical errors, the part of the covariance matrix corresponding to n_π, n_K and n_p is computed as part of the maximum-likelihood fit. This is done numerically by the program MINUIT using the routine HESSE [61]. Statistical errors in A_π, A_K and A_p are assumed to be uncorrelated, and contribute only to V_{44}, V_{55} and V_{66} respectively.

For n_π, n_K and n_p, the systematic errors are dominated by knowledge of the mean expected dE/dx as a function of momentum, $T_i(p)$, and by knowledge of the dE/dx resolution. The uncertainty in $T_i(p)$ is taken to be $\Delta T/T$ = 0.2% for $i = \pi$, K and p, and 0.4% for i = e. (See figure 4.6.) The contribution to V_{ij} is estimated by repeating the fitting procedure with $T_i(p)$ displaced by $\pm \Delta T_i$ for one of the hadron types:

$$V^{T}_{ij} = \frac{1}{4} \sum_{\alpha} \left(n_i(T_\alpha + \Delta T_\alpha) - n_i(T_\alpha - \Delta T_\alpha)\right) \left(n_j(T_\alpha + \Delta T_\alpha) - n_j(T_\alpha - \Delta T_\alpha)\right) , \tag{6.11}$$

where α is summed over e, π, K and p. The contribution from the uncertainty in the dE/dx resolution is computed in a similar fashion:

$$V^{res}_{ij} = \frac{1}{4} \left(n_i(\sigma + \Delta\sigma) - n_i(\sigma - \Delta\sigma)\right) \left(n_j(\sigma + \Delta\sigma) - n_j(\sigma - \Delta\sigma)\right) , \tag{6.12}$$

where σ is the relative dE/dx resolution for minimum-ionizing pions. $\Delta\sigma/\sigma$ is estimated to be 8%.

For A_π, A_{K} and A_{p}, contributions to the systematic uncertainty are considered from the following sources:

1) Pattern recognition efficiency.

2) Simulation of nuclear interactions.

3) Simulation of the ionization energy loss correction for material between the beam line and the TPC.

4) Effects of momentum smearing.

5) Sensitivity to the cut on the number of dE/dx measurements.

The systematic error in the pattern recognition efficiency should be highly (but not completely) correlated between particle types. (Differences in transverse momentum spectra could, for example, lead to a dependence on particle type.) The contribution to the covariance matrix is taken to be

$$V_{ij}^{pat} = \left((2\%)^2 + (1\%)^2 \, \delta_{ij} \right) A_i \, A_j \ . \tag{6.13}$$

Here (and in the remainder of the discussion of acceptance errors) V_{ij} is understood to refer to the lower-right 3×3 quadrant of the covariance matrix.

The error due to nuclear interactions is broken into three parts: an uncertainty of 10% in the number of nuclear interaction lengths (6.4%) between the beam line and the TPC, a 20% uncertainty in the total interaction cross section, and a 75% uncertainty in production cross sections. In order to estimate the effect of these uncertainties, the contributions to the acceptance for particle type i from particles produced, $A_i^{produced}$, and absorbed, $A_i^{absorbed}$, were estimated from the Monte Carlo. The contributions to the covariance matrix from thickness, particle absorption and production are taken to be

$$V_{ij}^{thickness} = (10\%)^2 \left(A_i^{produced\,2} + A_i^{absorbed\,2} \right)^{1/2} \left(A_j^{produced\,2} + A_j^{absorbed\,2} \right)^{1/2}, \tag{6.14a}$$

$$V_{ij}^{absorption} = (20\%)^2 \, A_i^{absorbed} \, A_j^{absorbed}, \tag{6.14b}$$

$$V_{ij}^{production} = (75\%)^2 \, A_i^{produced} \, A_j^{produced}. \tag{6.14c}$$

The relative uncertainty in the amount of ionization energy loss in the material between the interaction region and the TPC is assumed to be 15%, independent of the amount of energy lost. This leads to the following contribution to the covariance matrix:

$$V_{ij}^{E\ loss} = \Delta\left(\ln E_i^{loss}\right)\,\Delta\left(\ln E_j^{loss}\right)\,\frac{\partial A_i}{\partial \ln E_i^{loss}}\,\frac{\partial A_j}{\partial \ln E_j^{loss}}$$

$$= (15\%)^2\left(\frac{\partial A_i}{\partial p}\,\frac{E_i^{loss}}{\beta_i}\right)\left(\frac{\partial A_j}{\partial p}\,\frac{E_j^{loss}}{\beta_j}\right). \qquad (6.15)$$

The derivatives with respect to momentum are computed by finite differences. The energy loss by particle type i is estimated as the average energy loss of a minimum ionizing particle (10 MeV at $\lambda = 45°$) divided by β_i^2. This source of error is only significant for momenta corresponding to the $1/\beta^2$ regions.

The acceptances could have been determined using the number of particles passing the track cuts in an interval of the generated momentum, Δz_{MC}. The resulting spectra would then need to be unfolded to correct for the effects of momentum smearing. Because of difficulties in carrying out such an unfolding procedure, the acceptances were determined using the momenta as reconstructed by the detector simulation program. (See equation 6.7.) This effectively corrects for momentum smearing, but is only correct if the momentum spectra in the event generator are the same as those of the real world. Based on estimates of such a discrepancy, the contribution to the covariance matrix for $0.7 < z < 0.9$ is taken to be

$$V_{ij}^{p\ smearing} = (10\%)^2\, A_i\, A_j\ . \qquad (6.16)$$

For $z < 0.7$ the momentum smearing error is negligible.

Systematic errors due to track cuts were estimated by varying the selection criteria listed in section 6.2. For the most part, the acceptance corrected results are sufficiently insensitive to the cuts that the corresponding systematic uncertainties can be neglected. The one exception concerns the cut on the number of dE/dx measurements ($n_w \geq 40$). This effects the results for highly ionizing protons, and for pions of sufficiently low momenta that their tracks curl up inside the TPC. The contributions to the covariance matrix are

$$V_{44}^{cuts} = (7\%)^2 \; A_{\pi}^{2} \qquad 0.010 < z < 0.015\,, \tag{6.17a}$$

$$V_{66}^{cuts} = (10\%)^2 \; A_{p}^{2} \qquad 0.035 < z < 0.040\,, \tag{6.17b}$$

$$V_{66}^{cuts} = (5\%)^2 \; A_{p}^{2} \qquad 0.040 < z < 0.045\,. \tag{6.17c}$$

For the cross sections, statistical errors dominate above $x \sim 0.5$. The systematic errors for the proton and kaon cross sections are dominated by the 0.2% uncertainty in the dE/dx vs. velocity curve and the 8% uncertainty in the dE/dx resolution. The pion cross section is dominated by the uncertainty in the pattern recognition efficiency. Because of the correlations in a number of the systematic errors, the uncertainties in the fractions are predominantly statistical over almost the entire momentum range.

6.6 Results

The various cross sections and particle ratios listed in section 6.1 are shown in figures 6.4 through 6.11. Values are given in tables 6.1 through 6.6. One of the cross sections contains factors determined from the Monte Carlo:

$$\frac{1}{\sigma_{tot}\,\beta}\,\frac{\mathrm{d}\sigma_i}{\mathrm{d}x} = \left\langle \frac{1}{\beta_i} \right\rangle \frac{n_i}{A_i \;\Delta x \;\; N_{events}}\,. \tag{6.18}$$

Values of $<1/\beta_i>$ determined from the Lund version 5.3 event generator are given in table 6.3. The factor of z in the cross section $z/\sigma_{tot}\, d\sigma_i/dz$ is taken as the average z for all particle types over the momentum interval:

$$\frac{z}{\sigma_{tot}} \frac{d\sigma_i}{dz} = \frac{<z>\, n_i}{A_i\ \Delta z\ \ N_{events}}. \tag{6.19}$$

All points are plotted in the centers of the corresponding z or x intervals.

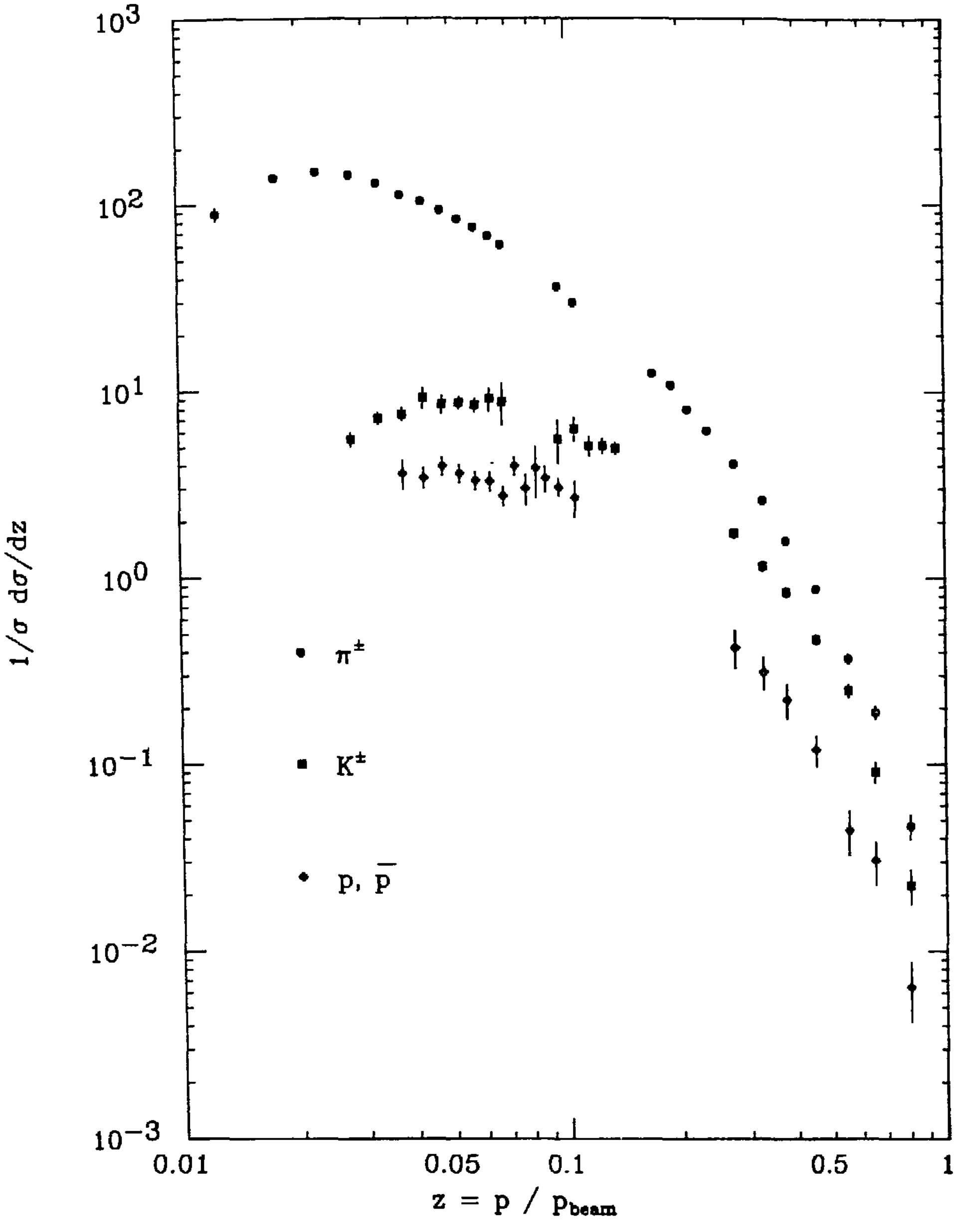

Figure 6.4 The normalized inclusive cross section $1/\sigma_{tot}\ d\sigma_i/dz$ for $i = \pi^\pm$, $K^\pm$ and p, $\bar{p}$ as a function of $z = p_{hadron}/p_{beam}$.

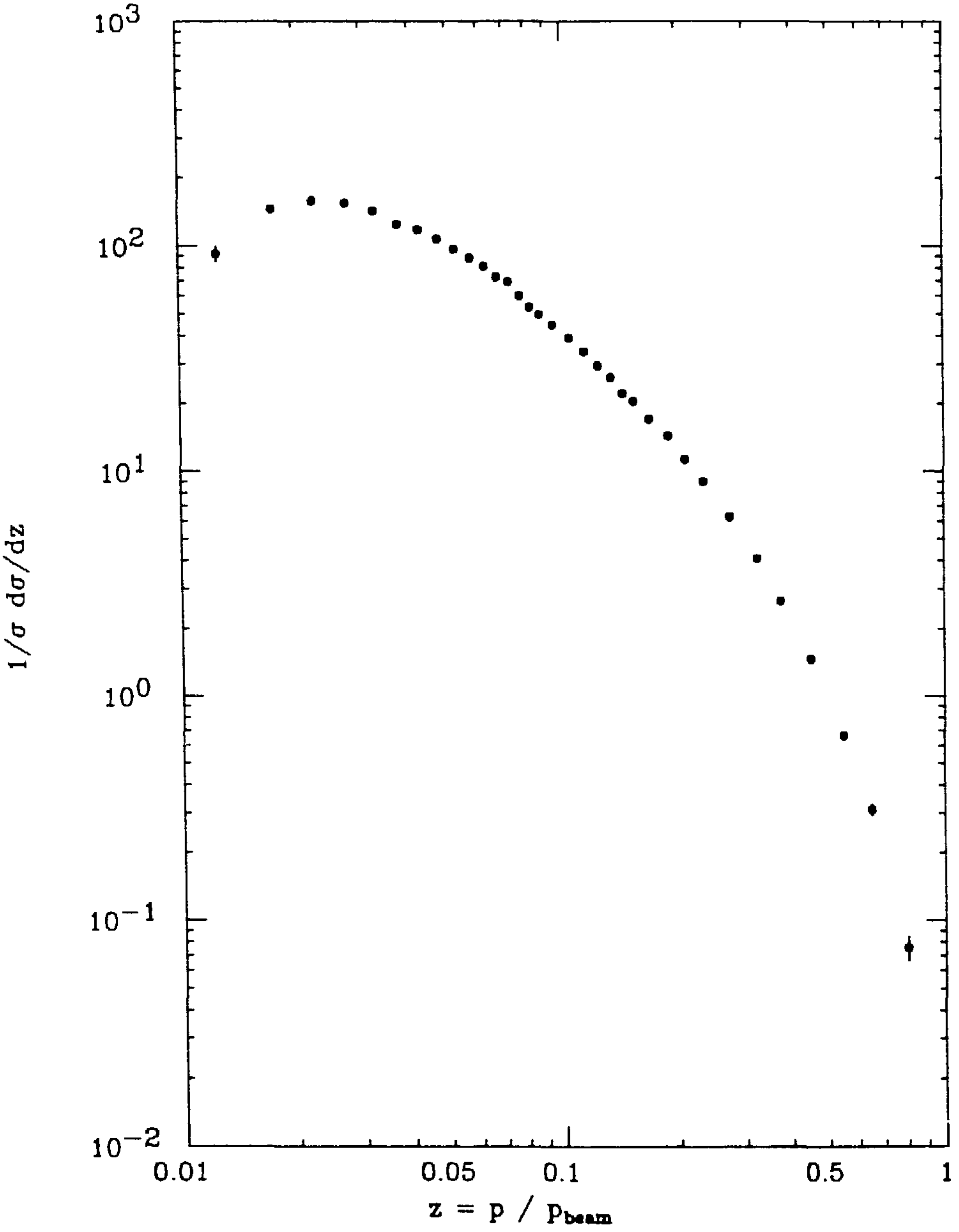

Figure 6.5 The normalized inclusive cross section $1/\sigma_{tot}\, d\sigma/dz$ for charged stable hadrons (i.e. $\pi^{\pm} + K^{\pm} + p, \bar{p}$) as a function of $z = p_{hadron}/p_{beam}$.

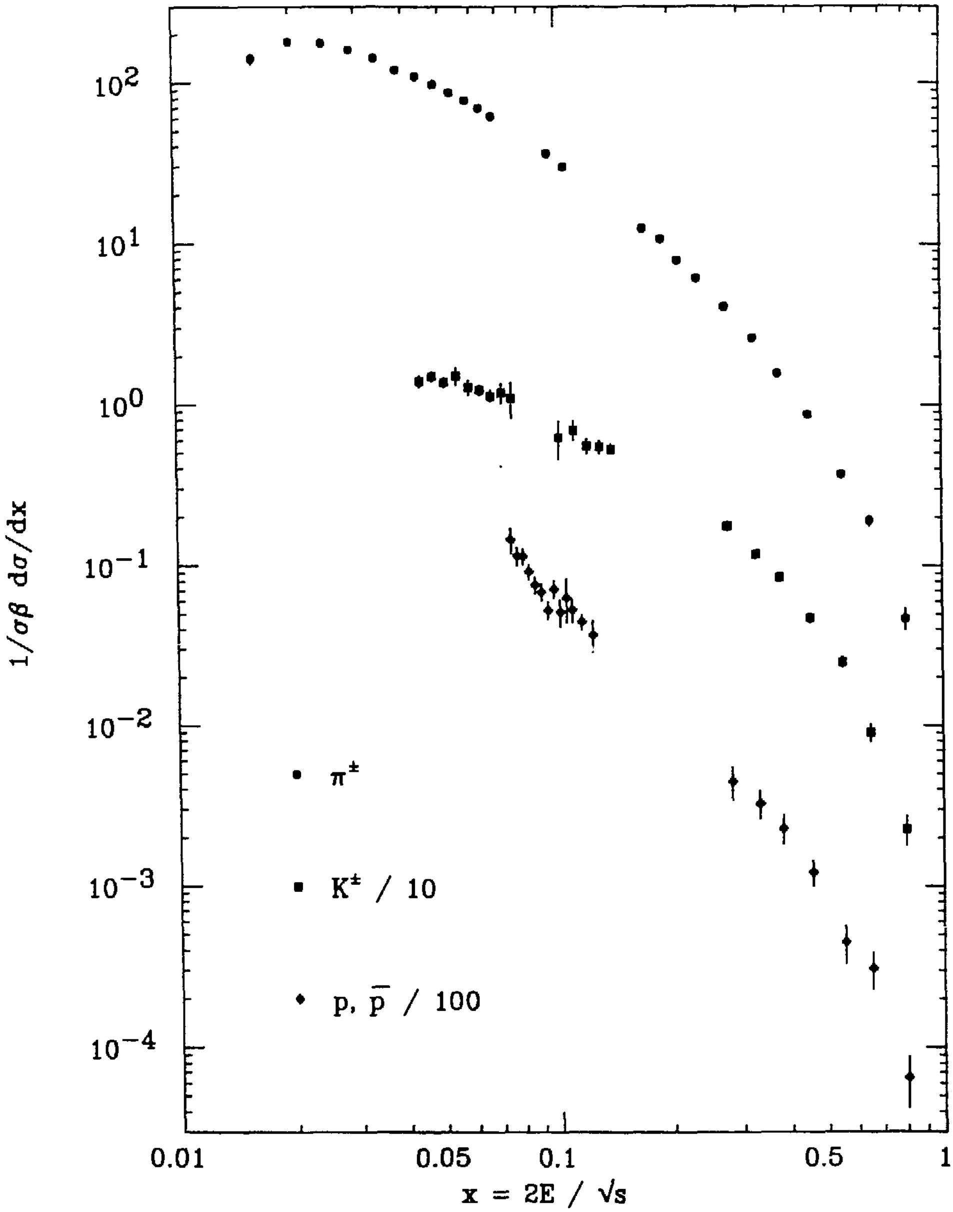

Figure 6.6 The normalized inclusive cross section $1/\beta\sigma_{tot}\ d\sigma_i/dx$ for $i = \pi^\pm$, $K^\pm$ and p, $\bar{p}$ as a function of $x = 2E_{hadron}/\sqrt{s}$.

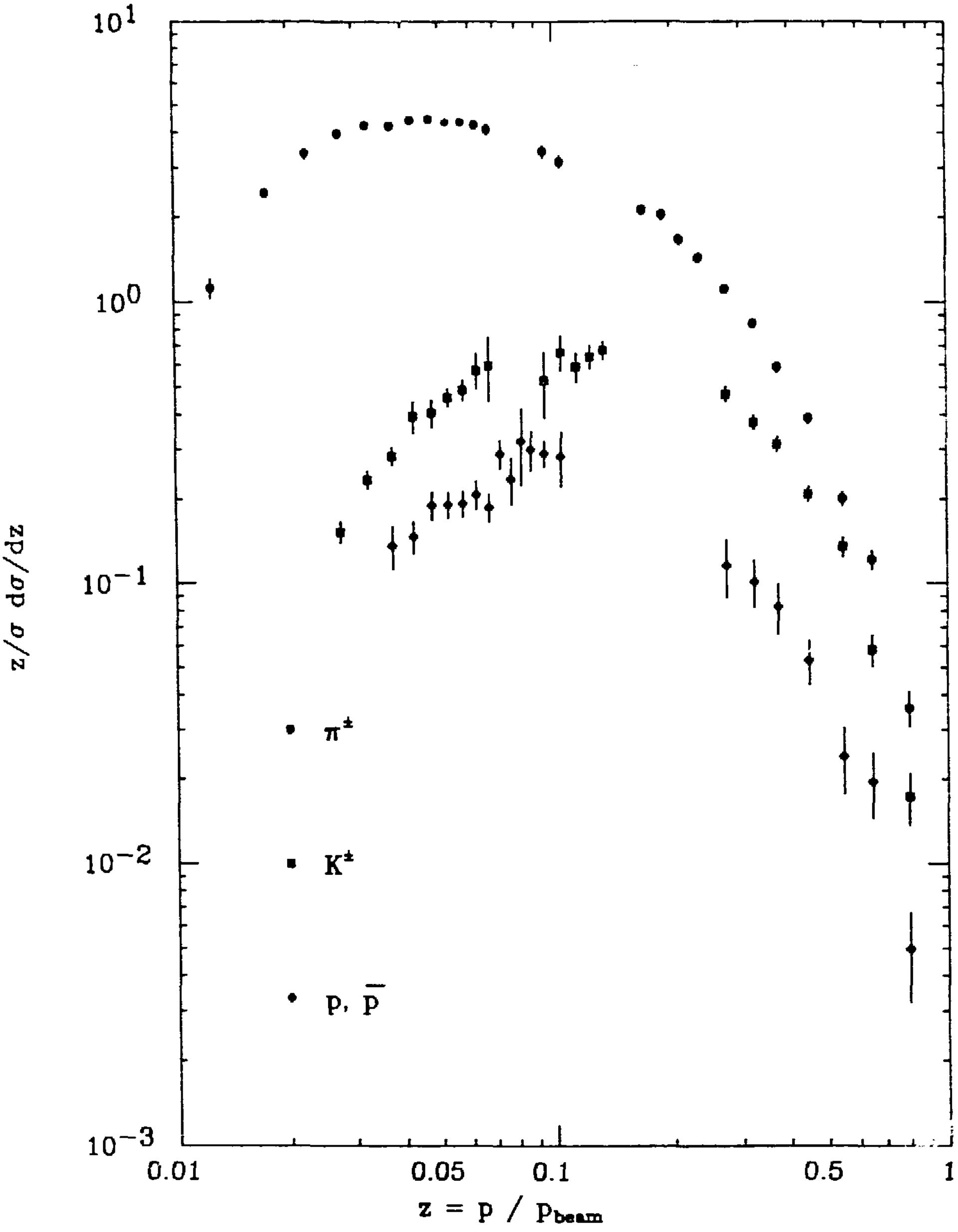

Figure 6.7 The inclusive cross section $z/\sigma_{tot}\, d\sigma_i/dz$ for $i = \pi^\pm$, $K^\pm$ and p, $\bar{p}$ as a function of $z = p_{hadron}/p_{beam}$.

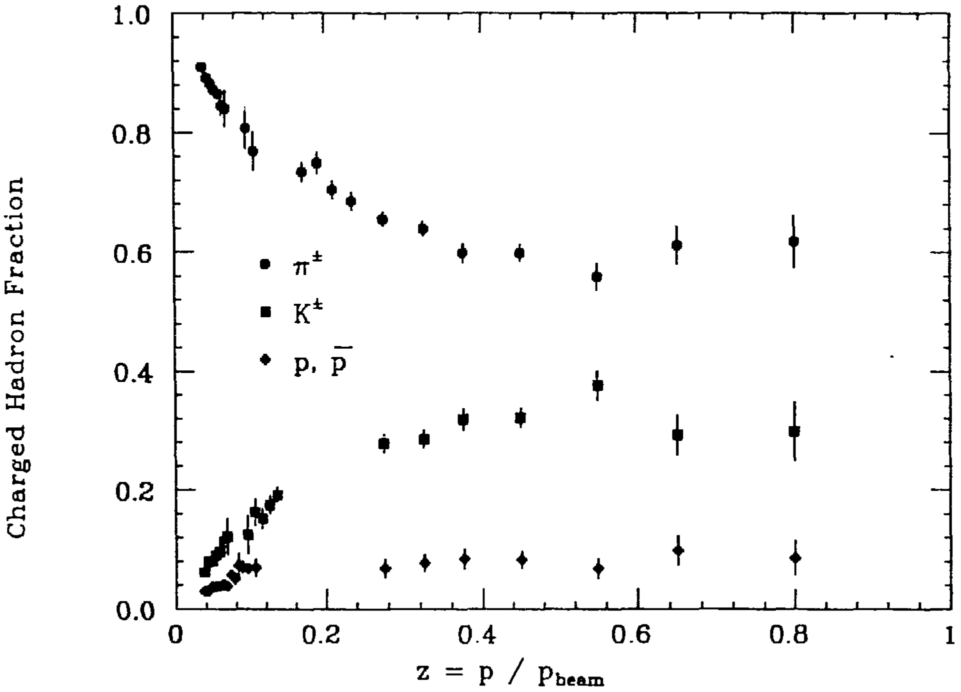

Figure 6.8 The charged hadron fractions as a function of $z = p_{hadron}/p_{beam}$.

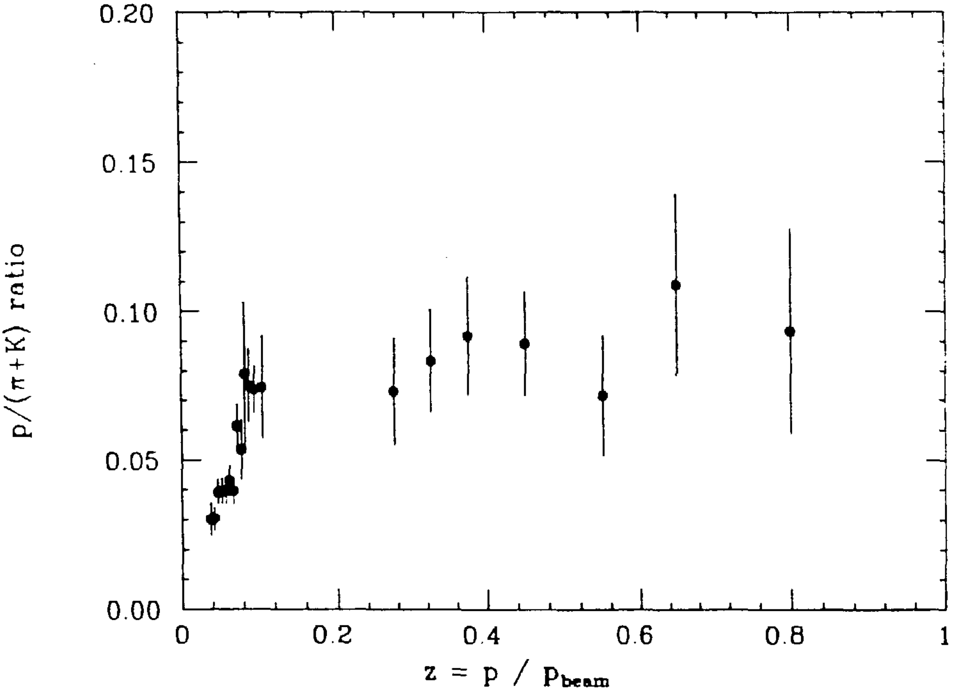

Figure 6.9 The ratio (p, $\bar{p}$) / ($\pi^{\pm}$ + $K^{\pm}$) as a function of $z = p_{hadron}/p_{beam}$

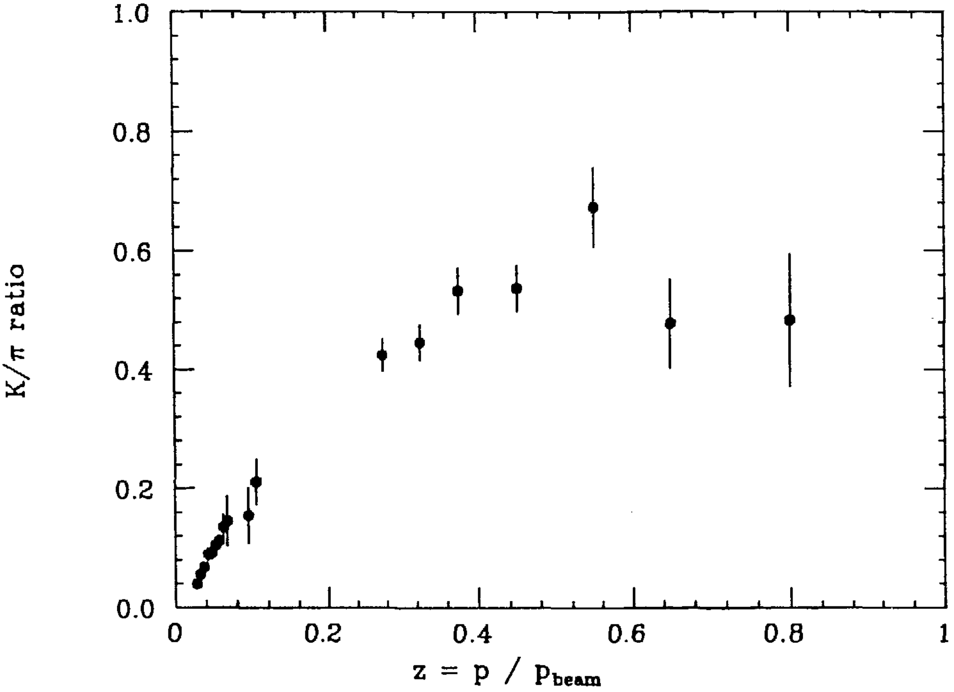

Figure 6.10 The ratio $K^{\pm}/\pi^{\pm}$ as a function of $z = p_{hadron}/p_{beam}$.

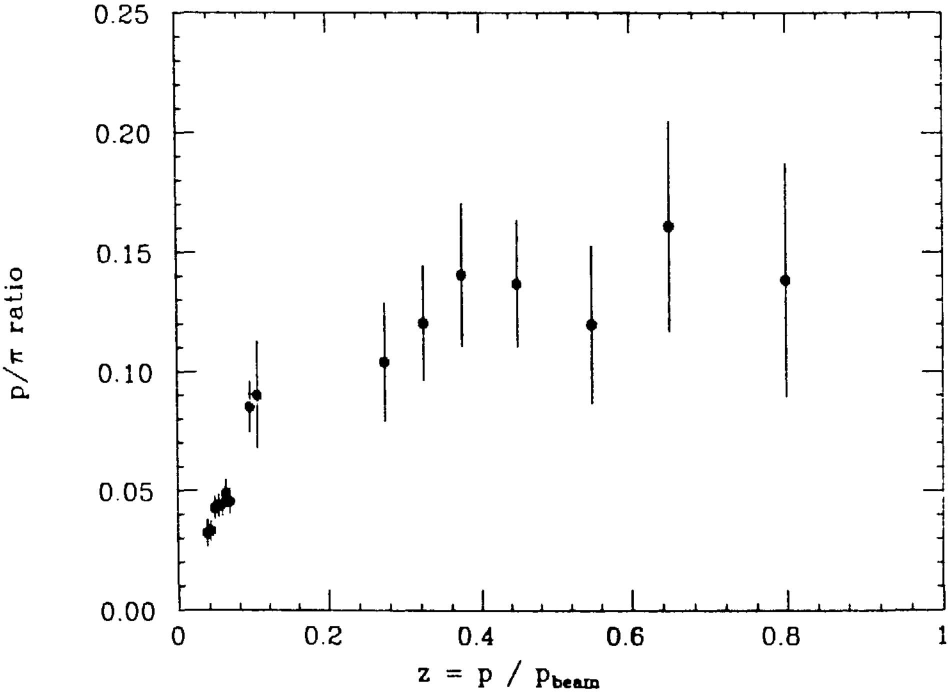

Figure 6.11 The ratio (p,p̄) / $K^{\pm}$ as a function of $z = p_{hadron}/p_{beam}$.

Table 6.1 The normalized cross section $1/\sigma_{tot}\ d\sigma_i/dz$ for $i = \pi^\pm, K^\pm, p, \bar{p}$ and total (i.e. $\pi^\pm + K^\pm + p, \bar{p}$) as a function of $z = p_{hadron}/p_{beam}$.

z interval	$\frac{1}{\sigma_{tot}}\frac{d\sigma}{dz}(e^+e^- \to h^\pm + X)$			
	$\pi^\pm$	$K^\pm$	$p, \bar{p}$	total
0.010 - 0.015	88.4 ± 7.2	-	-	91.5 ± 7.4
0.015 - 0.020	138.3 ± 5.4	-	-	144.8 ± 5.6
0.020 - 0.025	149.5 ± 6.6	-	-	157.7 ± 7.0
0.025 - 0.030	144.2 ± 5.0	5.56 ± 0.49	-	153.4 ± 5.2
0.030 - 0.035	130.9 ± 4.1	7.21 ± 0.56	-	142.2 ± 4.3
0.035 - 0.040	112.9 ± 3.5	7.60 ± 0.59	3.63 ± 0.65	124.1 ± 3.8
0.040 - 0.045	104.6 ± 3.2	9.3 ± 1.2	3.46 ± 0.46	117.3 ± 3.6
0.045 - 0.050	93.8 ± 3.0	8.55 ± 0.96	3.99 ± 0.46	106.4 ± 3.3
0.050 - 0.055	83.8 ± 2.7	8.73 ± 0.65	3.64 ± 0.41	96.2 ± 3.0
0.055 - 0.060	76.0 ± 2.5	8.48 ± 0.74	3.35 ± 0.39	87.8 ± 2.7
0.060 - 0.065	68.2 ± 2.6	9.2 ± 1.3	3.32 ± 0.39	80.7 ± 2.6
0.065 - 0.070	60.9 ± 3.0	8.8 ± 2.3	2.76 ± 0.33	72.5 ± 2.4
0.070 - 0.075	-	-	4.00 ± 0.48	69.2 ± 2.4
0.075 - 0.080	-	-	3.04 ± 0.58	60.0 ± 2.2
0.080 - 0.085	-	-	3.9 ± 1.2	53.3 ± 2.2
0.085 - 0.090	-	-	3.43 ± 0.57	49.2 ± 1.8
0.090 - 0.100	36.0 ± 1.9	5.6 ± 1.5	3.06 ± 0.33	44.6 ± 1.4
0.100 - 0.110	29.9 ± 1.5	6.32 ± 0.92	2.69 ± 0.60	39.0 ± 1.3
0.110 - 0.120	-	5.13 ± 0.61	-	33.9 ± 1.3
0.120 - 0.130	-	5.13 ± 0.49	-	29.4 ± 1.1
0.130 - 0.140	-	5.00 ± 0.38	-	26.1 ± 1.0
0.140 - 0.150	-	-	-	22.11 ± 0.82
0.150 - 0.160	-	-	-	20.44 ± 0.79
0.160 - 0.180	12.48 ± 0.51	-	-	17.00 ± 0.58
0.180 - 0.200	10.77 ± 0.45	-	-	14.38 ± 0.58
0.200 - 0.220	7.95 ± 0.36	-	-	11.31 ± 0.44
0.220 - 0.250	6.13 ± 0.26	-	-	8.96 ± 0.32
0.250 - 0.300	4.09 ± 0.14	1.73 ± 0.11	0.42 ± 0.10	6.24 ± 0.18
0.300 - 0.350	2.61 ± 0.10	1.161 ± 0.073	0.313 ± 0.062	4.08 ± 0.13
0.350 - 0.400	1.581 ± 0.071	0.842 ± 0.055	0.222 ± 0.046	2.644± 0.093
0.400 - 0.500	0.874 ± 0.038	0.470 ± 0.030	0.120 ± 0.022	1.463 ± 0.049
0.500 - 0.600	0.370 ± 0.022	0.249 ± 0.020	0.044 ± 0.012	0.663 ± 0.029
0.600 - 0.700	0.190 ± 0.015	0.090 ± 0.012	0.0305 ± 0.0080	0.310± 0.019
0.700 - 0.900	0.0466 ± 0.0070	0.0225 ± 0.0048	0.0064 ± 0.0023	0.0755 ± 0.0098

Table 6.2 The normalized cross section $1/\sigma_{tot}\beta\ d\sigma/dx$, where $x = 2E_{hadron}/\sqrt{s}$, for fixed intervals of $z = p_{hadron}/p_{beam}$.

z interval	x_{center}	$\frac{1}{\sigma_{tot}\beta}\frac{d\sigma}{dx}\ (e^+e^- \to h^{\pm} + X)$				
		$\pi^{\pm}$		$K^{\pm}$		$p,\bar{p}$
0.010 - 0.015	0.016	142. ± 12.		-		-
0.015 - 0.020	0.020	180.9 ± 7. 1		-		-
0.020 - 0.025	0.024	177.2 ± 7.8		-		-
0.025 - 0.030	0.029	162.1 ± 5.6	0.044	14.1 ± 1.2		-
0.030 - 0.035	0.034	142.5 ± 4.5	0.047	15.2 ± 1.2		-
0.035 - 0.040	0.039	120.4 ± 3.7	0.051	13.9 ± 1.1	0.075	14.5 ± 2.6
0.040 - 0.045	0.044	110.0 ± 3.4	0.054	15.2 ± 2.0	0.077	11.5 ± 1.5
0.045 - 0.050	0.048	97.7 ± 3.1	0.058	13.0 ± 1.5	0.080	11.4 ± 1.3
0.050 - 0.055	0.053	86.6 ± 2.8	0.063	12.4 ± 0.9	0.083	9.2 ± 1.0
0.055 - 0.060	0.058	78.1 ± 2.6	0.067	11.5 ± 1.0	0.087	7.60 ± 0.89
0.060 - 0.065	0.063	69.8 ± 2.6	0.071	11.9 ± 1.7	0.090	6.87 ± 0.81
0.065 - 0.070	0.068	62.2 ± 3.0	0.076	11.1 ± 2.8	0.094	5.30 ± 0.63
0.070 - 0.075		-		-	0.097	7.18 ± 0.86
0.075 - 0.080		-		-	0.101	5.15 ± 0.98
0.080 - 0.085		-		-	0.105	6.3 ± 1.9
0.085 - 0.090		-		-	0.109	5.31 ± 0.88
0.090 - 0.100	0.095	36.4 ± 1.9	0.101	6.3 ± 1.7	0.115	4.49 ± 0.48
0.100 - 0.110	0.105	30.2 ± 1.5	0.110	7.0 ± 1.0	0.123	3.72 ± 0.83
0.110 - 0.120		-	0.120	5.58 ± 0.67		-
0.120 - 0.130		-	0.130	5.51 ± 0.52		-
0.130 - 0.140		-	0.139	5.32 ± 0.41		-
0.140 - 0.150		-		-		-
0.150 - 0.160		-		-		-
0.160 - 0.180	0.170	12.52 ± 0.51		-		-
0.180 - 0.200	0.190	10.79 ± 0.45		-		-
0.200 - 0.220	0.210	7.97 ± 0.36		-		-
0.220 - 0.250	0.235	6.14 ± 0.26		-		-
0.250 - 0.300	0.275	4.09 ± 0.14	0.277	1.76 ± 0.11	0.283	0.45 ± 0.11
0.300 - 0.350	0.325	2.61 ± 0.10	0.327	1.174 ± 0.074	0.331	0.326 ± 0.064
0.350 - 0.400	0.375	1.582 ± 0.071	0.377	0.849 ± 0.055	0.381	0.229 ± 0.047
0.400 - 0.500	0.450	0.875 ± 0.038	0.451	0.472 ± 0.030	0.455	0.122 ± 0.023
0.500 - 0.600	0.550	0.370 ± 0.022	0.551	0.250 ± 0.020	0.554	0.045 ± 0.012
0.600 - 0.700	0.650	0.190 ± 0.015	0.651	0.091 ± 0.012	0.653	0.0308±0.0081
0.700 - 0.900	0.800	0.0466 ± 0.0070	0.801	0.0225 ± 0.0048	0.803	0.0065±0.0023

Table 6.3 Values of $<1/\beta>$ from the Lund version 5.3 event generator used to compute the cross section $1/\sigma_{tot}\,\beta\,d\sigma/dx$. (See table 6.2 and figure 6.6.)

z interval	$<1/\beta>$		
	$\pi^{\pm}$	$K^{\pm}$	$p, \bar{p}$
0.010 - 0.015	1.267	-	-
0.015 - 0.020	1.144	-	-
0.020 - 0.025	1.089	-	-
0.025 - 0.030	1.060	1.591	-
0.030 - 0.035	1.044	1.450	-
0.035 - 0.040	1.033	1.352	1.996
0.040 - 0.045	1.026	1.282	1.822
0.045 - 0.050	1.021	1.231	1.690
0.050 - 0.055	1.017	1.193	1.589
0.055 - 0.060	1.014	1.163	1.506
0.060 - 0.065	1.012	1.139	1.440
0.065 - 0.070	1.010	1.120	1.386
0.070 - 0.075	1.009	1.105	1.341
0.075 - 0.080	1.008	1.093	1.303
0.080 - 0.085	1.007	1.082	1.271
0.085 - 0.090	1.006	1.073	1.244
0.090 - 0.100	1.005	1.063	1.211
0.100 - 0.110	1.004	1.052	1.175
0.110 - 0.120	1.004	1.043	1.148
0.120 - 0.130	1.003	1.037	1.126
0.130 - 0.140	1.003	1.031	1.109
0.140 - 0.150	1.002	1.027	1.095
0.150 - 0.160	1.002	1.024	1.084
0.160 - 0.180	1.002	1.020	1.070
0.180 - 0.200	1.001	1.016	1.057
0.200 - 0.220	1.001	1.013	1.047
0.220 - 0.250	1.001	1.011	1.038
0.250 - 0.300	1.001	1.008	1.028
0.300 - 0.350	1.000	1.006	1.020
0.350 - 0.400	1.000	1.004	1.015
0.400 - 0.500	1.000	1.003	1.011
0.500 - 0.600	1.000	1.002	1.007
0.600 - 0.700	1.000	1.001	1.005
0.700 - 0.900	1.000	1.001	1.004

Table 6.4 The cross section z/σ_{tot} $d\sigma_i/z$ as a function of $z = p_{hadron}/p_{beam}$ for $i = \pi^{\pm}$, $K^{\pm}$ and p, $\bar{p}$. The factor of z is taken as the mean z over the interval for all particle types combined.

z interval	<z>	$\frac{z}{\sigma}\frac{d\sigma}{dz}$ $(e^+e^- \rightarrow h^{\pm} + X)$		
		$\pi^{\pm}$	$K^{\pm}$	p, $\bar{p}$
0.010 - 0.015	0.0126	1.118 ± 0.091	-	-
0.015 - 0.020	0.0175	2.426 ± 0.095	-	-
0.020 - 0.025	0.0225	3.36 ± 0.15	-	-
0.025 - 0.030	0.0275	3.96 ± 0.14	0.153 ± 0.014	-
0.030 - 0.035	0.0325	4.25 ± 0.13	0.234 ± 0.018	-
0.035 - 0.040	0.0374	4.23 ± 0.13	0.284 ± 0.022	0.136 ± 0.024
0.040 - 0.045	0.0424	4.44 ± 0.14	0.393 ± 0.051	0.147 ± 0.020
0.045 - 0.050	0.0474	4.45 ± 0.14	0.405 ± 0.046	0.189 ± 0.022
0.050 - 0.055	0.0525	4.40 ± 0.14	0.458 ± 0.034	0.191 ± 0.022
0.055 - 0.060	0.0575	4.36 ± 0.14	0.488 ± 0.042	0.192 ± 0.023
0.060 - 0.065	0.0625	4.26 ± 0.16	0.574 ± 0.084	0.207 ± 0.024
0.065 - 0.070	0.0675	4.11 ± 0.20	0.60 ± 0.15	0.186 ± 0.022
0.070 - 0.075	0.0724	-	-	0.289 ± 0.035
0.075 - 0.080	0.0775	-	-	0.235 ± 0.045
0.080 - 0.085	0.0825	-	-	0.321 ± 0.098
0.085 - 0.090	0.0875	-	-	0.300 ± 0.050
0.090 - 0.100	0.0948	3.41 ± 0.18	0.53 ± 0.14	0.290 ± 0.031
0.100 - 0.110	0.1049	3.14 ± 0.16	0.663 ± 0.097	0.283 ± 0.063
0.110 - 0.120	0.1149	-	0.589± 0.070	-
0.120 - 0.130	0.1248	-	0.6401 ± 0.061	-
0.130 - 0.140	0.1349	-	0.674 ± 0.052	-
0.140 - 0.150	0.1448	-	-	-
0.150 - 0.160	0.1550	-	-	-
0.160 - 0.180	0.1699	2.120 ± 0.086	-	-
0.180 - 0.200	0.1896	2.042 ± 0.084	-	-
0.200 - 0.220	0.2095	1.666 ± 0.076	-	-
0.220 - 0.250	0.2346	1.438± 0.060	-	-
0.250 - 0.300	0.2728	1.115 ± 0.039	0.473 ± 0.029	0.116 ± 0.027
0.300 - 0.350	0.3236	0.843 ± 0.032	0.376 ± 0.024	0.101 ± 0.020
0.350 - 0.400	0.3722	0.588 ± 0.026	0.313 ± 0.020	0.083 ± 0.017
0.400 - 0.500	0.4438	0.388 ± 0.017	0.208 ± 0.013	0.0531 ± 0.0098
0.500 - 0.600	0.5420	0.200± 0.012	0.135 ± 0.011	0.0240 ± 0.0064
0.600 - 0.700	0.6408	0.1214 ± 0.0097	0.0579 ± 0.0075	0.0195 ± 0.0051
0.700 - 0.900	0.7701	0.0359 ± 0.0054	0.0173 ± 0.0037	0.0050 ± 0.0017

Table 6.5 Charged hadron fractions as a function of $z = p_{hadron}/p_{beam}$.

z interval	Charged Hadron Fraction (%)		
	$\pi^\pm$	$K^\pm$	$p, \bar{p}$
0.035 - 0.040	90.95 ± 0.66	6.12 ± 0.45	2.93 ± 0.51
0.040 - 0.045	89.15 ± 0.99	7.90 ± 0.94	2.95 ± 0.38
0.045 - 0.050	88.21 ± 0.90	8.04 ± 0.84	3.75 ± 0.41
0.050 - 0.055	87.13 ± 0.74	9.08 ± 0.63	3.79 ± 0.41
0.055 - 0.060	86.52 ± 0.89	9.66 ± 0.80	3.82 ± 0.43
0.060 - 0.065	84.5 ± 1.7	11.4 ± 1.6	4.11 ± 0.47
0.065 - 0.070	84.0 ± 3.1	12.2 ± 3.1	3.81 ± 0.44
0.070 - 0.075	-	-	5.77 ± 0.66
0.075 - 0.080	-	-	5.06 ± 0.92
0.080 - 0.085	-	-	7.3 ± 2.1
0.085 - 0.090	-	-	7.0 ± 1.1
0.090 - 0.100	80.7 ± 3.5	12.4 ± 3.3	6.86 ± 0.70
0.100 - 0.110	76.9 ± 3.2	16.2 ± 2.3	6.9 ± 1.5
0.110 - 0.120	-	15.1 ± 1.7	-
0.120 - 0.130	-	17.4 ± 1.6	-
0.130 - 0.140	-	19.1 ± 1.3	-
0.140 - 0.150	-	-	-
0.150 - 0.160	-	-	-
0.160 - 0.180	73.4 ± 1.6	-	-
0.180 - 0.200	74.8 ± 1.9	-	-
0.200 - 0.220	70.3 ± 1.6	-	-
0.220 - 0.250	68.4 ± 1.6	-	-
0.250 - 0.300	65.4 ± 1.1	27.8 ± 1.6	6.8 ± 1.6
0.300 - 0.350	63.9 ± 1.3	28.4 ± 1.6	7.7 ± 1.5
0.350 - 0.400	59.8 ± 1.7	31.8 ± 1.8	8.4 ± 1.7
0.400 - 0.500	59.7 ± 1.5	32.1 ± 1.7	8.2 ± 1.5
0.500 - 0.600	55.8 ± 2.3	37.5 ± 2.5	6.7 ± 1.8
0.600 - 0.700	61.0 ± 3.2	29.1 ± 3.4	9.8 ± 2.5
0.700 - 0.900	61.7 ± 4.5	29.8 ± 5.0	8.5 ± 2.9

Table 6.6 The ratios $K^{\pm}/\pi^{\pm}$, $(p, \bar{p})/\pi^{\pm}$ and $(p, \bar{p})/(\pi^{\pm} + K^{\pm})$ as a function of $z = p_{hadron}/p_{beam}$.

z interval	$K^{\pm}/\pi^{\pm}$	$(p, \bar{p})/\pi^{\pm}$	$(p, \bar{p})/(\pi^{\pm}+K^{\pm})$
0.025 - 0.030	0.0386 ± 0.0035	-	-
0.030 - 0.035	0.0551 ± 0.0043	-	-
0.035 - 0.040	0.0673 ± 0.0053	0.0322 ± 0.0058	0.0302 ± 0.0054
0.040 - 0.045	0.089 ± 0.012	0.0331 ± 0.0044	0.0304 ± 0.0040
0.045 - 0.050	0.091 ± 0.010	0.0426 ± 0.0049	0.0390 ± 0.0044
0.050 - 0.055	0.1042 ± 0.0080	0.0434 ± 0.0050	0.0393 ± 0.0045
0.055 - 0.060	0.112 ± 0.010	0.0441 ± 0.0052	0.0397 ± 0.0046
0.060 - 0.065	0.135 ± 0.022	0.0486 ± 0.0059	0.0429 ± 0.0051
0.065 - 0.070	0.145 ± 0.042	0.0453 ± 0.0056	0.0396 ± 0.0047
0.070 - 0.075	-	0.0612 ± 0.0074	-
0.075 - 0.080	-	0.053 ± 0.010	-
0.080 - 0.085	-	0.079 ± 0.024	-
0.085 - 0.090	-	0.075 ± 0.012	-
0.090 - 0.100	0.154 ± 0.047	0.085 ± 0.011	0.0736 ± 0.0081
0.100 - 0.110	0.211 ± 0.038	0.090 ± 0.023	0.074 ± 0.018
.			
.			
.			
.			
0.250 - 0.300	0.424 ± 0.027	0.104 ± 0.025	0.073 ± 0.018
0.300 - 0.350	0.446 ± 0.030	0.120 ± 0.024	0.083 ± 0.018
0.350 - 0.400	0.532 ± 0.040	0.140 ± 0.030	0.092 ± 0.020
0.400 - 0.500	0.537 ± 0.039	0.137 ± 0.026	0.089 ± 0.018
0.500 - 0.600	0.673 ± 0.067	0.120 ± 0.033	0.072 ± 0.020
0.600 - 0.700	0.477 ± 0.075	0.161 ± 0.044	0.109 ± 0.031
0.700 - 0.900	0.48 ± 0.11	0.138 ± 0.049	0.093 ± 0.034

Chapter 7

Discussion of Results

7.1 Introduction

In this chapter the measured cross sections and fractions are compared to the results of other experiments and to various theoretical predictions. As in the previous chapter, error bars include both statistical and systematic uncertainties. All data points, including those of other experiments, are plotted in the centers of the corresponding x or z intervals. (This is done for lack of a better alternative: several instances will be pointed out where this procedure leads to apparent discrepancies between experiments.)

7.2 Comparison with Other Experiments

In figures 7.1 and 7.2 the differential cross section $1/\beta\sigma_{tot}\ d\sigma/dx$ is plotted along with results from HRS [1], Mark II [2], TASSO [4] and the previous measurement made by the TPC group [3]. The TASSO measurement was made at a center-of-mass energy of $\sqrt{s}$ = 34 GeV, and the others at $\sqrt{s}$ = 29 GeV. The TASSO group reported the cross section $s/\beta\ d\sigma/dx$, which was converted to the normalized cross section $1/\beta\sigma_{tot}\ d\sigma/dx$ using the TASSO value of the total cross section (R = 4.01) [63]. In general, the

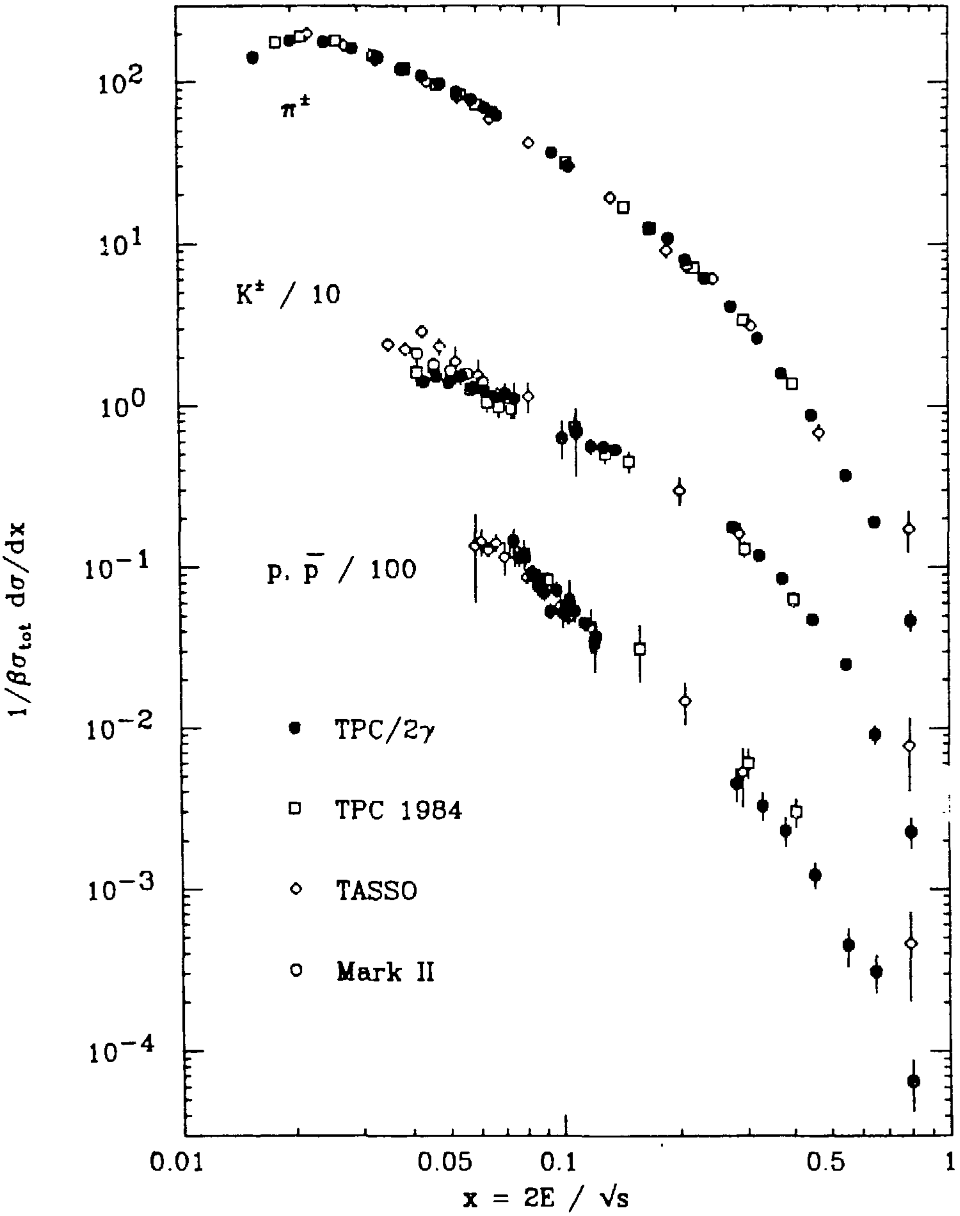

Figure 7.1 Comparison of the inclusive cross section $1/\beta\sigma_{tot}\ d\sigma/dx$ with measurements from TPC/2γ (this analysis), TPC [3], TASSO [4] and Mark II [2].

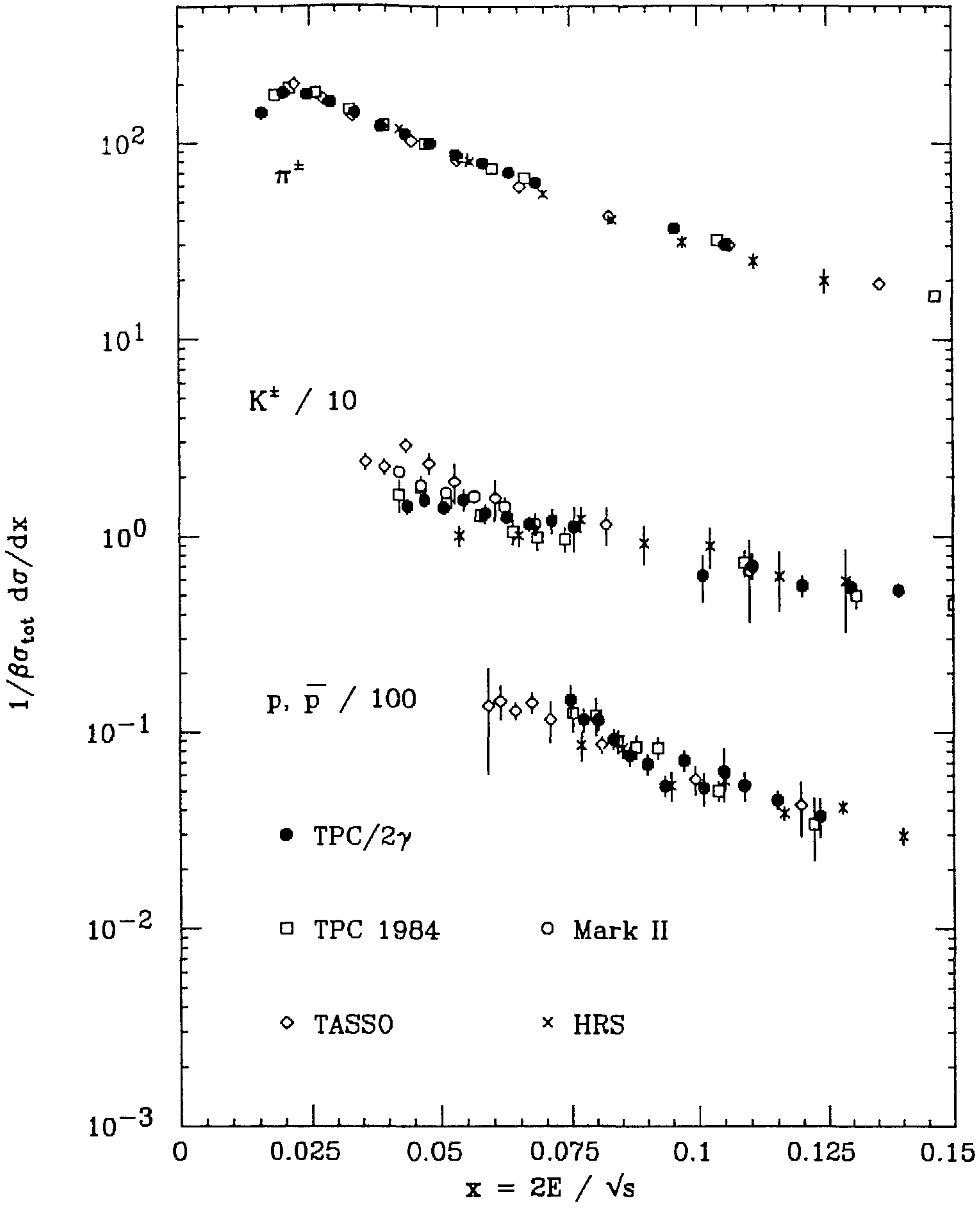

Figure 7.2 Comparison of the inclusive cross section $1/\beta\sigma_{tot}\ d\sigma/dx$ at low x with measurements from TPC/2γ (this analysis), TPC [3], TASSO [4], HRS [1] and Mark II [2].

agreement between experiments is fairly good. There is a discrepancy between the $K^{\pm}$ cross sections at low momentum, where the TASSO measurement is higher than the other three. The proton cross section from this analysis in the region $0.2 < x < 0.4$ is somewhat lower than in the previous TPC measurement. The points at the highest momentum reported by TASSO correspond to a very wide momentum interval ($10 < p < 17$ GeV, or $0.59 < x < 1.0$). Because of the rapidly falling cross section these points should actually be plotted more towards the left edge of the interval, which would move them into closer agreement with the TPC/2γ results.

In figures 7.3 and 7.4 the charged hadron fractions are compared to the previous TPC measurement [3] and to the measurements by TASSO [4] and HRS [1]. The disagreement at low momentum with TASSO stems from the previously mentioned discrepancy in the kaon cross section. The only published high-z data is from the TASSO group, with one measurement in the interval $0.59 < z < 1.0$. The TASSO measurement agrees at high-z with this analysis within quoted errors. The TPC/2γ measurement is also in agreement with an unpublished measurement by the DELCO group at PEP [64], which set a 90% c.l. upper limit of 15% on the proton fraction for $z > 0.6$.

In figure 7.5 the cross section $1/\sigma_{tot}\, d\sigma/dz$ ($e^+e^- \to h^{\pm} + X$) where $h^{\pm}$ is a charged stable hadron (i.e. $\pi^{\pm} + K^{\pm} + p, \bar{p}$) is shown along with measurements by Mark II [65] and TASSO [66]. The lowest momentum point by Mark II corresponds to a relatively broad interval ($0.0 < z < 0.05$) which could account for the discrepancy between it and the TPC/2γ and TASSO measurements. Other than this, the measurements are in reasonably good agreement.

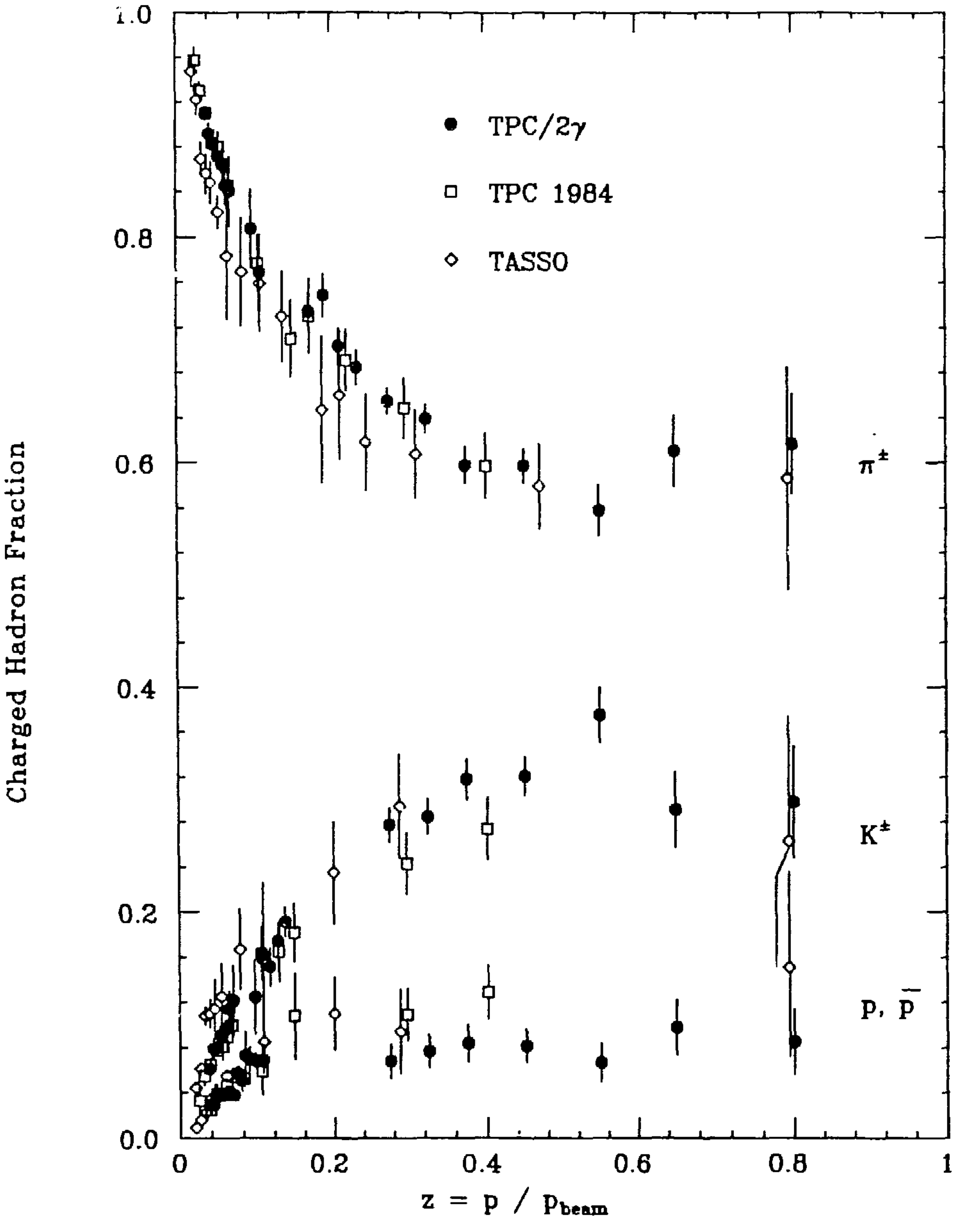

Figure 7.3 Comparison of the charged hadron fractions with measurements from TPC/2γ (this analysis), TPC [3] and TASSO [4].

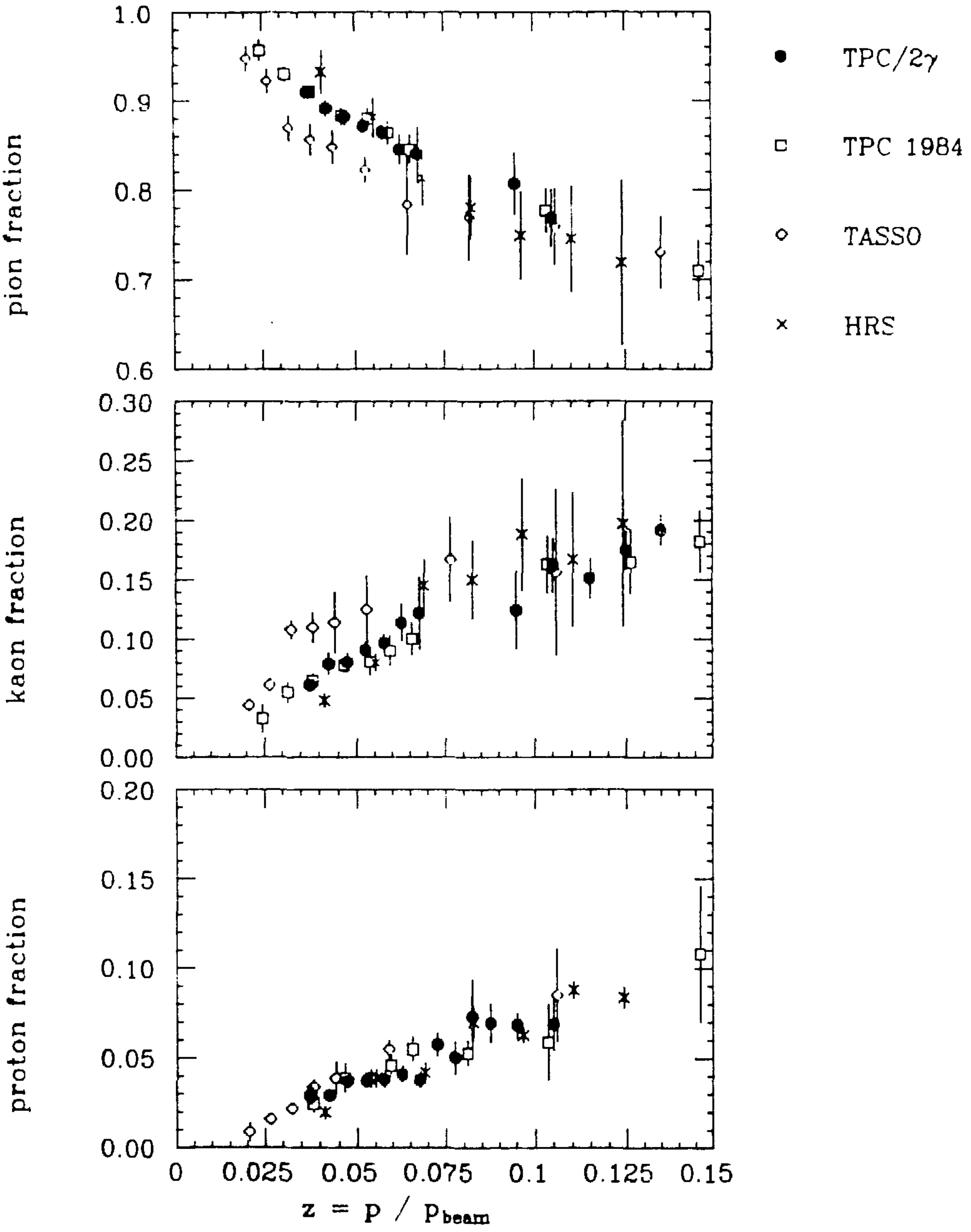

Figure 7.4 Comparison of the charged hadron fractions at low z with measurements from TPC/2γ (this analysis), TPC [3], HRS [1] and TASSO [4].

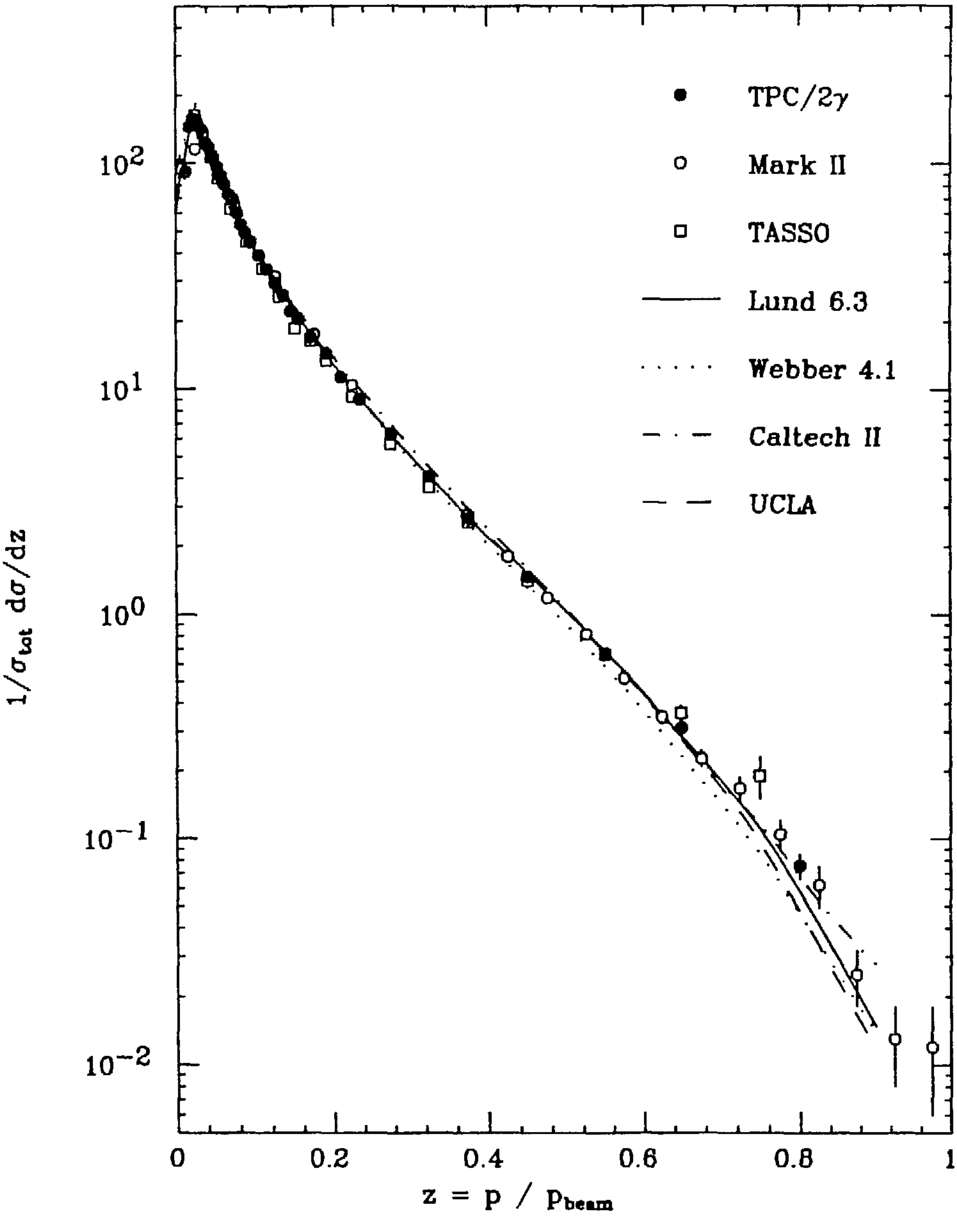

Figure 7.5 Comparison of the inclusive cross section $1/\sigma_{tot}\ d\sigma/dz$ for charged stable hadrons (i.e. $\pi^{\pm} + K^{\pm} + p, \bar{p}$) with measurements from TPC/2γ (this analysis), TASSO [4] and Mark II [2]. Also shown are the predictions of the models: Lund version 6.3 [6, 67], Webber version 4.1 [28], Caltech-II [29] and UCLA [27].

7.3 Comparison with Fragmentation Models

Qualitatively, the overall particle ratios are in agreement with the theoretical considerations discussed in chapter 2. That is, we observe more pions than kaons and more kaons than protons. The most obvious feature of the particle fractions for $z > 0.3$ is that they are approximately constant. This is in disagreement with the dimensional counting rules discussed in section 2.4.5, which predict a falling proton fraction. The statistical errors, however, are fairly large for $z > 0.6$, so a decreasing proton fraction cannot be ruled out.

Comparisons of various measured quantities with the predictions of several hadronization models (Lund [6, 55-57, 67], Webber [28], Caltech-II [29] and UCLA [27]) are shown in figures 7.5 through 7.15. Each Monte Carlo data set is based on 300,000 events, except for that of the UCLA model which is has only 100,000 events. The parameters used are given in table 7.1. The main difference between Lund 5.3 and Lund 6.3 is in the generation of the initial partonic configuration. Version 5.3 uses exact second-order QCD matrix elements, while version 6.3 uses parton showers. The Lund parameters are based on previous studies by the TPC/2γ group [53, 68, 69]. In the Webber model version 3.0, clusters always decay into two particles. In version 4.1, clusters of small enough mass "decay" into single hadrons.

In the low-z region ($z < 0.15$) there are only small differences between the predictions of the different models, and most are in excellent agreement with the data. The Webber model (both versions 3.0 and 4.1) predicts substantially fewer low-z protons than the measured number, and the UCLA model predicts slightly too few low-z protons and slightly too many low-z

Table 7.1 Parameters used in Monte Carlo hadronization models.

Lund JETSET parameters (d = default):

version:	5.3	6.3
a	0.955	0.361
b	0.6 GeV^{-2}	0.6 GeV^{-2}
Λ_{QCD}	0.642 GeV	0.372 GeV
σ_q	0.350 GeV	0.351 GeV
qq/q	0.1 (d)	0.09
s/u	0.3 (d)	0.3 (d)
$V/(V+PS)_{u,d}$	0.5 (d)	0.5 (d)
$V/(V+PS)_s$	0.6 (d)	0.5
$V/(V+PS)_{c,b}$	0.75 (d)	0.75 (d)
Q_0	-	1.0 GeV

For the Lund model, the parton evolution was by second order QCD matrix elements in version 5.3, and by parton showers in version 6.3. Parameters for the Webber and Caltech-II models and any parameters not mentioned explicitly above were left at their default values. The UCLA model used $a = 0.9$, $b = 0.85$ GeV^{-2}.

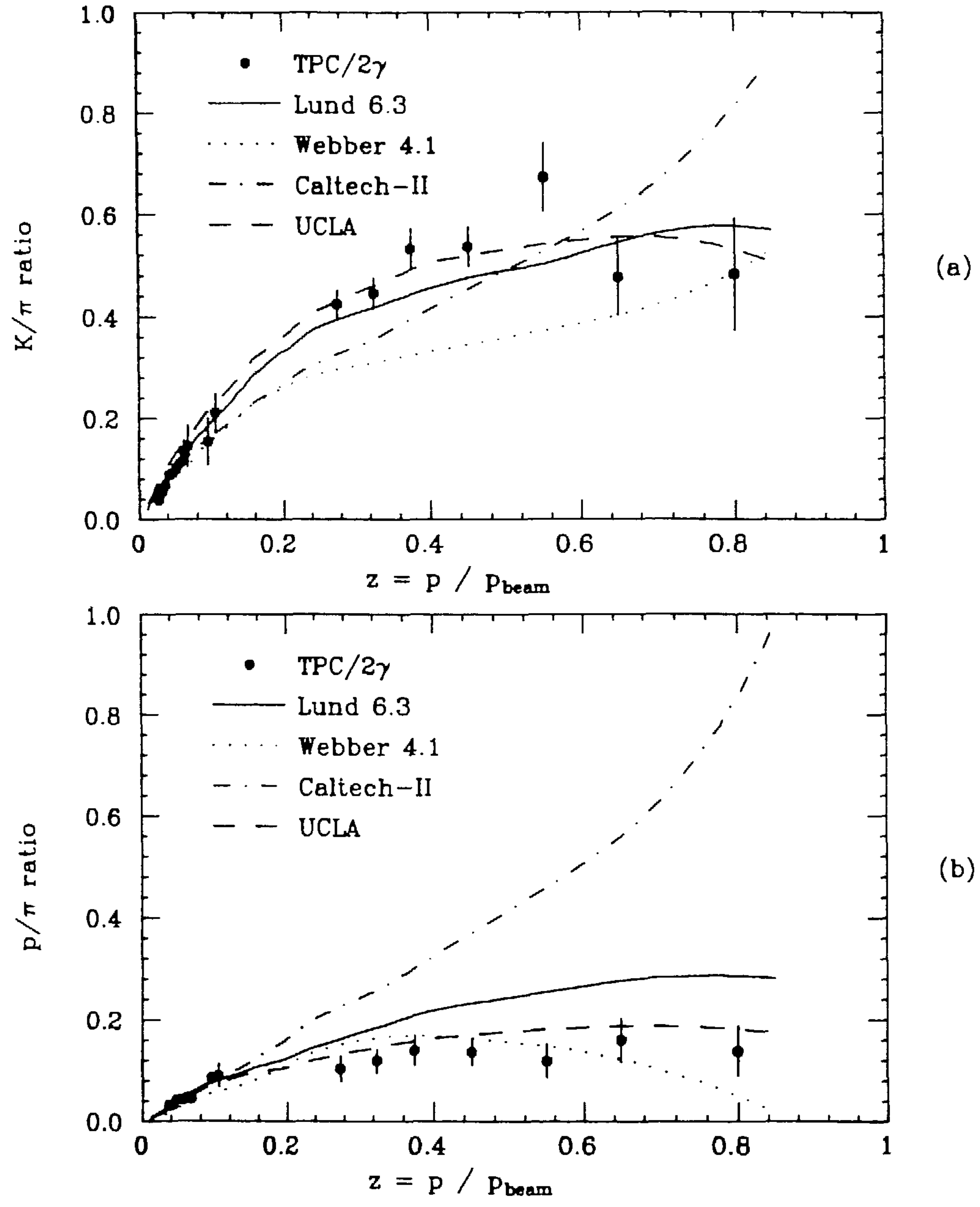

Figure 7.6 (a) Comparison of the measured K/π ratio and (b) the p/π ratio with predictions of hadronization models.

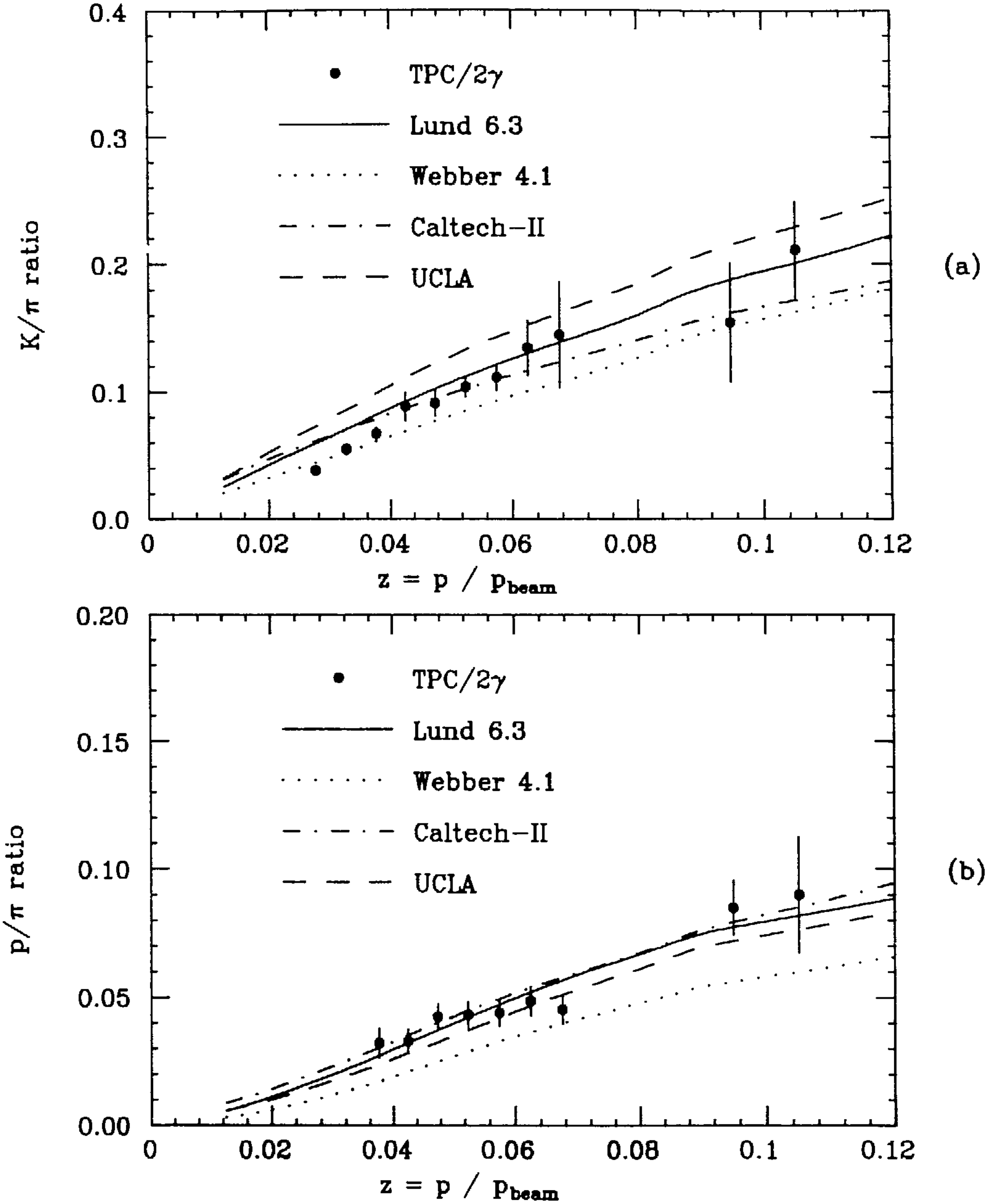

Figure 7.7 (a) Comparison of the measured K/π ratio and (b) the p/π ratio with predictions of hadronization models at low z.

kaons. All of the models have been tuned to reproduce the total charged multiplicity, which is dominated by low-z pions.

In the high-z region ($z > 0.25$) the Lund 6.3, Webber 4.1, Caltech-II and UCLA models are in reasonable agreement with the total inclusive cross section, as shown in figure 7.5. For the K/π ratio (figures 7.6 (a) and 7.7 (a)) the Webber model prediction is somewhat low in the range $0.25 < z < 0.6$, but continues to rise enough to be in agreement for $z > 0.6$. The Caltech-II K/π ratio is in mild disagreement in that it fails to level off. Both the Lund and UCLA models reproduce the K/π ratio very well. (Recall, however, that the UCLA model predicts too many low-z kaons.)

The predictions for the p/π ratio differ substantially in the high-z region, as can be seen in figures 7.6 (b) and 7.7 (b). The UCLA model is in the best agreement and the Webber model also does quite well, although both predict too few low-z protons. The high-z proton rate is somewhat too large in the Lund model, and significantly too large in the Caltech-II model. The problem with Caltech-II could possibly be cured by using an alternate decay scheme for high-z clusters, in which, for example, clusters containing diquarks are not allowed to "decay" into a single baryon [70].

In figures 7.8 through 7.15, the differential cross sections $1/\sigma_{tot}\, d\sigma_i/dz$ and the charged hadron fractions are compared with model predictions. None of the models agree very well with the data over the entire momentum range. Lund 6.3 predicts too many high-z protons, as mentioned in connection with the p/π plot. Webber 3.0 does not predict enough particles of any type at high-z, since clusters always decay into two particles. This is remedied somewhat in version 4.1, although neither version predicts particle ratios which agree over the entire momentum range. The UCLA model agrees with the data better than any other model at high-z, but disagrees at low-z in the kaon and proton rates. Nevertheless, it does surprisingly well considering the small number of adjustable parameters. The high-z particle fractions in the Caltech-II model are in significant disagreement with the data.

The Lund model was investigated further by adjusting the parameters a and b in the fragmentation function, $f(\zeta)$ (equation 2.22). For this, a and b were changed in a way that the total multiplicity remained constant. The best from tuning to low-z data are $a = 0.995$, $b = 0.6$ GeV^{-2}. This predicts too many high-z protons, as seen in figure 7.13. The values $a = 2.0$, $b = 1.2$ GeV^{-2} makes things worse, as seen in figure 7.14. The high-z proton fraction is more in agreement (although still too high) with $a = 0$, $b = 0.15$ GeV^{-2} (figure 7.15) but this leads to cross sections at high-z that are too large for all particle types. The proton fraction is also affected by the diquark to quark ratio, but this is fairly well determined by the proton cross section at low momentum.

Given the large number of parameters involved (up to a dozen) the results of this analysis cannot exclude the Lund model in its present form. The comparison, however, is not favorable, and it appears that one must do more than simply adjust a and b. One possible solution would be to revert to the fragmentation function, $f(\zeta)$, given by equation 2.21, with separate values of a for mesons and baryons. Such an $f(\zeta)$ could also be used in a UCLA-type model.

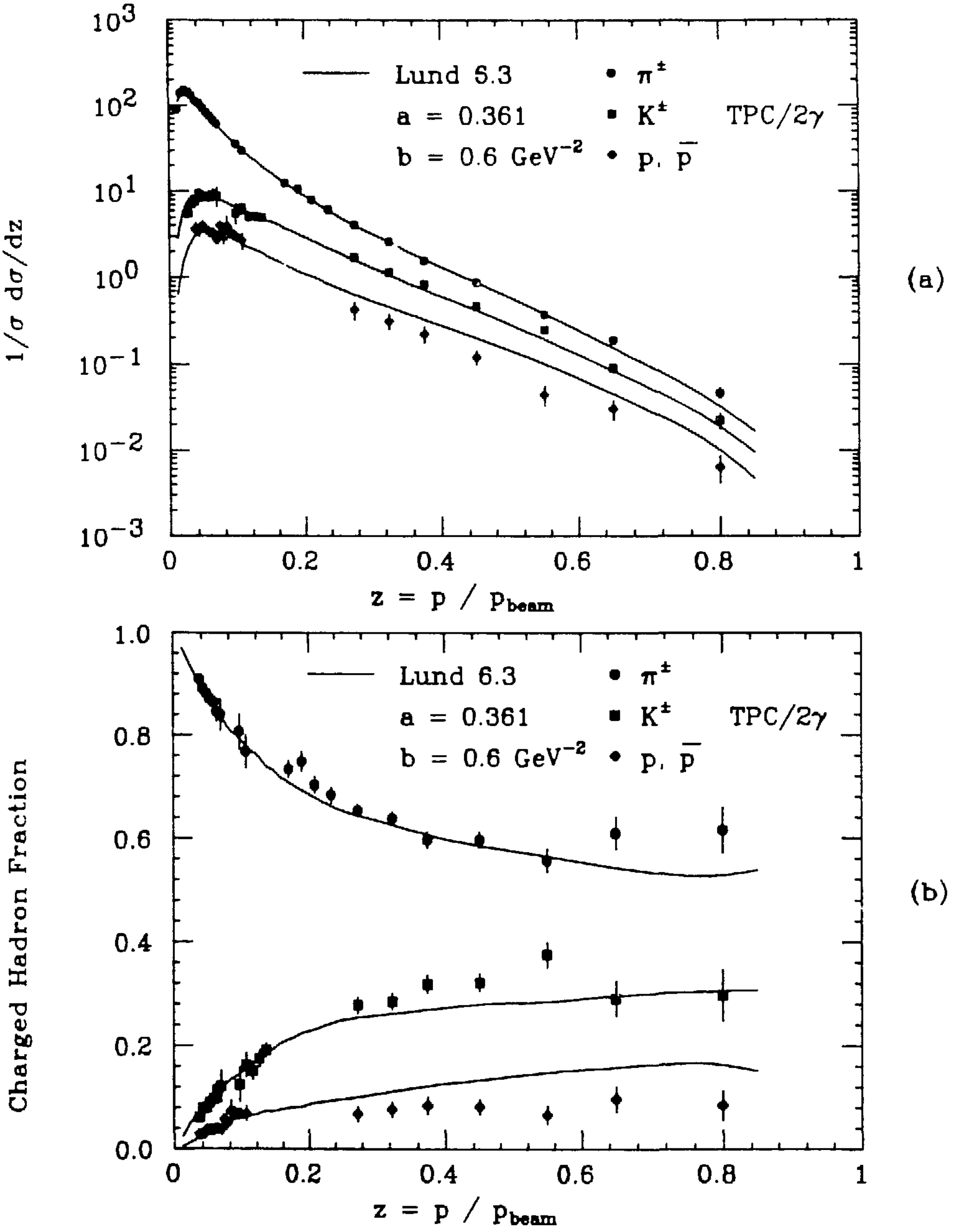

Figure 7.8 Comparison of the inclusive cross sections $1/\sigma_{tot}\, d\sigma/dz$ (a) and charged hadron fractions (b) with predictions of the Lund model version 6.3.

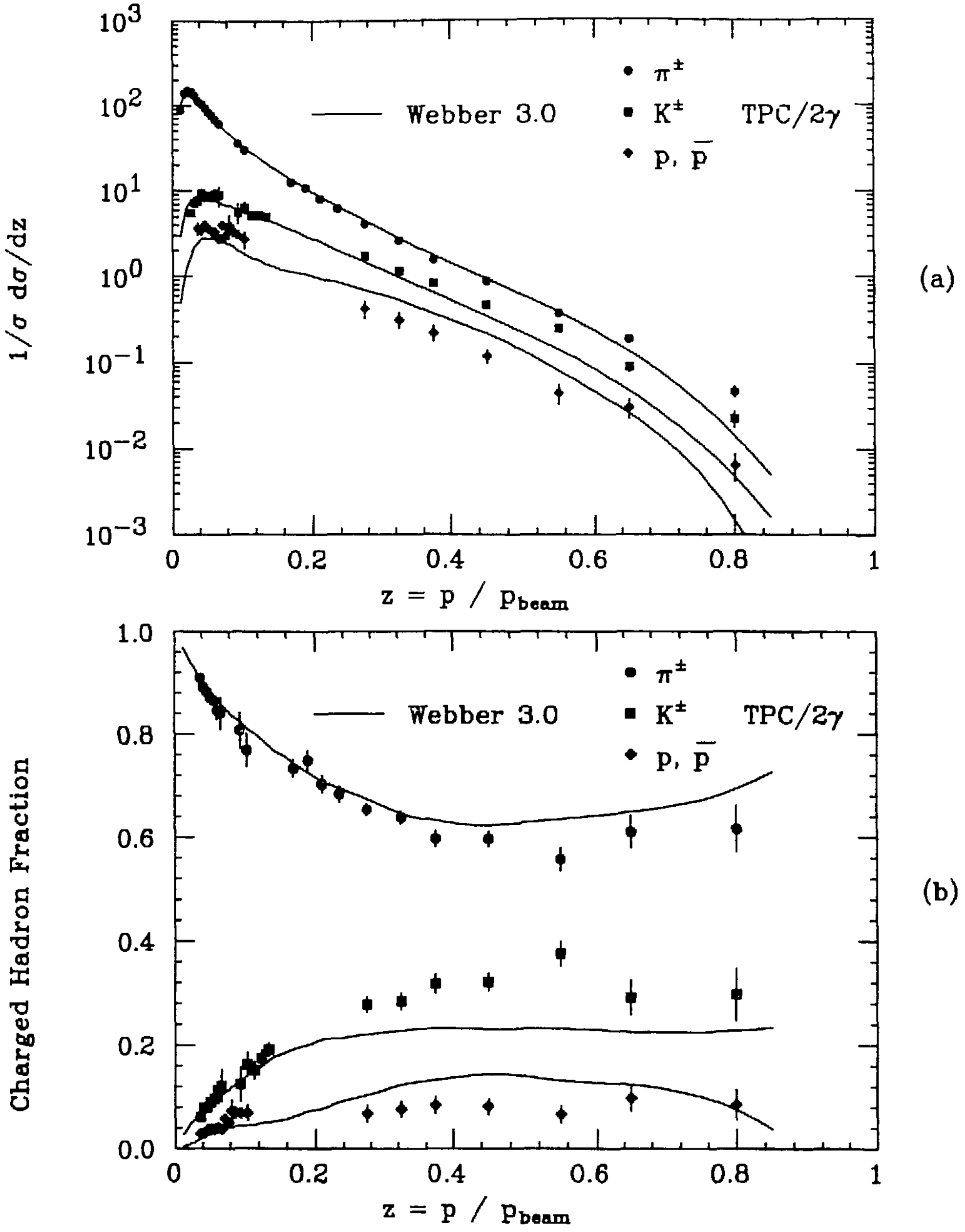

Figure 7.9 Comparison of the inclusive cross sections $1/\sigma_{tot}\ d\sigma/dz$ (a) and charged hadron fractions (b) with predictions of the Webber model version 3.0.

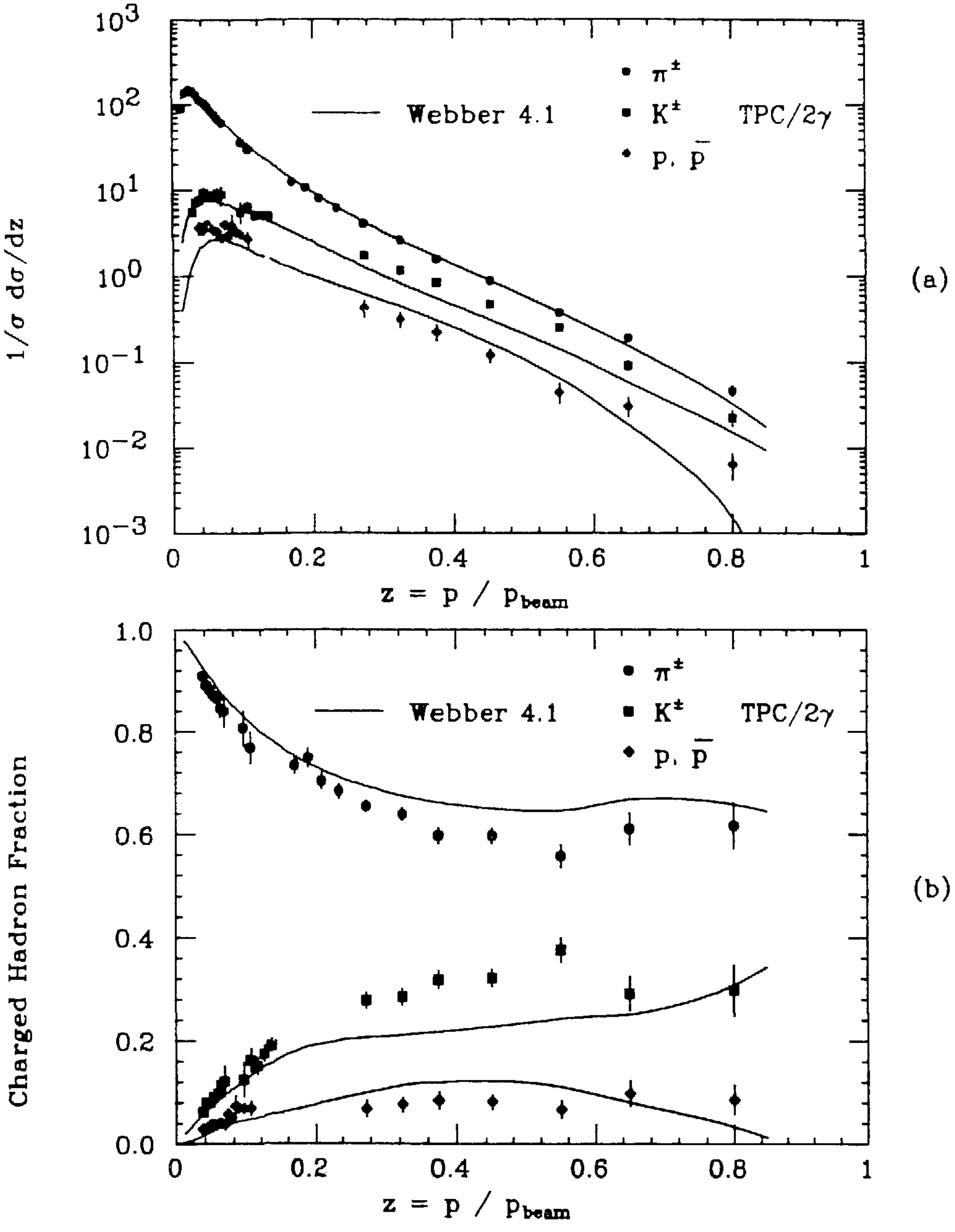

Figure 7.10 Comparison of the inclusive cross sections $1/\sigma_{tot}\ d\sigma/dz$ (a) and charged hadron fractions (b) with predictions of the Webber model version 4.1

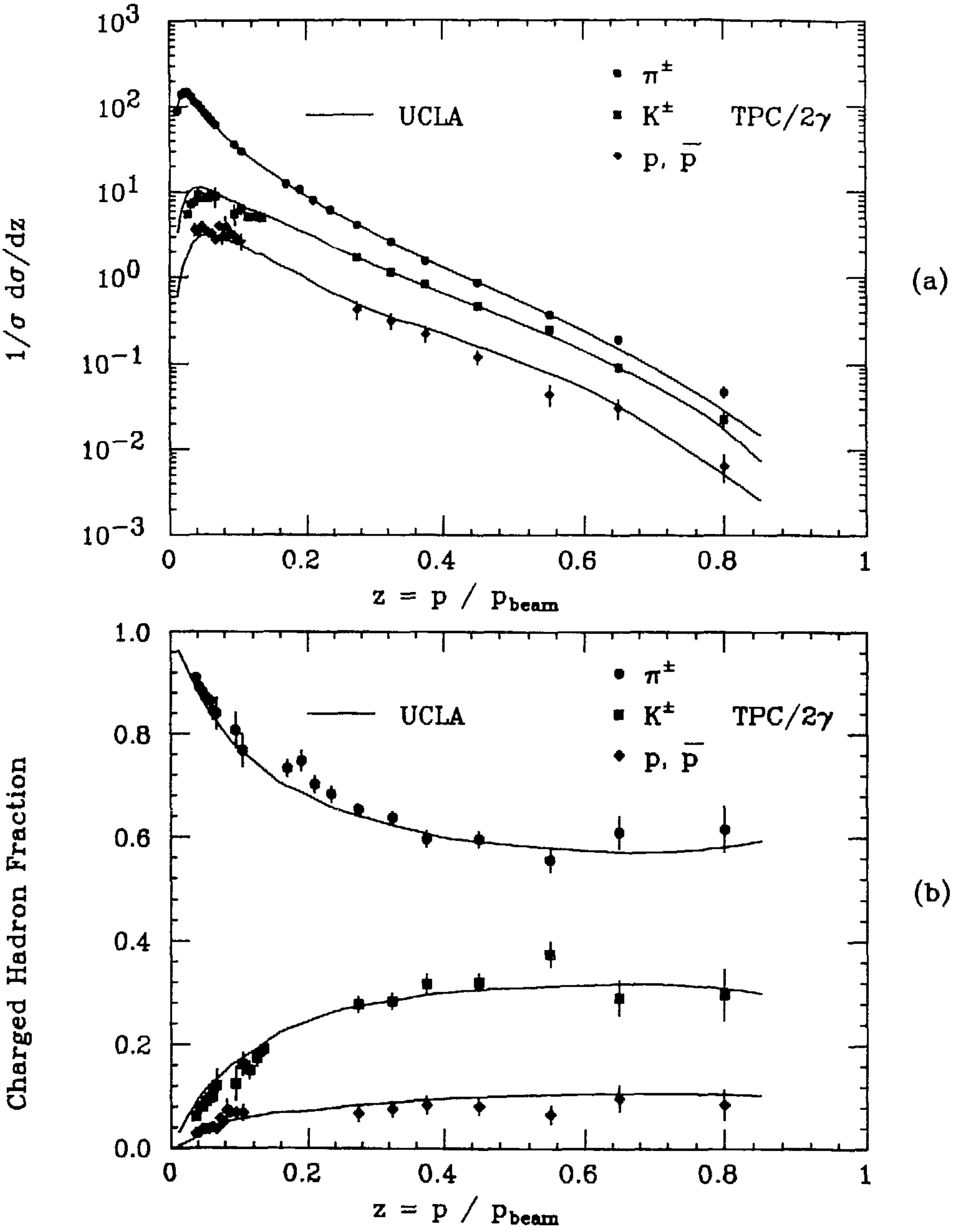

Figure 7.11 Comparison of the inclusive cross sections $1/\sigma_{tot}\ d\sigma/dz$ (a) and charged hadron fractions (b) with predictions of the UCLA model.

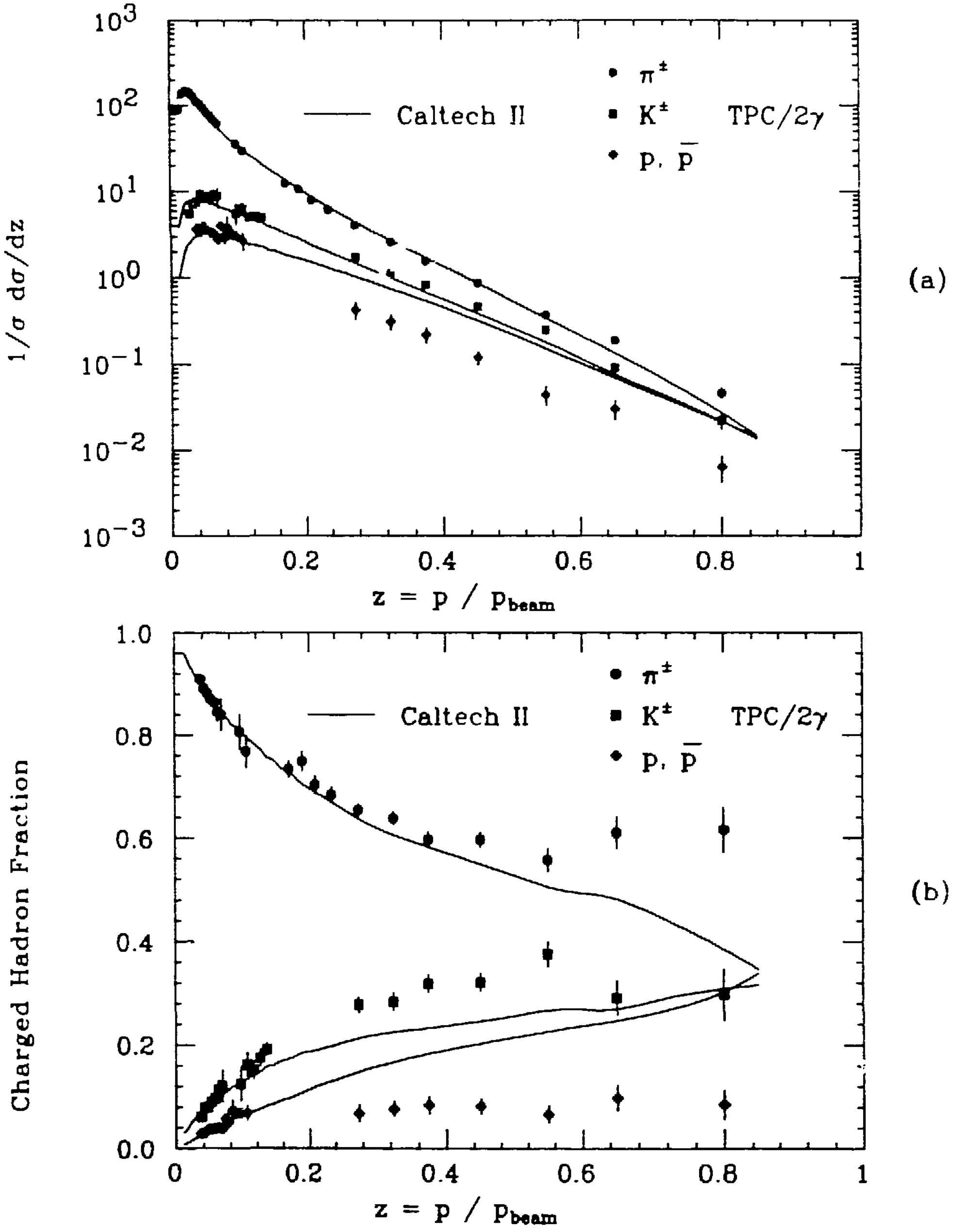

Figure 7.12 Comparison of the inclusive cross sections $1/\sigma_{tot}\ d\sigma/dz$ (a) and charged hadron fractions (b) with predictions of the Caltech-II model.

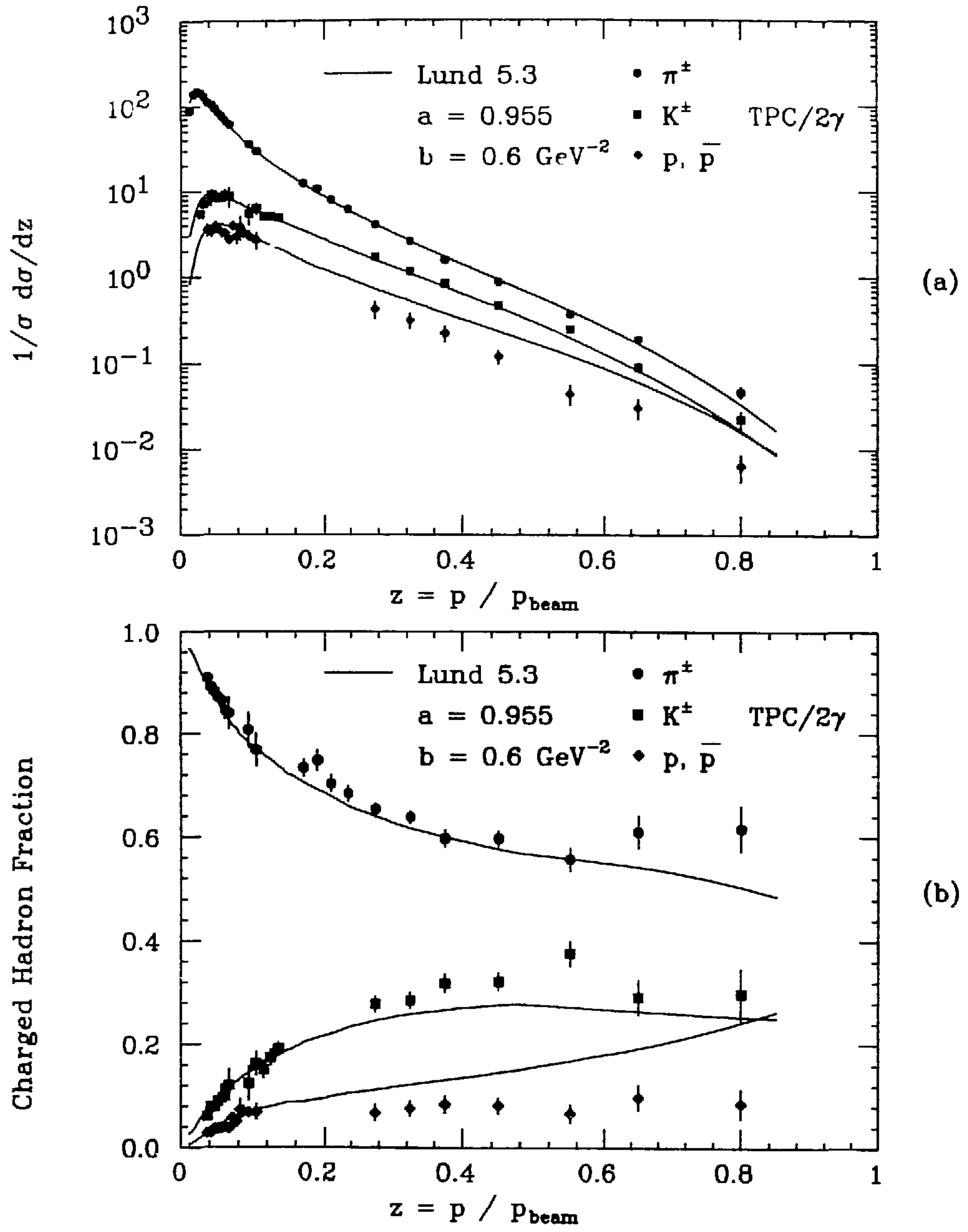

Figure 7.13 Comparison of the inclusive cross sections $1/\sigma_{tot}\ d\sigma/dz$ (a) and charged hadron fractions (b) with predictions of the Lund model version 5.3.

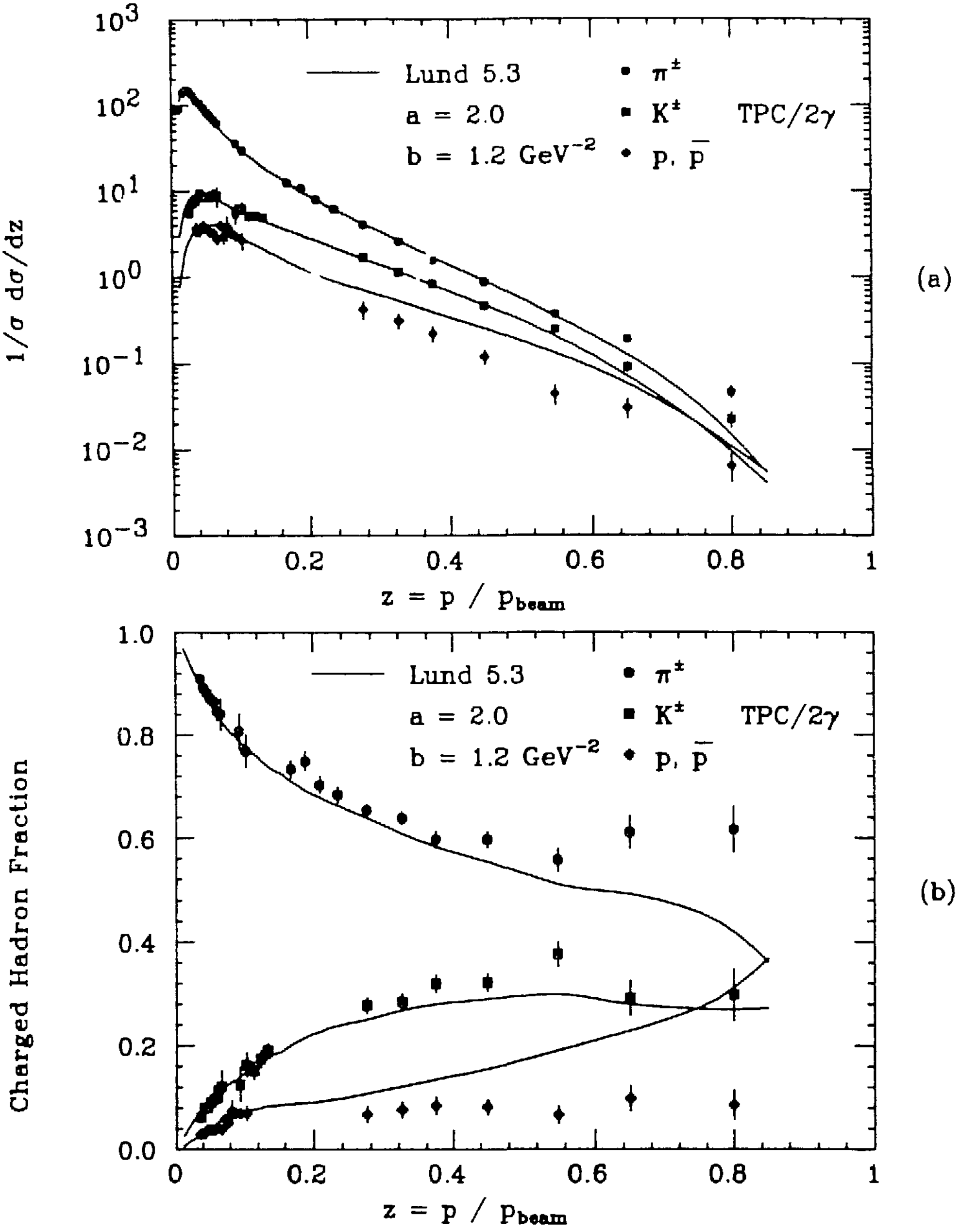

Figure 7.14 Comparison of the inclusive cross sections $1/\sigma_{tot}\, d\sigma/dz$ (a) and charged hadron fractions (b) with predictions of the Lund model version 5.3, with fragmentation function parameters a = 2.0 and b = 1.2 GeV^{-2}.

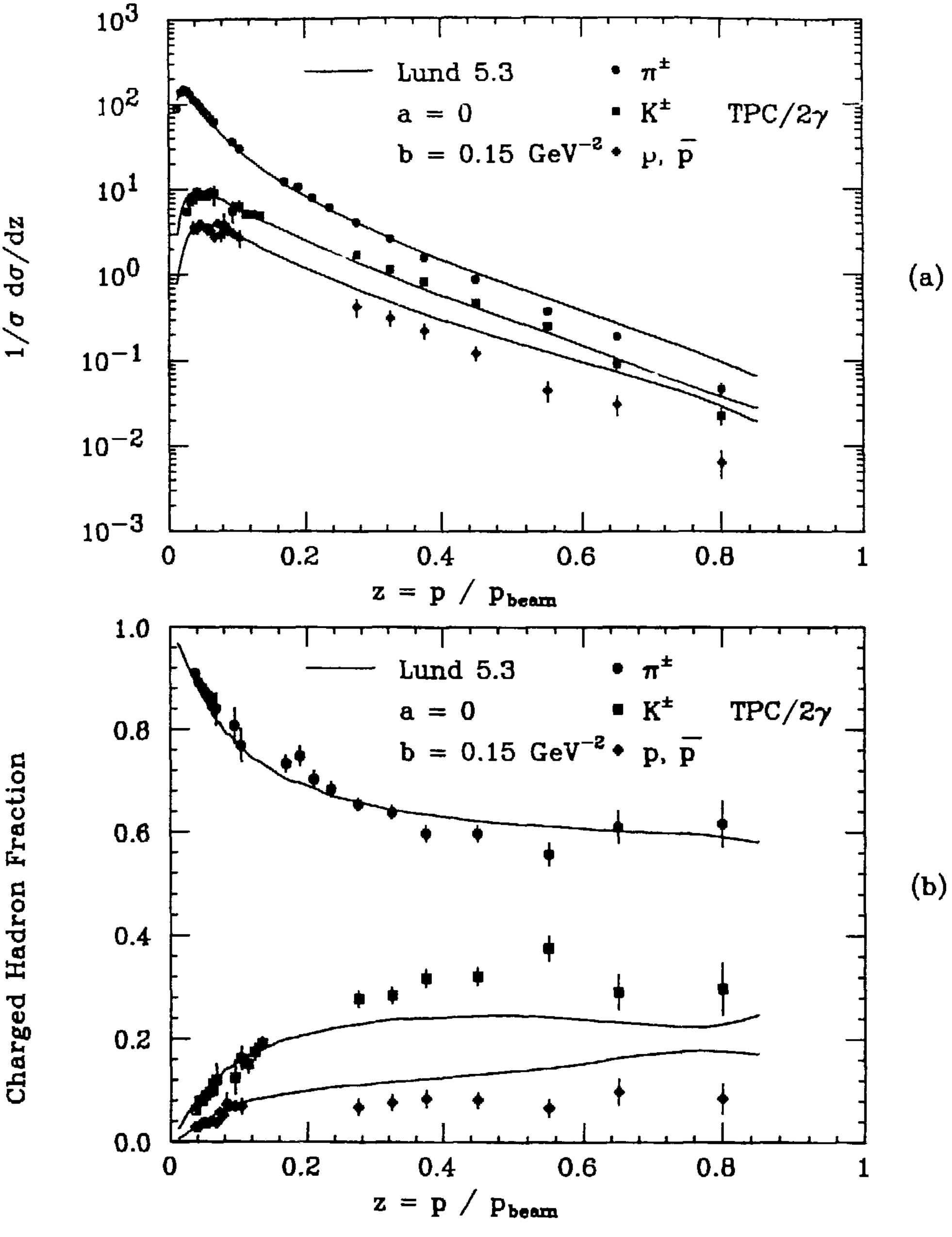

Figure 7.15 Comparison of the inclusive cross sections $1/\sigma_{tot}$ $d\sigma/dz$ (a) and charged hadron fractions (b) with predictions of the Lund model version 5.3, with fragmentation function parameters $a = 0$ and $b = 0.15$ GeV^{-2}.

Chapter 8

Summary and Conclusions

The normalized differential cross sections and charged hadron fractions have been measured for the process $e^+e^- \rightarrow h^\pm + X$ at $\sqrt{s}$ = 29 GeV, where $h^\pm$ is a charged pion, kaon or (anti)proton. The measurements were based on approximately 70 pb^{-1} of data collected between 1984 and 1986 by the TPC/2γ detector at PEP. Charged particles were identified by simultaneous measurement of momentum and (velocity sensitive) ionization rate.

The cross sections at low momentum are in fairly good agreement with previous measurements, and with the predictions of most hadronization models. This analysis provides a significant improvement in the knowledge of the particle ratios at high momentum. For $z = p/p_{beam} > 0.25$, the charged hadron fractions are observed to be approximately constant. This is in disagreement with the predictions of several hadronization models and with dimensional counting rules. None of the models studied are in better than fair agreement with the data over the entire momentum range. While some disagree worse than others, no serious attempt has been made to tune the models, and further work along these lines is needed. It is hoped that the results presented here will be useful in this regard.

References

1. M. Derrick, *et al.* (HRS) Phys. Rev. **D35**, 2639 (1987).
2. H. Schellman *et al.* (Mark II) Phys. Rev. **D31**, 3013 (1985).
3. H. Aihara *et al.* (TPC) Phys. Rev. Lett. **52**, 577 (1984).
4. M. Althoff *et al.* (TASSO) Z. Phys. **C17**, 5 (1983); An update of these results is given in *Inclusive pion, Kaon and Proton Production in e^+e^- Annihilations at 34 GeV CMS Energy*, 1985 Int. Symp. on Lepton and Photon Interactions at High Energies, Kyoto, (1985).
5. S. Brodsky and G. Farrar, Phys. Rev. Lett. **31**, 1153 (1973);
   V. A. Matveev et al., Nuovo Cimento Lett. **1**, 719 (1973);
   S. Brodsky and J. Gunion, Phys. Rev. **D17**, 848 (1978).
6. B. Andersson, G. Gustafson, G. Ingelman and T. Sjöstrand, Phys. Rep. **97**, 31 (1983).
7. R. Marshall, Rutherford Appleton Report RAL-87-031 (1987) and references therein.
8. H. Aihara *et al.* (TPC) Phys. Rev. Lett. **52**, 168 (1984).
9. H. Aihara *et al.* (TPC) Phys. Rev. Lett. **52**, 2332 (1984).
10. See, for example, F. Halzen and A. Martin, *Quarks and Leptons: An Introductory Course in Modern Particle Physics*, John Wiley & Sons, New York (1984).
11. See, for example, G. Kramer, *Theory of Jets in Electron-Positron Annihilation*, Springer-Verlag, Berlin (1984) and references therein.
12. G. Altarelli and G. Parisi, Nucl. Phys. **B126**, 298 (1977).
13. G. C. Fox and S. Wolfram, Nucl. Phys. **B168**, 285 (1980).
14. R. D. Field and R. P. Feynman, Nucl. Phys. **B136**, 1 (1978).

15. T. Meyer, Z. Phys. **C12**, 77 (1982).

16. H. Aihara *et al.* (TPC) Phys. Rev. Lett. **53**, 2199 (1984).

17. H. Aihara *et al.* (TPC/2γ), Phys. Rev. Lett. **57**, 3140 (1984).

18. R. Brandelik *et al.* (TASSO) Phys. Lett. **100B**, 357 (1981).

19. X. Artru and G. Mennessier, Nucl. Phys. **B70**, 93 (1974).

20. A. Casher, H. Neuberger and S. Nussinov, Phys. Rev. **D20**, 179 (1979).

21. J. Kogut and L. Susskind, Phys. Rev. **D11**, 395 (1975).

22. J. Schwinger, Phys. Rev. **128**, 2425 (1962).

23. E. Eichten et al., Phys. Rev. **D17**, 3090 (1978); E. Eichten et al., Phys. Rev. Lett. **34**, 369 (1975).

24. B. Andersson, G. Gustafson and B. Söderberg, Z. Phys. **C20**, 317 (1983).

25. B. Andersson, G. Gustafson and T. Sjöstrand, Nucl. Phys. **B197**, 45 (1982).

26. B. Andersson and G. Gustafson, Z. Phys. **C3**, 223 (1980).

27. C. D. Buchanan and S. B. Chun, Phys. Rev. Lett. **59**, 1997 (1987).

28. B. R. Webber, Nucl. Phys. **B238**, 492 (1984).

29. T. Gottschalk and D. Morris, Nucl. Phys. **B288**, 729 (1987).

30. H. Aihara et al., IEEE Trans. Nucl. Sci. **30**, 153 (1983).

31. *Proposal for PEP Facility Based on the Time Projection Chamber (TPC)*, Johns Hopkins University, Lawrence Berkeley Laboratory, University of California at Los Angeles, University of California at Riverside and Yale University, PEP Experiment No. 4, SLAC PUB-5012 (1976).

32. R. Fuzesy, N. Hadley and P. Robrish, Nucl. Instr. Meth. **223**, 40 (1984).

33. H. Aihara et al., IEEE Trans. Nucl. Sci. **30**, 63 (1983).

34. R. Jared, D. Landis and F. Goulding, IEEE Trans. Nucl. Sci. **29**, 57 (1982).

35. R. Jared *et al.*, IEEE Trans. Nucl. Sci. **29**, 282, (1982).

36. J. Marx, TPC Note TPC-LBL-82-84, Lawrence Berkeley Laboratory (1982).

37. P. Nemethy, P. Oddone, N. Toge and A. Ishibashi, Nucl. Instr. Meth. **212**, 273 (1983).

38. M. Ronan, TPC Note TPC-LBL-87-12, Lawrence Berkeley Laboratory (1987).

39. M. Ronan, J. Millaud and T. McGathen, IEEE Trans. Nucl. Sci. **29**, 427 (1982).

40. H. Aihara et al., IEEE Trans. Nucl. Sci. **30**, 162 (1983).

41. H. Aihara et al., IEEE Trans. Nucl. Sci. **30**, 76 (1983).

42. H. Aihara et al., IEEE Trans. Nucl. Sci. **30**, 117 (1983).

43. H. Aihara et al., IEEE Trans. Nucl. Sci. **30**, 67 (1983).

44. E. Fermi, Phys. Rev. **57**, 485 (1940).

45. A. Crispin and G. Fowler, Rev. Mod. Phys. **42**, 290 (1970).

46. L. Landau, J. Phys. U.S.S.R. **8**, 201 (1944).

47. R. Talman, Nucl. Instr. Meth. **159**, 189 (1979).

48. H. Maccabee and D. Papworth, Phys. Lett. **30A**, 241 (1969).

49. W. Allison and J. Cobb, Ann. Rev. Nucl. Part. Sci. **30**, 253 (1980).

50. The model presented here is similar to those described in: G. Lynch, TPC Note TPC-LBL-81-6, Lawrence Berkeley Laboratory, (1981); M. Shapiro (TPC, Ph.D. Thesis) Lawrence Berkeley Laboratory Report LBL-18820 (1984).

51. F. Lapique and F. Piuz, Nucl. Instr. Meth. **175**, 297 (1980).

52. S. Kaye, TPC Note TPC-LBL-87-1, Lawrence Berkeley Laboratory (1987).

53. J. W. Gary (TPC, Ph.D. Thesis) Lawrence Berkeley Laboratory Report LBL-20638 (1985).

54. M. L. Stevenson, TPC Note TPC-LBL-84-37, Lawrence Berkeley Laboratory (1987).

55. H.-U. Bengtsson, TPC Note TPC-UCLA-84-1 (1984).

56. T. Sjöstrand, Computer Phys. Comm. **27**, 243 (1982).

57. T. Sjöstrand, Computer Phys. Comm. **28**, 229 (1982).

58. See, for example, H. Kolanoski, *Two-Photon Physics at e^+e^- Storage Rings*, Springer-Verlag, Berlin (1984).

59. A. Bäcker, *VIIth International Workshop on Photon-Photon Collisions*, A. Courau and P. Kessler ed., World Scientific, 101 (1986).

60. L. Lyons, *Statistics for Nuclear and Particle Physicists*, Cambridge University Press, Cambridge, 98-102 (1986).

61. F. James and M. Roos, Computer Phys. Comm. **10**, 343 (1975).

62. H. Aihara, *et al.* (TPC) Phys. Rev. **D31**, 2719 (1985).

63. R. Brandelik *et al.* (TASSO) Phys. Lett. **113B**, 499 (1982).

64. M. Prescott Duro (DELCO, Ph.D. Thesis) Stanford U., Phys. Dept., RX-1134 (1985).

65. A. Petersen *et al.* (Mark II) Phys. Rev. **D37**, 1 (1988).

66. M. Althoff *et al.* (TASSO) Z. Phys. **C22**, 307 (1984).

67. T. Sjöstrand, University of Lund Report LU-TP-85-10 (1985).

68. H. Aihara *et al.*, Z. Phys. **C28**, 31 (1985).

69. Tadayuki Takahashi (Ph.D. Thesis) U. Tokyo, Phys. Dept. UT-HE-87/2 (1987).

70. T. Gottschalk, private communication.